

# Ion-beam induced modifications of structural and thermophysical properties of graphite materials.

Prosvetov, Alexey

(2020)

DOI (TUprints): <https://doi.org/10.25534/tuprints-00013253>

Lizenz:



CC-BY-NC-ND 4.0 International - Creative Commons, Namensnennung, nicht kommerziell, keine Bearbeitung

Publikationstyp: Dissertation

Fachbereich: 11 Fachbereich Material- und Geowissenschaften

Quelle des Originals: <https://tuprints.ulb.tu-darmstadt.de/13253>

---

---

# Ion-beam induced modifications of structural and thermophysical properties of graphite materials

---

**Ionenstrahlinduzierte Modifikationen struktureller und thermophysikalischer Eigenschaften von Graphitmaterialien**

Zur Erlangung des Grades eines Doktors der Naturwissenschaften (Dr. rer. nat.)  
genehmigte Dissertation von **M.Sc. Alexey Prosvetov** aus Chişinău (Moldawien)

Darmstadt 2020 — D 17



TECHNISCHE  
UNIVERSITÄT  
DARMSTADT

Fachbereich Material- und  
Geowissenschaften  
Ionenstrahlmodifizierte  
Materialien

---

Ion-beam induced modifications of structural and thermophysical properties of graphite materials

Ionenstrahlinduzierte Modifikationen struktureller und thermophysikalischer Eigenschaften von Graphitmaterialien

Genehmigte Dissertation von M.Sc. Alexey Prosvetov aus Chişinău (Moldawien)

1. Gutachten: Prof. Dr. Christina Trautmann

2. Gutachten: Prof. Dr. Wolfgang Ensinger

Tag der Einreichung: 16.06.2020

Tag der Prüfung: 10.08.2020

Darmstadt 2020 – D 17

Bitte zitieren Sie dieses Dokument als:

URN: urn:nbn:de:tuda-tuprints-132530

URL: <https://tuprints.ulb.tu-darmstadt.de/id/eprint/13253>

Dieses Dokument wird bereitgestellt von tuprints,

E-Publishing-Service der TU Darmstadt

<http://tuprints.ulb.tu-darmstadt.de>

[tuprints@ulb.tu-darmstadt.de](mailto:tuprints@ulb.tu-darmstadt.de)



Die Veröffentlichung steht unter folgender Creative Commons Lizenz:

Namensnennung-Nicht kommerziell-Keine Bearbeitungen 4.0 International

<https://creativecommons.org/licenses/by-nc-nd/4.0/>

---

## Erklärung zur Dissertation

*Hiermit versichere ich, die vorliegende Dissertation ohne Hilfe Dritter nur mit den angegebenen Quellen und Hilfsmitteln angefertigt zu haben. Alle Stellen, die aus Quellen entnommen wurden, sind als solche kenntlich gemacht. Diese Arbeit hat in gleicher oder ähnlicher Form noch keiner Prüfungsbehörde vorgelegen.*

Darmstadt, 15.08.2020

---

(Alexey Prosvetov)

*I herewith formally declare that I have written the submitted thesis independently. I did not use any outside support except for the quoted literature and other sources mentioned in the work. I clearly marked and separately listed all of the literature and all of the other sources which I employed when producing this academic work, either literally or in content. This thesis has not been handed in or published before in the same or similar form.*

Darmstadt, 15.08.2020

---

(Alexey Prosvetov)



---

## Abstract

With further development of high-power accelerators and nuclear reactors, there is a strong demand for structural materials that can withstand extreme operational conditions, e.g., large heat loads, mechanical and thermal stresses, high intensity and long-term ion irradiation. Carbon-based materials show excellent thermal transport properties and thus efficient heat dissipation required for such applications. Under ion beam irradiation, graphite also has the advantage of lower stopping power and lower radiation induced activation compared to metals. For these reasons, polycrystalline graphite is commonly used in extreme radiation environments, e.g. beam dumps. In the past, neutron-irradiation effects in graphite have been studied in detail, whereas data on material behavior under exposure to high-energy ion beams is scarce.

This thesis focuses on changes of structural and thermophysical properties induced by swift heavy ion irradiation in well-oriented flexible graphite (FG) and in fine-grained isotropic polycrystalline graphite (PG). To investigate radiation-induced degradation processes, graphite samples were irradiated with 4.8 and 5.9 MeV/u  $^{12}\text{C}$ ,  $^{48}\text{Ca}$ ,  $^{129}\text{Xe}$ ,  $^{197}\text{Au}$ , and  $^{238}\text{U}$  ions with fluences up to  $\sim 2 \times 10^{14}$  ions/cm<sup>2</sup> at the UNILAC accelerator of the GSI Helmholtz Centre for Heavy Ion Research, Darmstadt. Structural transformations along the ion range were monitored by Raman spectroscopy complemented by scanning electron microscopy. The corresponding modifications of thermophysical properties were characterized using laser flash analysis and frequency domain photothermal radiometry.

The response of FG and PG to high-energy ion beams is shown to be quite different, which is ascribed to the different initial microstructure and microtexture of these graphite materials. Radiation damage in flexible graphite follows the trend of the nuclear energy loss and yields a weak or no correlation with the electronic energy loss up to 30 keV/nm. The density of point defects produced via elastic collisions monotonously increases along the ion range and causes a pronounced thermal diffusivity degradation from  $\sim 550$  down to 50 mm<sup>2</sup>/s for the Au ion irradiation at a fluence of  $\sim 1 \times 10^{14}$  ions/cm<sup>2</sup>. In contrast, in polycrystalline graphite, both nuclear and electronic (above a certain threshold) energy loss contribute to material modifications. Raman spectroscopy reveals the same type of damage for low Z (Ca) and high Z (Au, U) ions at the end of the ion range (last  $\sim 15$   $\mu\text{m}$ ), where the nuclear energy loss is maximal. Within the range section dominated by the electronic energy loss, the irradiation with Au and U ions (high energy loss of 20-25 keV/nm) causes significant disordering, crystallite refinement and misalignment as well as partial amorphization. At the highest applied fluence of

---

$5 \times 10^{13}$  ions/cm<sup>2</sup>, this leads to a structure similar to glassy carbon. Exposure to Ca ions of the same fluence produces just a slight increase of the defect density. The corresponding drop of the thermal diffusivity is from 80 mm<sup>2</sup>/s (virgin) to ~5 mm<sup>2</sup>/s for Au ions and to ~70 mm<sup>2</sup>/s for Ca ions. Damage cross-sections in both graphite materials are calculated based on the evolution of the Raman parameters and thermophysical properties as a function of fluence. Raman parameters assigned to the lattice disorder and thermal diffusivity values show a strong correlation, providing the possibility to estimate heat transfer properties of graphite materials by means of Raman spectroscopy.

---

## Zusammenfassung

Mit der Weiterentwicklung von Hochleistungsbeschleunigern und Kernreaktoren besteht eine starke Nachfrage nach Strukturmaterialien, die extremen Betriebsbedingungen standhalten, wie z.B. große Wärmebelastungen, mechanische und thermische Beanspruchungen, sowie hochintensive und anhaltende Ionenbestrahlung. Kohlenstoffbasierte Materialien weisen hervorragende Wärmetransporteigenschaften auf, die für Anwendungen, die effiziente Wärmeableitung benötigen, äußerst wichtig sind. Im Vergleich zu Metallen hat Graphit bei Bestrahlung den Vorteil, dass der Energieverlust der Ionen klein und die strahlungsinduzierte Aktivierung gering ist. Aus diesen Gründen wird polykristalliner Graphit üblicherweise in extremer Strahlungsumgebung verwendet, z.B. für Beam Dumps. Während in der Vergangenheit Neutronenbestrahlungseffekte in Graphit gut untersucht wurden, sind nur sehr wenige die Daten zum Materialverhalten unter Bestrahlung mit Ionen sehr hoher Energie verfügbar.

Diese Arbeit konzentriert sich auf Änderungen struktureller und thermophysikalischer Eigenschaften, die durch die Bestrahlung mit hochenergetischen Schwerionen in orientiertem flexiblem Graphit (FG) und feinkörnigem, isotropem, polykristallinem Graphit (PG) hervorgerufen werden. Zur Untersuchung strahleninduzierter Abbauprozesse wurden Graphitproben mit 4,8 und 5,9 MeV/u  $^{12}\text{C}$ ,  $^{48}\text{Ca}$ ,  $^{129}\text{Xe}$ ,  $^{197}\text{Au}$  und  $^{238}\text{U}$  Ionen mit Fluenzen bis zu  $\sim 2 \times 10^{14}$  Ionen/cm<sup>2</sup> am UNILAC-Beschleuniger des GSI Helmholtzzentrums für Schwerionenforschung, Darmstadt, bestrahlt. Strukturelle Veränderungen entlang der Ionenbahn wurden mittels Raman-Spektroskopie ergänzt durch Rasterelektronenmikroskopie untersucht. Die entsprechenden Modifikationen der thermophysikalischen Eigenschaften wurden durch Laser-Flash-Analyse (LFA) und mittels photothermischer Radiometrie (PTR) charakterisiert.

Es zeigt sich, dass FG und PG sehr unterschiedlich auf die Ionenbestrahlung reagieren, was auf die unterschiedliche anfängliche Mikrostruktur und Mikrotextrur dieser Graphitmaterialien zurückzuführen ist. Strahlenschäden in flexiblem Graphit folgen dem Trend des nuklearen Energieverlusts und ergeben eine schwache oder keine Korrelation mit dem elektronischen Energieverlust bis zu 30 keV/nm. In flexiblem Graphit nimmt die Dichte der Punktdefekte, die durch elastische Kollisionen erzeugt werden, entlang des bestrahlten Bereiches monoton zu und verursacht für die Bestrahlung mit Au-Ionen bei einer Fluenz von  $\sim 1 \times 10^{14}$  Ionen/cm<sup>2</sup> eine Verschlechterung der Temperaturleitfähigkeit von  $\sim 550$  auf  $50$  mm<sup>2</sup>/s. Im Gegensatz dazu tragen bei polykristallinem Graphit sowohl nukleare als auch elektronische Energieverluste (oberhalb einer bestimmten Schwelle) zur Materialmodifikation bei. Raman-Spektroskopie zeigt für Ionen mit niedrigem Z (Ca) und hohem Z (Au, U) die gleiche Art von

---

Schädigung am Ende der Ionenreichweite (letzte  $\sim 15 \mu\text{m}$ ), wo der nukleare Energieverlust maximal ist. Innerhalb der vom elektronischen Energieverlust dominierten Ionenreichweite verursacht die Bestrahlung mit Au- und U-Ionen (hoher Energieverlust von 20-25 keV/nm) signifikante Schäden, Umorientierung und Verkleinerung der Kristallite, sowie teilweise Amorphisierung. Dies führt schließlich bei einer Fluenz von  $5 \times 10^{13}$  Ionen/cm<sup>2</sup> zu einer ähnlichen Struktur wie glasartiger Kohlenstoff. Die Bestrahlung mit Ca-Ionen gleicher Fluenz ergibt nur eine geringfügig erhöhte Defektdichte. Der entsprechende Abfall der Temperaturleitfähigkeit fällt von ursprünglich (unbestrahlt) 80 mm<sup>2</sup>/s auf  $\sim 70$  mm<sup>2</sup>/s für Ca-Ionen und auf  $\sim 5$  mm<sup>2</sup>/s für Au-Ionen ab. Aus dem Verlauf der Raman-Parameter und der Temperaturleitfähigkeit als Funktion der Fluenz werden Schadensquerschnitte für beide Graphitmaterialien abgeleitet. Raman-Parameter, die der Gitterstruktur zugeordnet sind, und Temperaturleitfähigkeit zeigen eine starke Korrelation. Daraus ergibt sich die Möglichkeit, die Wärmetransporteigenschaften von Graphitmaterialien mittels Raman-Spektroskopie abzuschätzen.

---

# Table of contents

<b>ERKLÄRUNG ZUR DISSERTATION .....</b>	<b>3</b>
<b>ABSTRACT .....</b>	<b>4</b>
<b>ZUSAMMENFASSUNG .....</b>	<b>6</b>
<b>TABLE OF CONTENTS .....</b>	<b>8</b>
<b>INTRODUCTION .....</b>	<b>10</b>
1 Introduction and motivation .....	10
<b>THEORETICAL BASICS .....</b>	<b>14</b>
2 Theoretical background .....	14
2.1 Carbon and graphite .....	14
2.1.1 Graphite unit cell .....	14
2.1.2 Carbon-based materials .....	16
2.2 Ion matter interaction .....	20
2.2.1 Ion track formation .....	23
2.3 Heat transport .....	26
2.3.1 Thermal conduction .....	26
2.3.2 Thermal radiation .....	27
<b>EXPERIMENTAL .....</b>	<b>29</b>
3 Specimens .....	29
4 Ion beam irradiation .....	31
5 Characterization .....	34
5.1 Scanning electron microscopy .....	34
5.2 Raman spectroscopy .....	36
5.3 Laser flash analysis .....	44
5.4 Photothermal radiometry .....	48
<b>RESULTS AND DISCUSSIONS .....</b>	<b>51</b>
6 Structural modifications caused by ion irradiation .....	51
6.1 Well-oriented graphite .....	51
6.1.1 Scanning electron microscopy .....	51
6.1.2 Raman spectroscopy .....	52
6.2 Quasi-isotropic polycrystalline graphite .....	58
6.2.1 Scanning electron microscopy .....	58
6.2.2 Raman spectroscopy .....	59
6.3 Discussion and summary .....	69

---

7	Thermophysical modifications caused by ion irradiation .....	72
7.1	Well-oriented graphite .....	72
7.1.1	In-plane laser flash analysis.....	72
7.1.2	Transversal laser flash analysis.....	75
7.2	Quasi-isotropic polycrystalline graphite .....	77
7.2.1	Laser flash analysis.....	77
7.2.2	Photothermal radiometry .....	79
7.3	Discussion and summary .....	91
8	Ion damage cross-section .....	93
9	Correlation of thermal diffusivity and Raman parameters .....	98
	<b>CONCLUSIONS .....</b>	<b>100</b>
10	Conclusions .....	100
11	Perspectives and open questions .....	101
	<b>REFERENCES.....</b>	<b>103</b>
	<b>LIST OF FIGURES .....</b>	<b>116</b>
	<b>LIST OF TABLES .....</b>	<b>122</b>
	<b>LIST OF ABBREVIATIONS .....</b>	<b>123</b>
	<b>ACKNOWLEDGMENTS.....</b>	<b>124</b>
	<b>CURRICULUM VITAE.....</b>	<b>126</b>

## 1 Introduction and motivation

---

The ongoing development of new generations of high-temperature nuclear reactors and high-power accelerators faces many technological challenges. One of the critical aspects is related to the extreme radiation and temperature operation conditions for engineering materials. In high-temperature gas cooled reactors (HTR), graphite acts both as moderator and as structural material, whereas in the field of high-power accelerators, graphite is the first choice material for collimators, beam dumps and production targets. For the latter application, one of the main limiting factors for higher luminosities is the degradation of the thermophysical properties of beam intercepting device materials exposed to high-intensity beams. For high-dose applications, it is thus essential to understand how the thermophysical properties of different graphite grades evolve with accumulation of radiation damage. This issue is of great importance for the future international accelerator Facility for Antiproton and Ion Research (FAIR), which is being built at the GSI Helmholtz Centre for Heavy Ion Research (see Figure 1.1). The new FAIR facility is designed to provide ion beam intensities up to a factor of 100-1000 higher in comparison with the existent GSI facility. Operating in both slow and fast extraction modes, such beams will lead to the deposition of an enormous power in beam-intercepting materials and will be a great challenge for their resilience.

Isotropic polycrystalline graphite (PG), a material that served traditionally in the nuclear field for many decades, is still one of the best candidates for applications in extreme radiation environments [1–3]. The low atomic number and density of graphite lead to reduced energy deposition by the ion beam in comparison with metals [4]. In addition, both the nuclear activation by interaction with high-energy primary ion beams and its decay time are low for pure carbon, qualifying graphite as most favorable in terms of radiation safety [1,5]. However, it was shown that heavy ion irradiations lead to beam-induced structural defects, phase transformations and degradation of the electrical and mechanical properties of graphite [6–10]. One has also to expect a severe influence of ion irradiation on the thermophysical properties of graphite, affecting both the thermal diffusivity ( $a$ ) and thermal conductivity ( $k$ ) with a direct consequence on the efficiency of the system to diffuse the energy deposited by the ion beam. Under extreme conditions, reduced  $a$  and  $k$  may lead to performance degradation and ultimately to failure of a device.

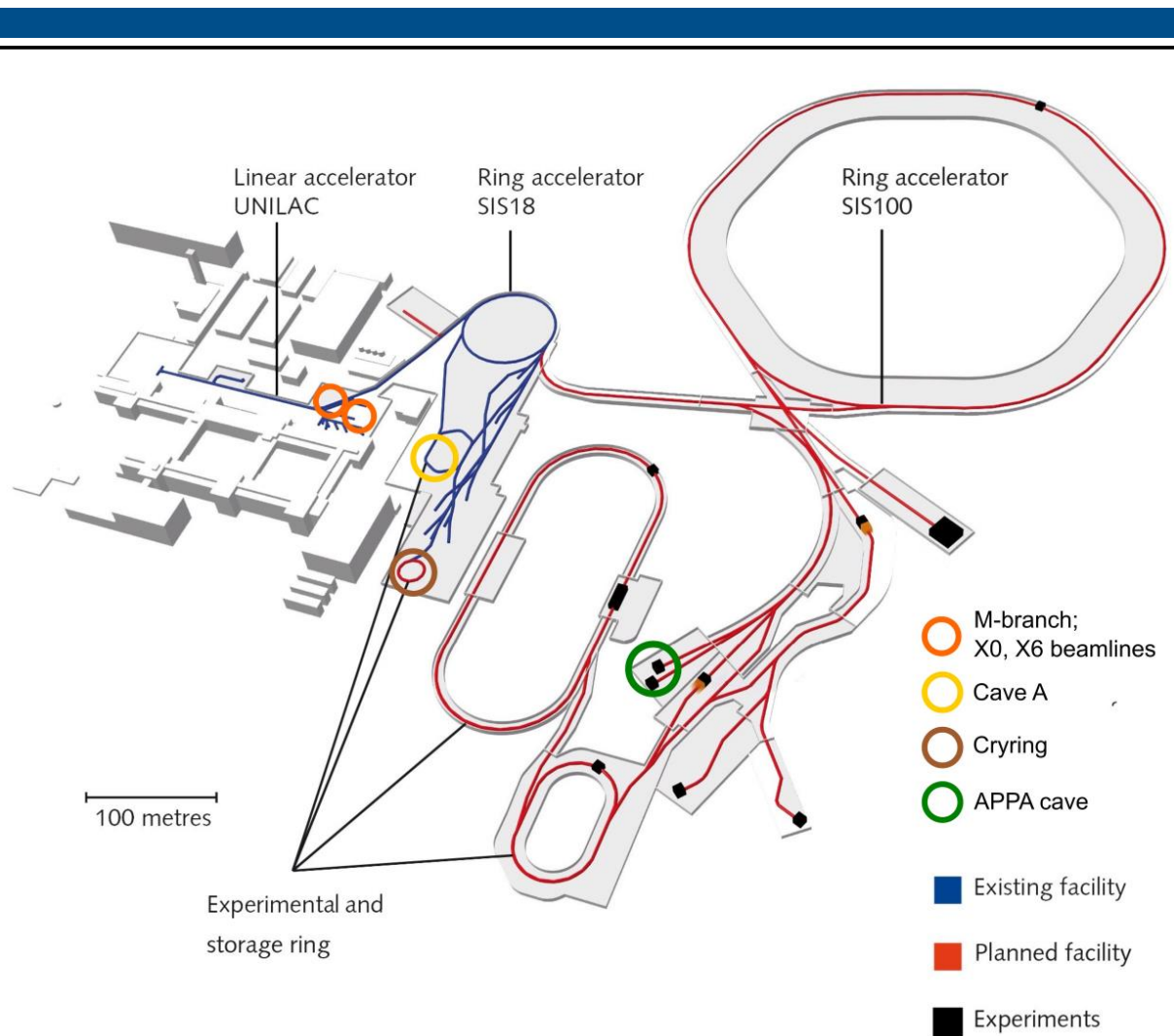


Figure 1.1 Scheme of the current GSI (in blue) and future (in red) FAIR accelerator facility, adapted from [11]. The materials research facilities are highlighted with colorful rings.

Structural and morphological irradiation-induced modifications are known to be determined by the pristine graphite structure. The evolution of thermophysical properties with accumulated radiation dose is dependent on the starting degree of graphitization. This thesis concentrates on two types of graphite, well-oriented flexible graphite (FG) and fine-grained, high density, isotropic graphite grade with improved mechanical properties and stability at elevated temperatures. Flexible graphite exhibits highly anisotropic properties with a very high thermal conductivity in the basal plane. In contrast to the more common highly oriented pyrolytic graphite (HOPG), FG has the advantage of easier handling and sample shaping, making it a good candidate for thermal management applications. Although there exist some data on ion irradiated HOPG [12–16], irradiation effects in flexible graphite has not been studied yet. Most of the previous studies on polycrystalline graphite concentrated on neutron irradiation induced damage produced by collisional displacement cascades, relevant for nuclear reactor applications [17–23]. The defect creation mechanism via elastic atomic



---

displacements, characteristic for neutron and keV-MeV ion irradiations, is quite different from ions of MeV-GeV energy [24,25]. When high-energy heavy ions pass through matter, the energy loss is dominated by ionization and electronic excitation processes of the target atoms (electronic stopping). Defect creation occurs via energy transfer from the excited electronic subsystem by electron-phonon coupling to the atomic system.

At present it is not clear to which degree nuclear and electronic stopping contribute to the overall damage and corresponding degradation of the thermophysical properties in graphite. Experimentally this phenomenon has not yet been investigated thoroughly. Data of thermal properties are scarce for neutron irradiated polycrystalline graphite and non-existing for graphite irradiated with low and high energy ions. The influence of ion irradiation on the thermophysical properties of well-oriented graphite, HOPG or FG, is unknown as well. This lack of experimental data is probably linked to the fact that the penetration depth of ions is rather limited (tens of nanometers for keV ions and up to about 100  $\mu\text{m}$  for GeV ions) and the analysis requires the preparation of sufficiently thin samples or/and more sophisticated thermophysical characterization techniques.

The aim of the thesis is to study structural modifications and corresponding changes of the thermophysical properties, induced by swift heavy ion irradiation of well-oriented flexible graphite and fine-grained isotropic polycrystalline graphite. This research extends the existing knowledge of radiation effects in different types of carbon based materials, caused by neutron and low energy ion irradiation. The results on the evolution of the graphite thermophysical properties under swift heavy ion irradiation are beneficial for the nuclear and particle accelerator community in terms of the design and the long-term operation prediction of beam intercepting devices. The obtained results for ion-beam induced thermal conductivity degradation are also important for future model calculations, because they can be used as a benchmark for computer models such as finite element and molecular dynamics simulations [26–29].

In this work, structural modifications of flexible graphite and fine-grained, isotropic graphite samples irradiated with 4.8 MeV/u C, Ca, Xe, Au and U ions were investigated using Raman spectroscopy complemented by scanning electron microscopy. The corresponding changes of thermophysical properties were characterized by in-plane laser flash analysis (LFA) [30] and photothermal radiometry (PTR) [31–34] techniques.

The thesis consists of five chapters including this introduction and motivation. In chapter **Theoretical Basics** an essential review covering carbon and graphite materials, ion-matter

---

interaction, and heat transport with main thermophysical properties is provided. The **Experimental** chapter describes the samples studied, irradiation conditions and characterization methods used. **Results and Discussions** are dedicated to the observed beam-induced structural and thermophysical changes. In **Conclusions and Outlook**, the thesis summary is formulated together with achieved goals, the perspectives of this research and remaining open questions.

## 2 Theoretical background

### 2.1 Carbon and graphite

Carbon, C, is one of the most abundant elements in the universe. Its atomic number is 6, and the electron configuration is  $2s^1 2s^2 2p^2$  with 4 valence electrons. Carbon atoms can form  $sp^1$ ,  $sp^2$  and  $sp^3$  hybridization bonds, which explains the broad variety of carbon allotropes with very different physical properties. The most common carbon allotropes are graphite with pure  $sp^2$  hybridization and diamond with pure  $sp^3$  hybridization, however there are also amorphous carbon (soot), glassy carbon, fullerene, carbon nanotubes, graphene and others.

#### 2.1.1 Graphite unit cell

A stable modification of graphite is formed by ABAB stacked layers of carbon atoms in the hexagonal order (see Figure 2.1). In the basal plane each carbon atom is connected with 3 other atoms via covalent  $sp^2$  bonds ( $\sigma$ -bond) at the distance of 1.42 Å. The layers are connected via covalent  $\pi$ -bonds with the interlayer distance of 3.35 Å. The graphite unit cell consists of 4 atoms with parameters  $a$  and  $c$  equal to 2.46 Å and 6.71 Å, respectively. The theoretical density of ideal graphite is 2.267 g/cm<sup>3</sup>.

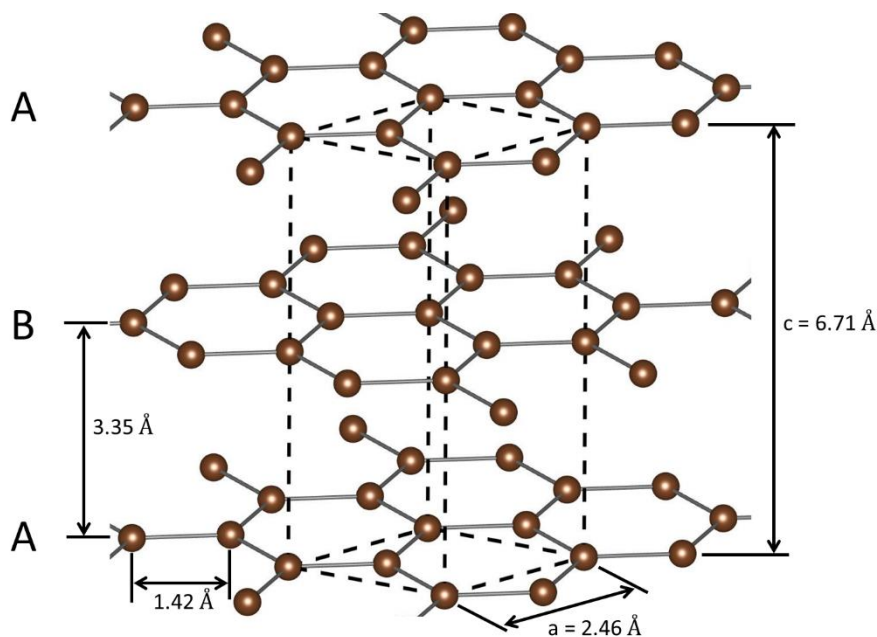


Figure 2.1 The crystal lattice of hexagonal graphite with the unit cell (dashed lines) and characteristic sizes, created using VESTA software [35].

The Brillouin zone of graphene is hexagonal and transmits into a hexagonal prism for graphite. The Brillouin zones and calculated electronic structure of graphene and graphite are shown in Figure 2.2. For a single layer graphene, the valence and conduction bands touches near the Fermi energy at the K point of the Brillouin zone, making the material a zero-gap semiconductor. With increasing number of layers and for bulk graphite the valence and conduction bands start to overlap causing semi-metal behavior [36].

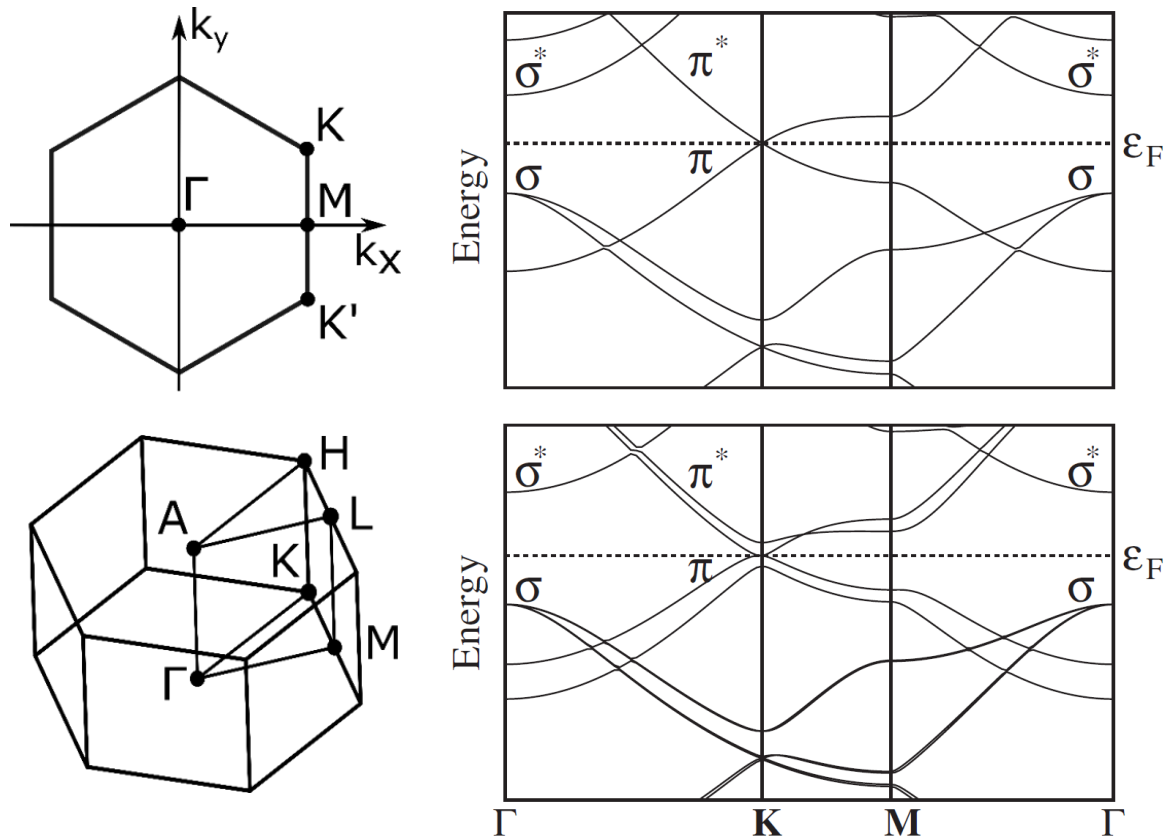


Figure 2.2 The Brillouin zone (left) and electronic band structure (right) of graphene (top) and graphite (bottom), adapted from [37].

The experimental and calculated phonon structure of graphite is presented in Figure 2.3. “O” and “A” indicate optical and acoustical phonon branches. “L”, “T” and “Z” stand for longitudinal, transversal and out of plane polarization. Primed modes refer to the oscillations of the two atoms in each layer of the unit cell, while non-primed modes indicate atoms in the same layer.

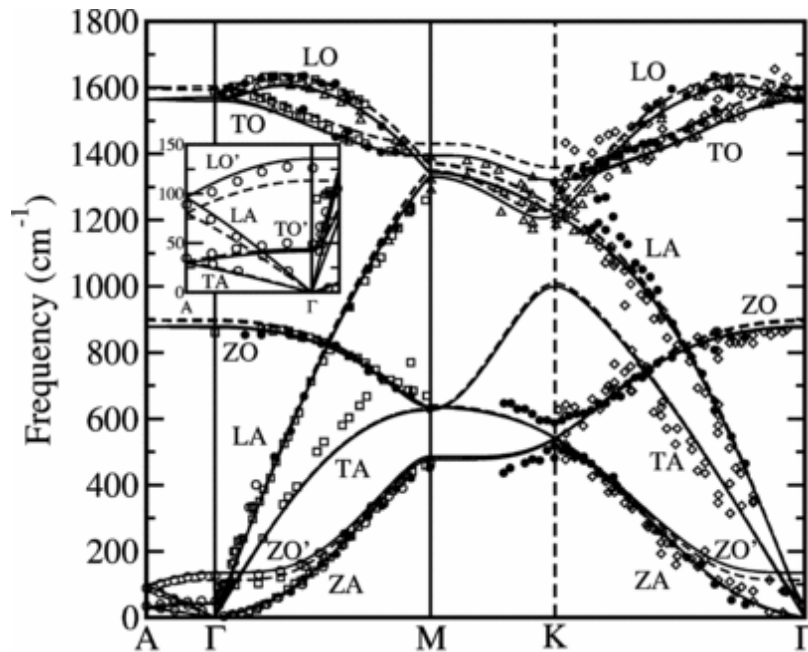


Figure 2.3 Phonon dispersion of graphite adapted from [38]. Lines and points show ab initio calculations and experimental data, respectively.

### 2.1.2 Carbon-based materials

The structure and nanotexture of carbon materials depend strongly on the precursor and the heat treatment to which the material was exposed during the production process. During carbonization the structural units in form of carbon hexagons are formed from organic precursors at temperatures around 1000-1500°C. At these temperatures, all foreign atoms are released leaving solid pure carbon as a residual. The produced anisotropic carbon units are small and can be agglomerated with different orientation. The nanotexture differs between random (glassy carbon) and oriented. The latter is classified into planar (highly oriented pyrolytic graphite (HOPG)), axial (carbon nanotubes and carbon fibers) and point (fullerene) orientation. Some carbon nanotextures can grow and develop large regular graphitic structures after further heat treatment at temperatures above 2500°C. Graphitization proceeds easily in planar oriented carbons and is strongly depressed in the case of a random oriented nanotexture such as glassy carbon even at a temperature of 3000°C. Additionally applied high pressure during heat treatment allows to accelerate the graphitization development and even to overcome the suppressed formation of random oriented glassy carbon at a temperature of 1500°C.

This work is focused on three types of carbon materials: well oriented flexible graphite (FG) as a model of an ideal graphite structure, isotropic polycrystalline graphite as an important

---

material for nuclear and other high dose applications, and glassy carbon as a reference of disordered carbon.

---

#### **2.1.2.1 Well oriented graphite**

---

Flexible graphite is produced from natural graphite, which is chemically intercalated and then exfoliated by rapid heating to 900-1200°C. The exfoliated graphite, being free of intercalates, is further molded or rolled into a sheet without any binder or adhesive. The molding or rolling process causes mechanical interconnection between exfoliated graphite particles and defines the resulting material thickness and density, typically varying from 0.1 to 3 mm and 0.7 to 1.4 g/cm<sup>3</sup>, respectively. The density also influences the mechanical and thermophysical properties of flexible graphite.

Flexible graphite is well oriented along the c axis (perpendicular to the basal plane), but it has a much larger mosaic spread angle than highly oriented pyrolytic graphite (HOPG). As a result, FG still exhibits strong anisotropic properties with a very high in-plane thermal conductivity (~150-500 Wm<sup>-1</sup>K<sup>-1</sup>) and low thermal conductivity (~5-20 Wm<sup>-1</sup>K<sup>-1</sup>) in the perpendicular direction. In addition to the typical graphite properties such as chemical and thermal stability, high thermal and electrical conductivity, flexible graphite sheets have the advantage of easy shaping, high compressibility and high resilience. Based on these properties flexible graphite is widely used for sealing and thermal management applications.

---

#### **2.1.2.2 Isotropic polycrystalline graphite**

---

The production of high density isotropic graphite can be classified based on the raw materials used and whether a binder is added or not. The most common fabrication is similar to the general production of polycrystalline graphite. The filler, petroleum and coal tar pitch cokes, as well as possibly natural and recycled graphite, are milled to a particle size of below 10-20 μm and afterwards mixed with a binder pitch. The produced carbon pastes are formed by cold isostatic pressing and then undergo carbonization with an optional pitch impregnation at a temperature around 1000°C. For graphitization, the carbon blocks are processed at a temperature of 2500-3000°C.

The binder free production of high density isotropic graphite can be performed from grinded raw coke powder with a large content of volatile substances. Another option is to use anisotropic mesophase spheres as the filler, which are called mesocarbon microbeads. They are formed at the very beginning of pyrolysis of the pitches, which are usually the residues of refining of petroleum oil and coals, and separated from the isotropic matrix using a solvent.

---

Most properties of polycrystalline graphite are dependent on the filler and binder, as well as the heat processing conditions. The polycrystalline graphite has the density of around 1.7-1.9 g/cm<sup>3</sup> with porosity of approx. 10-20%. Pore density and pore size are usually inversely proportional and have a big influence on the resulting mechanical properties. The random orientation of small anisotropic graphite grains leads to isotropic bulk properties. Thermal conductivity of polycrystalline graphite can vary between 70 and 140 Wm<sup>-1</sup>K<sup>-1</sup> and coefficient of thermal expansion stays around 4-8 ×10<sup>-6</sup> K<sup>-1</sup>. High thermal resistance, high thermal conductivity and low coefficient of thermal expansion make polycrystalline graphite highly resistant to thermal shock.

---

### 2.1.2.3 Glassy carbon

---

Glassy carbon is produced by pyrolysis of thermosetting resins or cellulose. The production process is characterized by a very slow heating rate, which should be slower than the shrinkage rate in order to compensate for the development of pores due to the gas release from the precursor.

Glassy carbon has a fullerene-related structure of randomly interconnected tortuous graphitic lamellae of sp<sup>2</sup> bonded carbon [39–42]. The curvature of graphitic flakes is ascribed to the presence of pentagons and heptagons instead of ideal hexagonal carbon rings. In general, the structure of glassy carbon strongly depends on the process temperature during pyrolysis, which can extend from 600°C to 3000°C. Low temperature grades of glassy carbon are characterized by small size, disordered sp<sup>2</sup> bonded carbon domains, which tend to rearrange and form larger and less-disordered curved flakes in a high temperature pyrolysis process. Transmission electron microscopy (TEM) images and Harris models of low and high temperature glassy carbon grades are shown in Figure 2.4.

Due to the random nanotexture, glassy carbon exhibits isotropic properties and has a low thermal conductivity, high temperature resistance, high hardness and strength. Because of large amount of small closed pores, glassy carbon has a low density (~1.4-1.5 g/cm<sup>3</sup>), very low gas and liquid permeability as well as very good corrosion resistance.



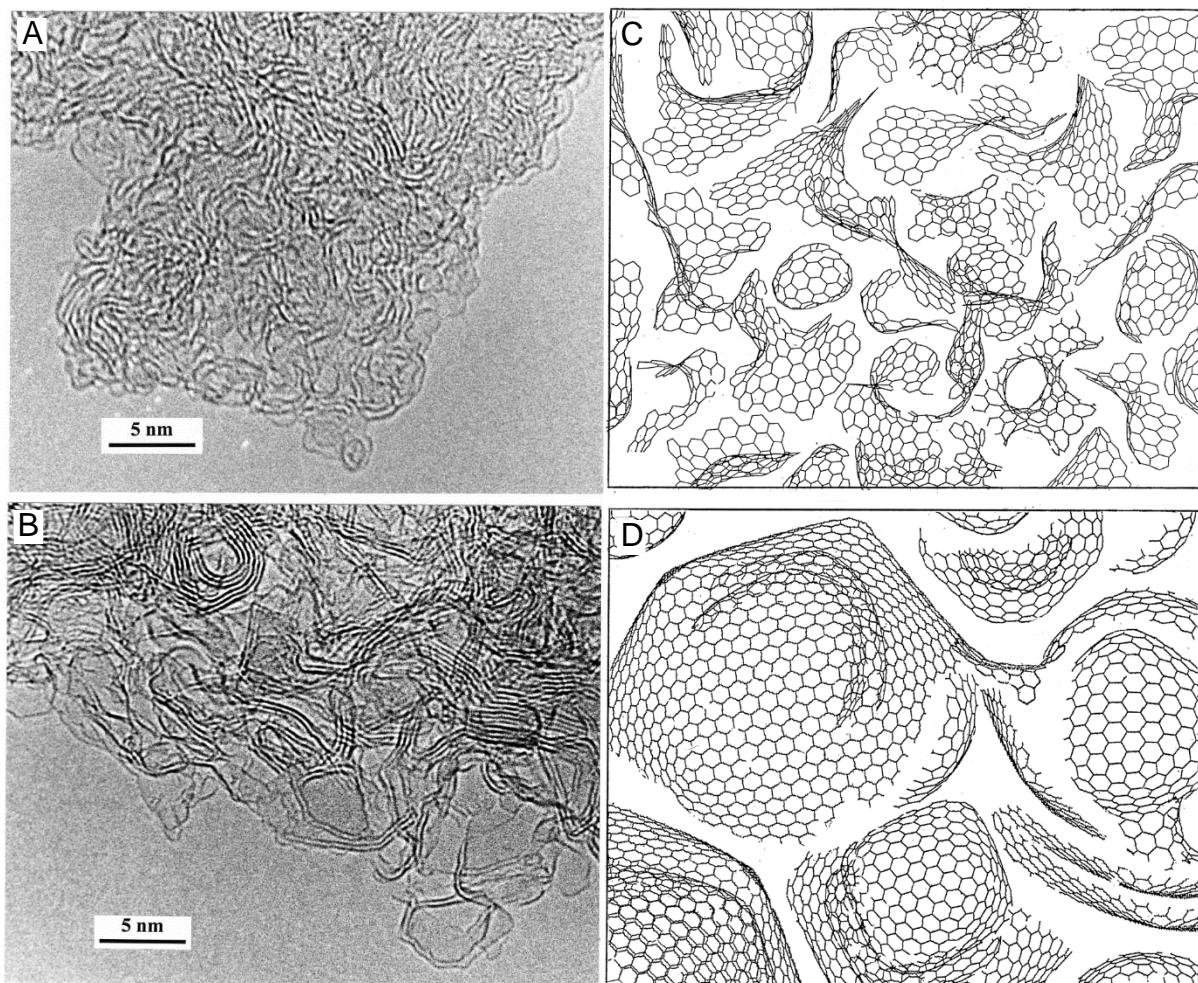


Figure 2.4 TEM images of Sigradur K (A) and Sigradur G (B) glassy carbon produced at 1000°C and 2800°C, respectively. Models for the fullerene-related structure of low-temperature (C) and high-temperature (D) glassy carbon, proposed by Harris. The figures are reproduced from [39].



---

## 2.2 Ion matter interaction

---

Swift heavy ions (SHI) are usually defined as ions heavier than  $\sim$  carbon propagating at a velocity that is higher than the electron velocity on the atomic orbitals. The typical kinetic energy of SHI lies in the range of MeV - GeV. Swift heavy ion irradiation can have a natural origin like, for examples, cosmic rays, radioactive decay and fission fragments, or can be produced artificially using ion accelerators.

When swift heavy ions propagate through matter, they slow down because of their interaction with the electron and lattice subsystems of the medium. Depending on the energy of the projectile, different processes play a major role in the stopping process.

Low energy ions mostly interact via elastic scattering on nuclei, and this process is called nuclear stopping. When the energy transferred to the recoil atom is higher than the displacement energy  $E_d$ , a point defect may be created in the lattice. The knocked-on ion leaves a vacancy in the lattice, moves and collides with other ions producing an elastic displacement cascade. The evolution of these collision cascades leads to the formation of interstitials, vacancies and vacancy clusters. Effects in the nuclear energy loss regime are comparable with radiation damage produced by neutron irradiation.

With increasing of the projectile energy, the electronic energy loss regime starts to play a major role. In this regime, the projectile scatters inelastically on the electrons of the target. The transferred energy goes to excitations and ionizations of the target atoms. The energy deposited in the electron subsystem dissipates and finally couples with the lattice, possibly producing structural and phase transformations.

When the kinetic energy of the projectile is high enough to overcome the Coulomb barrier, a nuclear reaction can occur. At relativistic velocities, the ions can generate photons via Bremsstrahlung and Cherenkov radiation.

In the MeV-GeV energy range, nuclear and electronic stopping play the main role and contributions from Bremsstrahlung and Cherenkov radiation can be neglected. Thus, the total stopping power  $S(E)$  in a solid can be expressed as:

$$S(E) = -\left(\frac{dE}{dx}\right)_{total} = -\left(\left(\frac{dE}{dx}\right)_{nuclear} + \left(\frac{dE}{dx}\right)_{electronic}\right) \quad 2.1$$

There is no analytical equation for an averaged nuclear energy loss. Usually it is calculated based on the binary collision approximation using a screened Coulomb potential.

The electronic energy loss of a charged particle in a solid depends on the projectile and target properties and is described by the Bethe equation (Eq. 2.2). The contribution of the projectile is defined by its effective charge state  $Z_{eff}$  and its energy (velocity  $v_p$ ). Due to the stripping and capturing of electrons, the effective charge is not constant and changes with the projectile velocity. Using the effective charge based on the semi-empirical Barkas formula (Eq. 2.3) [43], stopping power calculations provide good agreements with experimental data. The influence of the target material is represented in the equation by the electron number density, expressed via the atomic number  $Z_{target}$ , the molar mass  $M_{target}$  and the density  $\rho_{target}$ .

$$-\left(\frac{dE}{dx}\right)_{electronic} = \frac{e^4}{4\pi\epsilon_0^2 m_e} \times \frac{N_A \rho_{target} Z_{target}}{M_{target}} \times \frac{Z_{eff}^2}{v_p^2} \times \left( \ln \left( \frac{2m_e v_p^2}{I(1-\beta^2)} \right) - \beta^2 \right) \quad 2.2$$

$$Z_{eff} = Z_p \left[ 1 - \exp \left( -125 \frac{v_p}{c} Z_p^{-2/3} \right) \right] \quad 2.3$$

Here  $\epsilon_0$  is the vacuum permittivity,  $N_A$  is the Avogadro number,  $c$  is the speed of light,  $\beta = \frac{v_p}{c}$ ,  $e$  and  $m_e$  are the electron charge and mass respectively.  $I$  stands for the mean ionization potential of the target atoms. Although the Bethe equation shows good agreement with experimental data in the intermediate energy range, correction terms should be considered for low velocity and relativistic charged particles [44].

The radiation dose accumulated in the target is defined as damage  $D$ . It takes into account the energy loss  $\frac{dE}{dx}$ , the fluence  $\Phi$  (number of ions per unit area) and the material density  $\rho$ , and is calculated according to equation 2.4:

$$D_i = 1.6 \cdot 10^{-6} \cdot \left(\frac{dE}{dx}\right)_i \left[ \frac{keV}{nm} \right] \cdot \frac{1}{\rho [g/cm^3]} \cdot \Phi \left[ \frac{ions}{cm^2} \right] \quad 2.4$$

The Stopping and Range of Ions in Solids (SRIM), developed by Ziegler et al [45], is the most commonly used software for the calculation of the energy loss of SHI. It is based on a Monte Carlo simulation of binary collisions between nuclei with random values of the impact parameter. The main limitation of SRIM is ignoring the crystallite structure of the target (all materials are considered amorphous). Subsequently the complex dynamics of the lattice, like defect recombination and clustering, beam induced amorphization or crystallization, cannot be described using this software. The electronic energy loss values are based on fits to experimental data and it does not consider that the energy is initially deposited to the electrons and later transferred to the lattice atoms.

Nuclear and electronic energy loss values calculated with SRIM-2013 as a function of the specific energy for C, Ca, Au and U ions in graphite are shown in Figure 2.5. Specific energy

$E_s$ , defined as kinetic energy  $E$  per nucleon  $A$ , is usually used for comparison of different ions.  $E_s$  is linked to the projectile velocity and independent of the mass or the atomic number. The maximum of the electronic energy loss, called Bragg peak, in graphite corresponds to the specific energy around 1-5 MeV/u depending on the projectile atomic number. At the Bragg maximum, the electronic energy loss values are about two orders of magnitude higher than the nuclear energy loss. With decreasing energy, the ratio between electron and nuclear energy loss goes down and both stopping mechanisms contribute simultaneously below  $\sim 10$ -100 keV/u depending on the projectile mass. Before complete stopping of the projectile, the nuclear energy loss becomes dominant.

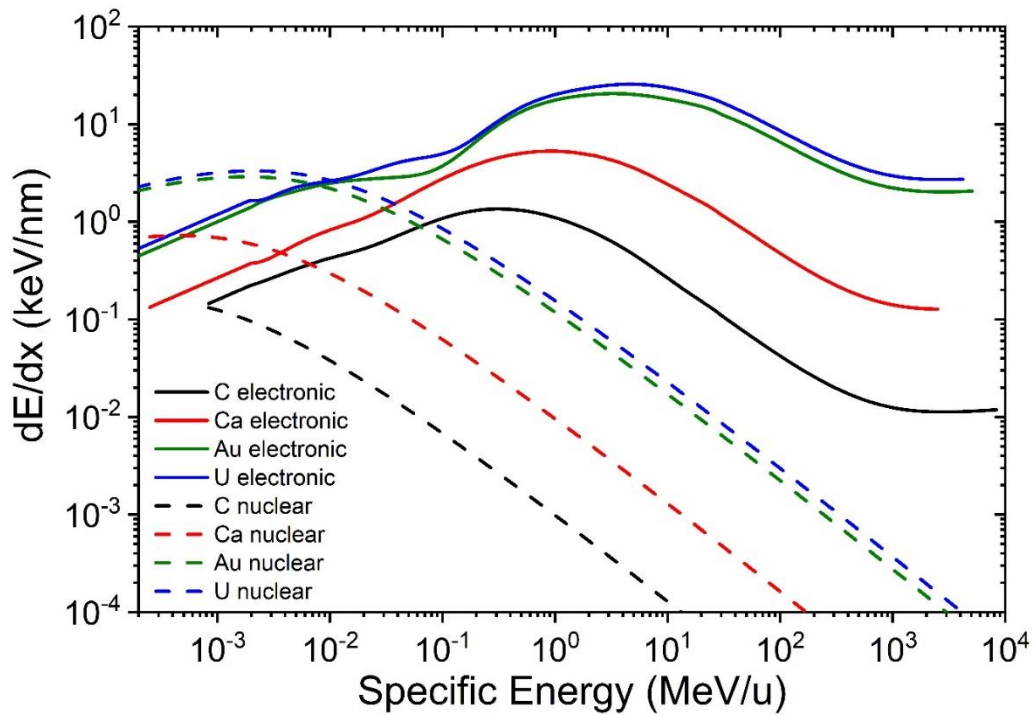


Figure 2.5 Nuclear (dashed lines) and electronic (solid lines) energy loss of different ions in graphite as a function of specific energy, calculated using SRIM-2013 software.

On the left and right sides of the Bragg peak the electronic energy loss have the same values, but because of the different velocity of the projectile, the material response is different. At the high velocity side, the excited electrons propagate radially further away from the ion trajectory and distribute the deposited energy into a larger volume in comparison with electrons excited by ions from the low velocity side. This causes a larger energy density on the slow velocity side, and as a result, stronger material modification. This phenomenon is called velocity effect [46].

---

---

### 2.2.1 Ion track formation

---

In some materials, the high energy density deposited in the electronic subsystem causes the formation of so-called ion tracks, a modified structure along the ion path with radius of several nm and length of several tens of  $\mu\text{m}$ . The first ion tracks were observed in mica exposed to U fission fragments [47]. Recent reviews of swift heavy ion irradiation effects in various materials as well as track formation models can be found in references [24,48–50]

Experimental data shows different sensitivity of materials to track formation based mainly on the electronic band structure and lattice structure. The sensitivity is usually also linked to an electronic energy loss threshold required for track formation. Most insulators, oxides and organic materials exhibit a strong sensitivity to track formation already below 10 keV/nm. Some insulators ( $\text{Al}_2\text{O}_3$ , MgO,  $\text{UO}_2$ , etc.), few metals, compounds and metallic glasses are more radiation hard and require 20-40 keV/nm for creating tracks. In high electrically conductive materials, like Cu, Ag, Au, and in diamonds characterized by high thermal conductivity no tracks were observed. Above the threshold, tracks are often cylindrical and their size increases with electronic energy loss. Electronic stopping below the threshold can cause inhomogeneous, discontinuous tracks. The track structure can also vary from material to material. In many cases, tracks are amorphous, but they can also have a complex core-shell structure or show a crystalline phase different from the initial material.

Although swift heavy ion irradiations in solids have been studied for decades, there exists no commonly accepted track formation model. The main issue is connected to the extremely short time and spatial scale of the material excitation. The projectile passes through the target typically on a time scale of  $10^{-17}$  to  $10^{-16}$  s and creates primary fast  $\delta$ -electrons. Within  $10^{-16}$  to  $10^{-14}$  s, the primary  $\delta$ -electrons spread in the material and cause the formation of secondary electrons and holes. The deposited energy couples further between the electron and lattice subsystems within  $10^{-13}$  to  $10^{-10}$  s. Subsequently, on the ns time scale the lattice responds to the excitation with structural changes, depending on the initial material structure and deposited energy density. Application of classic equations for describing such fast processes on a spatial scale of nm is limited and may cause systematic errors.

The inelastic thermal spike (i-TS) model tries to describe track formation in the electronic energy loss regime. The physical principals of the model were initially developed by Kaganov et al [51], and later adapted to track formation by Toulemonde [52,53]. The material response to the ion irradiation is calculated using a coupled system of classical thermal diffusion equations for electron and lattice subsystems (Eq. 2.5 and 2.6) with  $T_{e,a}$ ,  $C_{e,a}$ , and

$K_{e,a}$  standing for the temperature, the specific heat and the thermal conductivity of the electron and lattice subsystems, respectively. Initially the energy from the projectile is deposited in the electron subsystem described by a heat source  $A(r, t)$ . The form of  $A(r, t)$  is calculated according to the radial energy distribution of secondary electrons [54]. The energy in the form of heat dissipates within the electron subsystem and is finally transferred to the lattice. This electron-lattice energy transfer is defined by a parameter  $g$  indicating the strength of the coupling between the two subsystems. The heat transferred to the lattice can lead to a very fast temperature increase and subsequent material melting. The molten zone undergoes a fast quenching process freezing an amorphous ion track.

$$C_e(T_e) \frac{\partial T_e}{\partial t} = -\frac{1}{r} \frac{\partial}{\partial r} \left( r K_e(T_e) \frac{\partial T_e(r, t)}{\partial r} \right) - g(T_e - T_a) + A(r, t) \quad 2.5$$

$$C_a(T_a) \frac{\partial T_a}{\partial t} = -\frac{1}{r} \frac{\partial}{\partial r} \left( r K_a(T_a) \frac{\partial T_a(r, t)}{\partial r} \right) + g(T_e - T_a) \quad 2.6$$

The i-TS model shows good agreement with experimental data of amorphous tracks in many insulators and metals, however the description of semiconductors is not very consistent. The energy transfer to the lattice calculated via i-TS can be used as an input for more detailed molecular dynamics simulations of structural changes in ion tracks.

The weak points of the i-TS model, for which it is criticized [55,56], are mostly related to the application of macroscopic laws for the description of the extremely fast processes in the tracks. On the time and spatial scales mentioned, the heat transfer should have a finite propagation velocity, which is not taken into account in the heat diffusion equations. The classic equilibrium term temperature  $T$  cannot be considered for non-equilibrium thermodynamic processes in the track on a time scale up to 1 ps. The electron-phonon coupling parameter  $g$  is a free parameter, that allows fitting the model to the experimental track size data. Moreover, the i-TS model does not take into account the effect of holes in the electron subsystem.

Another model called TREKIS, which was recently developed, uses a hybrid approach of Monte Carlo simulation of the electron kinetics and molecular dynamics of the lattice [28,57]. The interaction cross-sections between electrons, holes and ions are calculated based on the formalism of the complex dielectric function (CDF) and the dynamic structure factor (DSF). DSF takes into account the collective response of the electron and ion subsystems to the excitation and can be expressed using the loss function, which equals to the inverse imaginary part of CDF. The approximation of CDF can be reconstructed from the experimental data of

---

the refractive index and the extinction coefficient of a material. This method allows taking into account coupled excitation and relaxation of the electron and lattice subsystems without macroscopic assumptions and fitting parameters, and at the same time provides results, which are in a good agreement with SRIM calculations and experimental data of track formation in various solids.

---

## 2.3 Heat transport

---

Basics of the heat transport are of great importance when studying ion beam induced damage in graphite. The heat propagation influences the material response on the ion irradiation and plays a critical role during track formation at the microscopic level. In addition, irradiation induced structural modifications can have a significant effect on the bulk thermophysical properties of a material. Thermophysical properties can be measured using various techniques based on the principles of thermal conduction and thermal radiation. One of the most convenient ways to perform a thermophysical analysis is to actively heat up a sample (for example via excitation by a pulsed or modulated laser) and measure the response using an infrared detector [58].

---

### 2.3.1 Thermal conduction

---

The parabolic heat equation 2.7, describing the heat distribution in a medium in the classical model, originates from the Fourier law of the thermal conduction with the heat flux  $\vec{q}$  (Eq. 2.8) and the energy conservation law:

$$\rho C_p \frac{\partial T}{\partial t} = k \nabla^2 T \quad 2.7$$

$$\vec{q} = -k \nabla T \quad 2.8$$

The thermal conductivity  $k$  ( $\text{Wm}^{-1}\text{K}^{-1}$ ) shows how much energy in terms of heat can be transmitted through a material. It is assigned to steady state heat transfer.

The specific heat capacity  $C_p$  ( $\text{Jkg}^{-1}\text{K}^{-1}$ ) defines a material property for storing energy in the form of heat related to the sample mass. In most heat transfer equations it appears in a product together with the density  $\rho$  ( $\text{kg m}^{-3}$ ) which is considered as volumetric heat capacity.

Another thermophysical material property is the thermal diffusivity  $a$  ( $\text{m}^2\text{s}^{-1}$ ). It is connected to the thermal conductivity and volumetric heat capacity as shown in equation 2.9 and describes how fast a given material reacts to a temperature difference and reaches equilibrium. Thermal diffusivity is usually used to describe a transient heat transfer.

$$a = \frac{k}{\rho \cdot C_p} \quad 2.9$$

The thermal effusivity  $e$  ( $\text{JK}^{-1}\text{m}^{-2}\text{s}^{-1/2}$ ) is a less common property also called the heat penetration coefficient or thermal inertia which is linked to the thermal conductivity and the

---

volumetric heat capacity (equation 2.10). It determines the heat exchange between two bodies in contact and measures the heat absorption speed.

$$e = \sqrt{k\rho C_p} \quad 2.10$$

The energy in solids can be transferred via two types of carriers, electrons and phonons, i.e. quantized lattice waves describing the elementary excitations of lattice vibrations [59]. The contribution of each carrier type depends on the electronic band structure of a material. In metals the main heat carriers are electrons, whereas the phonon mechanism is dominant for non-metals. Graphite belongs to semi-metals with phonons as main heat carriers and a small contribution of the electronic thermal conductivity [60].

According to the kinetic theory of gases, the thermal conductivity  $k$  can be expressed via the specific heat capacity  $C$ , the average particle velocity  $v$ , and the mean free path  $l$ :

$$k = \frac{1}{3} \cdot C \cdot v \cdot l \quad 2.11$$

This approach can be rather successfully applied to estimate the thermal conductivity of solids by considering phonons instead of gas molecules. The thermal conductivity strongly depends on the phonon mean free path  $l$ , or in other words, on the relaxation time between scattering  $\tau = l/v$ . Phonons can scatter through different mechanisms, including Umklapp phonon-phonon scattering, scattering on defects and impurities, phonon-electron scattering, and scattering on grain boundaries. Such processes become important when the phonon mean free path is comparable with the characteristic length scale of the material structure. The contribution of phonon-electron scattering on the thermal conductivity of solids is usually negligible. In general, the scattering mechanism strongly depends on the phonon frequency and temperature. All independent scattering processes can be taken into account by Matthiessen's rule, where  $\tau_i$  stands for the corresponding relaxation time:

$$\frac{1}{\tau} = \sum_i \frac{1}{\tau_i} \quad 2.12$$

A more detailed description of the thermal conductivity of graphite can be found in references [61–63].

---

### 2.3.2 Thermal radiation

---

All bodies of temperature above 0 K emit radiation. The spectral radiance at a given temperature  $T$  is described by Planck's law:



$$B(\lambda, T) = \frac{2\pi hc^2}{\lambda^5} \frac{1}{e^{\frac{hc}{\lambda k_B T}} - 1} \quad 2.13$$

Here  $h$  is the Planck constant,  $c$  is the speed of light,  $k_B$  is the Boltzmann constant.  $B(\lambda, T)$  defines the amount of energy, which is emitted per unit area of the body, per solid angle of emission, per spectral unit. As shown in Figure 2.6, at room temperature most of the radiation is emitted in the infrared region and shifts towards smaller wavelength with increasing temperature.

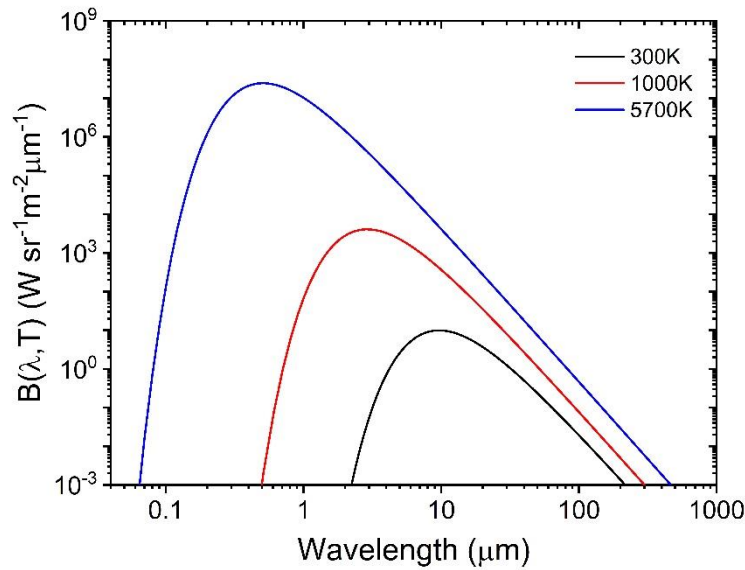


Figure 2.6 Spectral radiance according to Planck's law at different temperatures.

The total radiated power  $P$  per surface area  $A$  at the body temperature  $T$  is obtained from the integration of equation 2.13 over all wavelengths and solid angles, giving equation 2.14 called the Stefan-Boltzmann law:

$$\frac{P}{A} = \varepsilon \sigma T^4 \quad 2.14$$

where  $\sigma$  is the Stefan-Boltzmann constant and  $\varepsilon$  is the emissivity, which represents the effectiveness of emitting and absorbing energy in comparison with a black body. The emissivity is in general dependent on the wavelength, the angle of radiation and the body temperature.  $\varepsilon$  takes values from 0 (a perfect reflector) to 1 (an ideal black body).

## 3 Specimens

---

In the present work swift heavy ion irradiation effects were investigated for two different types of graphite: (1) well-oriented flexible graphite, an anisotropic graphitic structure with a low amount of defects and (2) fine-grain isotropic polycrystalline graphite.

Flexible graphite (FG) specimens were cut into 20 mm diameter discs from thin foils, produced as a laboratory test samples at SGL Carbon. The average measured thickness and density of the samples are  $21.3 \pm 0.7 \mu\text{m}$  and  $2.25 \pm 0.4 \text{ g/cm}^3$ , respectively.

The main grade of polycrystalline graphite (PG) used in this work is SIGRAFINE<sup>®</sup> R6650 by SGL Carbon with a nominal grain size of  $7 \mu\text{m}$  (according to data sheet of producer [64]). This grade is produced by isostatic pressing, and is considered as quasi-isotropic. A density of  $1.84 \text{ g/cm}^3$  and thermal conductivity of  $95 \text{ Wm}^{-1}\text{K}^{-1}$  are provided by the manufacturer.

The samples were cut into discs with a diameter of 10 and 20 mm. The 20 mm samples were lapped down to approx.  $43 \pm 7 \mu\text{m}$  thickness. The 10 mm discs have thicknesses spanning from  $\sim 50 \mu\text{m}$  to  $\sim 1 \text{ mm}$ . A photo of the different samples is shown in Figure 3.1

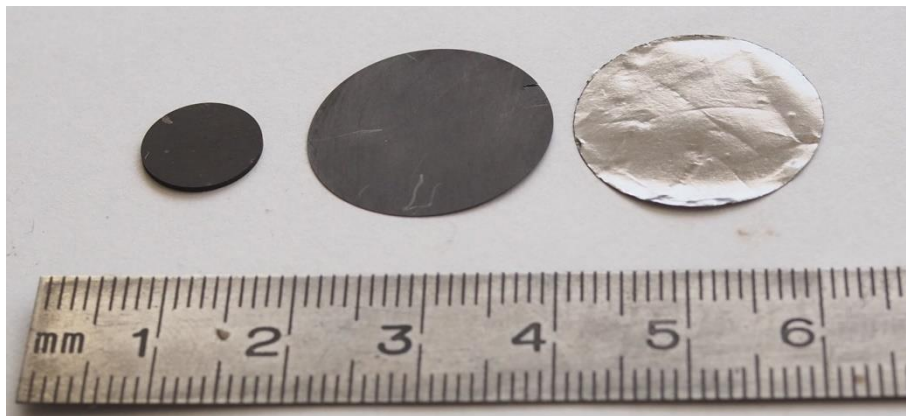


Figure 3.1 Photo of pristine samples. From left to right: polycrystalline graphite disc ( $\text{Ø} 10 \text{ mm}$ ,  $500 \mu\text{m}$  thick), polycrystalline graphite disc ( $\text{Ø} 20 \text{ mm}$ ,  $50 \mu\text{m}$  thick), flexible graphite disc ( $\text{Ø} 20 \text{ mm}$ ,  $21 \mu\text{m}$  thick).

Optical microscopy images of the surface of flexible graphite and polycrystalline graphite sample surfaces are presented in Figure 3.2.

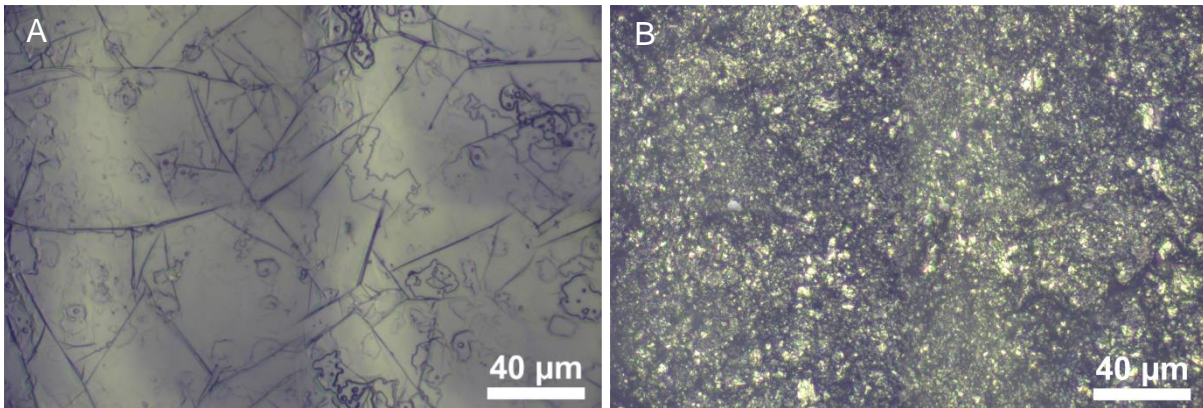


Figure 3.2 Optical microscopy images of flexible graphite (A) and polycrystalline graphite (B).

Two grades of glassy carbon having different manufacturing temperatures, Sigradur K and Sigradur G (HTW Hochtemperatur-Werkstoffe GmbH), were used as reference of disordered carbon material [65]. They are fabricated at 1000°C and 2800°C, respectively. The optical microscopy images of Sigradur K and Sigradur G samples are shown in Figure 3.3.

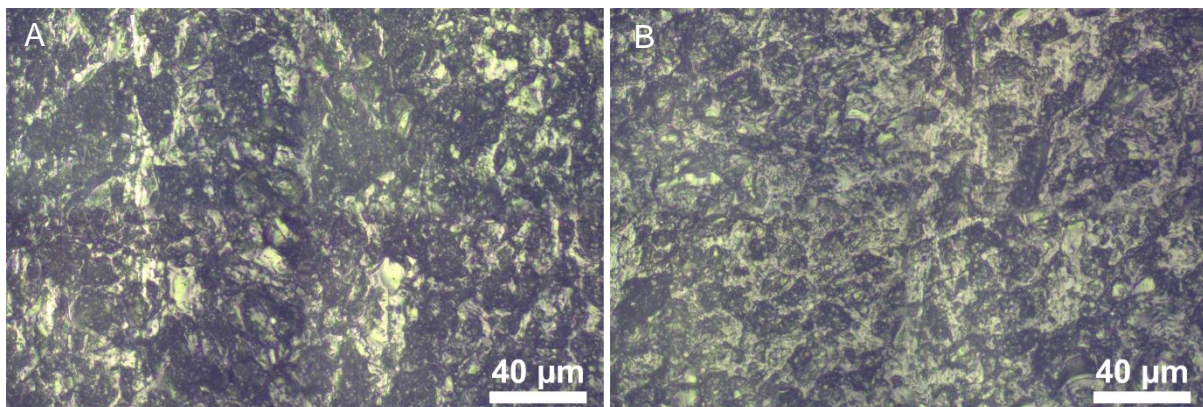


Figure 3.3 Optical microscopy images of Sigradur K (A) and Sigradur G (B) glassy carbon samples.

## 4 Ion beam irradiation

The ion beam irradiations were performed at the linear accelerator UNILAC at GSI Helmholtzzentrum für Schwerionenforschung. This facility can accelerate ions from  $^1\text{H}$  to  $^{238}\text{U}$  up to the energy of 11.4 MeV per nucleon (MeV/u).

The scheme of the UNILAC is presented in Figure 4.1. The ions, extracted from an ion source (for example, Penning Ionization Gauge (PIG) or Metal Vapor Vacuum Arc Ion Source (MEVVA)), are initially accelerated, bunched and focused in the Radio Frequency Quadrupole (RFQ). Then the beam passes through a gas stripper in order to achieve a higher charge state and is further accelerated in the Alvarez type drift tube linac. After acceleration the beam is delivered to the experimental area or is transferred to the heavy ion synchrotron SIS18 [66].

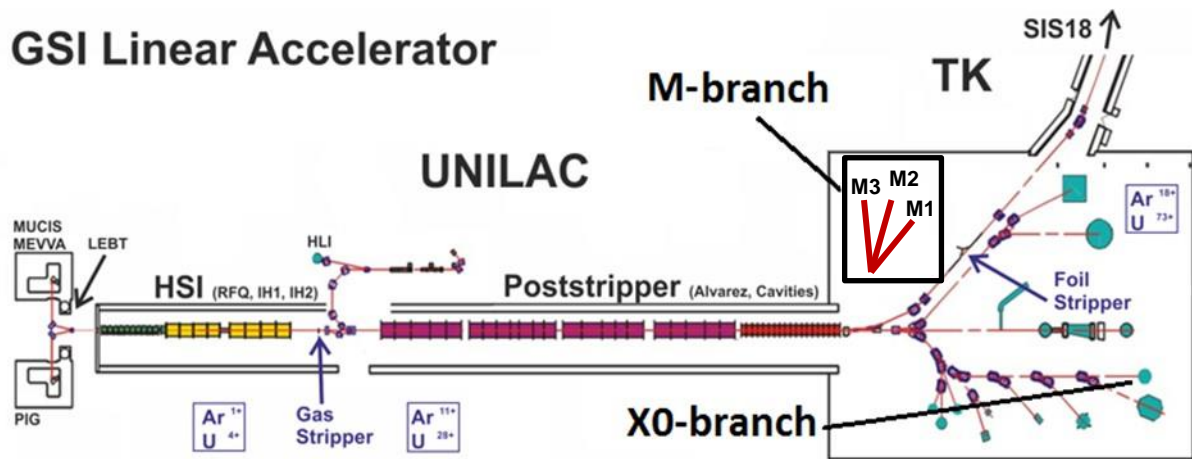


Figure 4.1 Scheme of GSI linear accelerator UNILAC, adapted from [66].

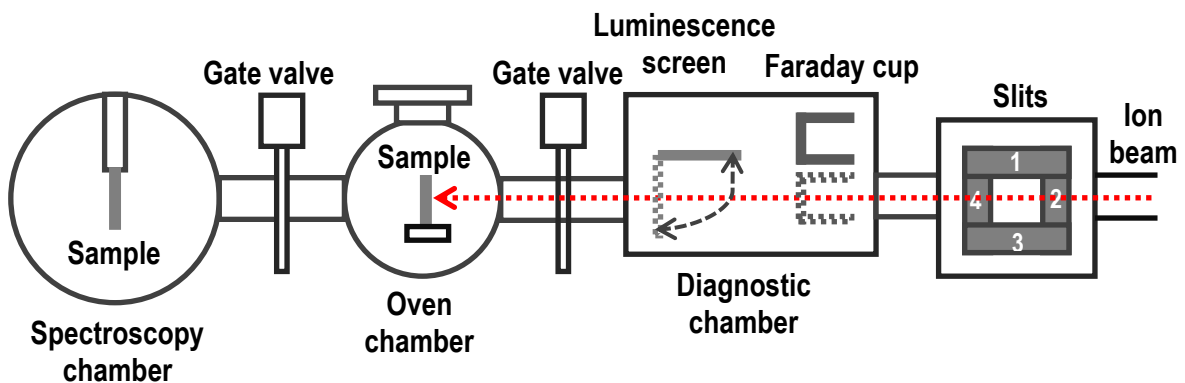


Figure 4.2 Schematic structure of M3-beamline at UNILAC.

All studied samples were irradiated at the M3-beamline of M-Branch experimental area. Figure 4.2 shows the schematic structure of the M3-beamline. Coming from the accelerator, the ions are passing through dipole and quadrupole magnets, used for bending and focusing



---

the beam, and a slit system, which shapes the beam and is used for the beam flux monitoring during irradiation. Behind the diagnostic chamber, the sample is mounted in the oven or multipurpose spectroscopy chamber.

Prior to the irradiation, the size and position of the beam spot is controlled by means of a luminescence target made of Cr-doped  $\text{Al}_2\text{O}_3$ , which glows under irradiation. When the beam spot is defined in a way that the beam covers homogeneously the whole sample surface (see Figure 4.3), the flux is calibrated via the beam induced current in a Faraday cup and on the slits. During irradiation of the samples the Faraday cup is removed and the flux is monitored by the slit current, assuming no changes in the beam shape and position.

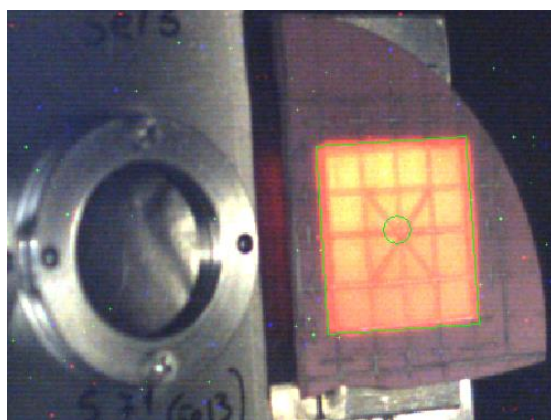


Figure 4.3 Example of a  $2\text{ cm} \times 2\text{ cm}$  beam spot checked on a luminescence screen (right) next to a sample holder (left).

The irradiated samples were fixed on an Al holder on the horizontally moving stage in the oven chamber. The irradiation was done in vacuum at  $10^{-6}$  -  $10^{-7}$  mbar at room temperature under normal beam incidence. The sample temperature during irradiation was monitored using an IR camera.

Depending on the ion source, the beam had 2 different time structures. C, Ca, Xe and Au ion beams from the PIG source were operated in a heavy duty cycle with a frequency of 10-40 Hz and 1-3 ms pulse length. The MEVVA ion source used for the U ion beam is operated in the high flux mode, which works at low duty cycles with a frequency of 0.5 – 1 Hz and a pulse length of 0.2 - 0.5 ms.

A summary of the irradiation conditions for flexible and polycrystalline graphite samples is presented in Table 4.1. Flexible graphite samples were irradiated in a stack of 3 samples (see Figure 5.6a). One set of flexible graphite samples was irradiated with 4.8 MeV/u Au ions in stacks consisting of  $10\ \mu\text{m}$  thick pyrolytic graphite sheets (PGS) from Panasonic with a density

of 2.13 g/cm<sup>3</sup> [67]. Samples of thickness less than the ion range are completely penetrated by the ion beam.

Table 4.1 Irradiation parameters for flexible graphite (FG) and polycrystalline graphite (PG) disc samples. Ion range is calculated using SRIM-2013 code with an uncertainty of about 10% [68]. Flux and fluence uncertainties are assumed to be between 10 and 20%.

Sample	Ion	Energy (MeV/u)	Ion range ( $\mu\text{m}$ )	Flux (ions/(cm <sup>2</sup> s))	Fluence range (ions/cm <sup>2</sup> )
FG Ø 20 mm $l=21\ \mu\text{m}$	<sup>48</sup> Ca	4.8	43.5	$(2.5-3)\times 10^9$	$1\times 10^{11}\dots 2.27\times 10^{14}$
	<sup>129</sup> Xe		39.6	$4\times 10^9$	$1\times 10^{11}\dots 1\times 10^{14}$
	<sup>197</sup> Au		46.7	$2\times 10^9$	$1\times 10^{11}\dots 1.34\times 10^{14}$
				$(4-10)\times 10^9$	$1\times 10^{12}\dots 4\times 10^{13}$
	<sup>238</sup> U		47.2	$2\times 10^9$	$5\times 10^{11}\dots 1.4\times 10^{13}$
PG Ø 20 mm $l=40-60\ \mu\text{m}$	<sup>12</sup> C	5.9	108.9	$5\times 10^9$	$1\times 10^{11}\dots 5\times 10^{13}$
	<sup>48</sup> Ca	4.8	55.4	$2\times 10^9$	$1\times 10^{11}\dots 5\times 10^{13}$
	<sup>197</sup> Au	4.8	57.2	$3\times 10^9$	$2\times 10^{11}\dots 1\times 10^{13}$
				$2\times 10^9$	$1\times 10^{11}\dots 5\times 10^{13}$
				$9\times 10^9$	$1\times 10^{12}\dots 5\times 10^{13}$
		5.9	67.9	$1.5\times 10^9$	$1\times 10^{11}\dots 1\times 10^{13}$
PG Ø 10mm $l=0.04-0.9\ \text{mm}$	<sup>12</sup> C	5.9	108.9	$5\times 10^9$	$1\times 10^{11}\dots 5\times 10^{13}$
	<sup>48</sup> Ca	4.8	55.4	$5\times 10^9$	$1\times 10^{11}\dots 1\times 10^{14}$
	<sup>197</sup> Au	4.8	57.2	$3\times 10^9$	$1\times 10^{11}\dots 5\times 10^{13}$
		5.9	67.9	$1.5\times 10^9$	$1\times 10^{11}\dots 5\times 10^{13}$
	<sup>238</sup> U	4.8	57.7	$2\times 10^9$	$5\times 10^{11}\dots 5\times 10^{13}$

---

## 5 Characterization

---

This chapter shortly describes the characterization techniques used for the analysis of the radiation damage in flexible and polycrystalline graphite, including experimental details of scanning electron microscopy, Raman spectroscopy, laser flash analysis, and photothermal radiometry.

---

### 5.1 Scanning electron microscopy

---

Scanning electron microscopy (SEM) is a common technique used for the sample topography [69,70]. The focused electron beam scans the sample surface in a raster mode and based on the combination of the beam position with the detected signal a sample image is produced. In the region, where the beam interacts with medium, called the interaction volume, different processes take place, causing the emission of secondary, backscattered and Auger electrons as well as characteristic, continuum and fluorescent X-rays (see Figure 5.1). The penetration depth of the electron beam increases with increasing electron kinetic energy and decreases with the atomic number  $Z$  and the density  $\rho$  of a sample.

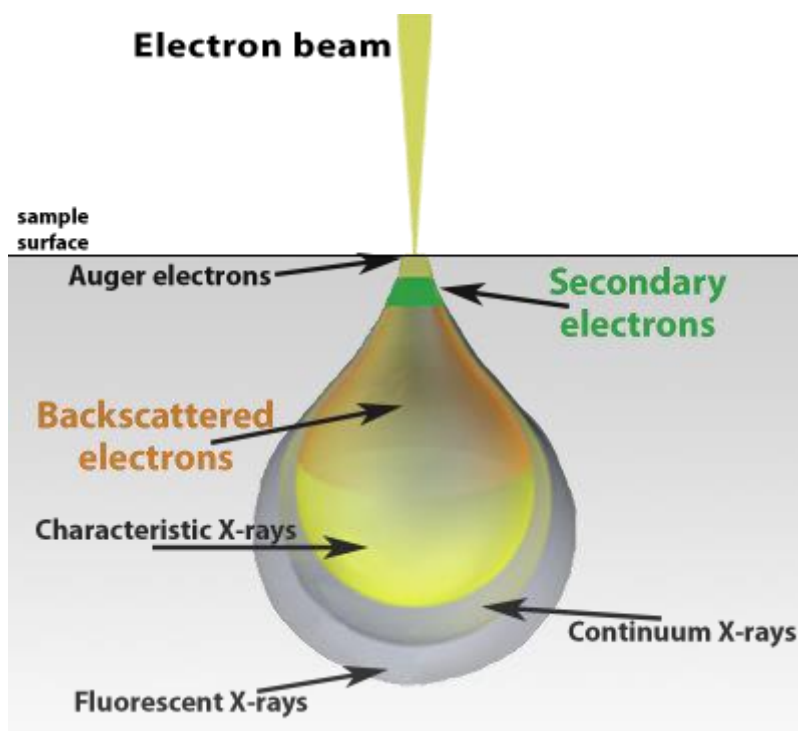


Figure 5.1 Scheme of processes in the interaction volume of a sample exposed to the electron beam, adapted from [71].

Secondary electrons (SE) are produced in the process of inelastic scattering of the electron beam and typically have a low energy and relatively small scattering angles. This leads to the

---

fact, that most of the secondary electrons are stopped in the sample volume, and only those generated just below the surface ( $< 2$  nm) can escape and be detected. Thus, the SE image provides information mainly from the surface structure (topography) rather than from the bulk. The secondary electron yield depends on the angle between the incoming beam and the surface, which is minimum in the case of a perpendicular incidence and increases with larger angles between the primary beam and the surface normal. Because of this orientation dependence of the yield, tilted, protruding or recessed features usually appear with a brighter outline in a SE image.

SEM images, presented in the thesis were obtained using the secondary electrons Everhart Thornley Detector. The low magnification images were measured using a SEM Philips XL30 FEG with an operating voltage of 10 kV. The high magnification images were taken at JEOL JSM 7600F operated at 5 kV.



## 5.2 Raman spectroscopy

Raman spectroscopy is related to inelastic scattering of light and is commonly used for chemical and structural characterization of material. It provides information on vibrational modes of molecules excited to a virtual state by absorbed photons. The schematic representation of different light scattering processes, depending on the energy level to which a molecule relaxes after emitting a photon, is shown in Figure 5.2. The most probable scattering process is elastic also called Rayleigh scattering. During this process, the system relaxes back to the initial state by emitting a photon with the same energy (frequency) as the absorbed one. The scattering is called inelastic or Raman scattering when the emitted photon has a different energy, corresponding to the relaxation from the excited state to the level with higher or lower energy level. The probability of this scattering is much lower, what causes several orders of magnitude weaker intensity of the emitted light. If the emitted photon has a lower energy, the energy difference is called Stokes shift. The photon emission with a higher energy is called anti-Stokes shift.

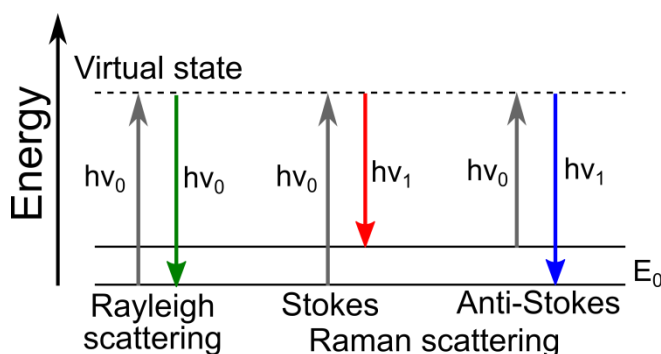


Figure 5.2 Energy level representation of elastic (Rayleigh) and inelastic (Raman) scattering.

The Raman shift  $\Delta\omega$ , usually given in wavenumbers ( $\text{cm}^{-1}$ ), can be calculated using equation 5.1, where  $\lambda_0$  and  $\lambda_1$  are the wavelength of the excitation and emission light, respectively.

$$\Delta\omega(\text{cm}^{-1}) = \left( \frac{1}{\lambda_0(\text{nm})} - \frac{1}{\lambda_1(\text{nm})} \right) \frac{10^7 \text{ nm}}{\text{cm}} \quad 5.1$$

Raman spectroscopy is widely used for the characterization of carbon based materials. A recent summary of accumulated knowledge on this technique and application to structural analysis of different types of graphite can be found in the following works [72–77].

The typical Raman spectra of flexible and polycrystalline graphite before and after irradiation are shown in Figure 5.3. The list of all deconvoluted peaks is presented in Table 5.1. The main band, so called G-peak, which is always observed in Raman spectra of carbon with a  $\text{sp}^2$  structure, is caused by the  $\text{E}_{2\text{g}}$  vibration and has a Raman shift of  $1580 \text{ cm}^{-1}$ . The Raman band

at about  $1360\text{ cm}^{-1}$  (D-band) is usually connected to the breathing vibrations of carbon rings,  $A_{1g}$ , and becomes active with the introduction of defects in the lattice. The D band of well oriented graphite (HOPG, flexible graphite) is asymmetric and consists of the D1-peak ( $1355\text{ cm}^{-1}$ ) and the D2-peak ( $1375\text{ cm}^{-1}$ ). They originate from graphite edge plane and in-plane defects, respectively [12,78]. Both D1 and D2 peaks can be used for the analysis of polycrystalline graphite Raman spectra, although in this case the D-band has a symmetric shape. The D'-peak at  $1620\text{ cm}^{-1}$  is observed only in damaged graphite. The second order Raman bands consist of several overtones of the first order Raman bands. The high intensity second order Raman band is located at about  $2720\text{ cm}^{-1}$  and consists of two peaks 2D1 and 2D2. The appearance and energy dispersive behavior of D, D' and 2D bands can be explained by a double resonance process [79–81]. The D' band is due to an intravalley scattering process involving a phonon and a defect. D and 2D bands are caused by an intervalley scattering between K and K' points in the Brillouin zone (see Figure 2.2 and Figure 2.3) by a phonon plus a defect or by two phonons, respectively. The peaks D3 (also called A,  $\sim 1500\text{ cm}^{-1}$ ), D4 ( $\sim 1250\text{ cm}^{-1}$ ) and D5 (also called T,  $\sim 1100\text{ cm}^{-1}$ ) around D-band are usually only observed on highly disordered graphite [82,83]. These peaks are also present in nanocarbons with high curvature of basal planes (carbon onions). They are required for a good fit, however there is no data available of their quantitative contribution. The same applies to the second order D+D' band, which is also called D+G.

Table 5.1 List of deconvoluted peaks of graphite Raman spectra recorded with a laser of wavelength  $\lambda=473\text{ nm}$ .

First order		Second order	
Peak	Raman shift ( $\text{cm}^{-1}$ )	Peak	Raman shift ( $\text{cm}^{-1}$ )
D5	1080-1150	D1+D5	2430-2440
D4	1240-1260	D2+D5	2455-2480
D1	1355-1362	2D1	2702-2721
D2	1372-1380	2D2	2444-2750
D3	1460-1500	D+D'	2950-2965
G	1578-1585		
D'	1614-1623		

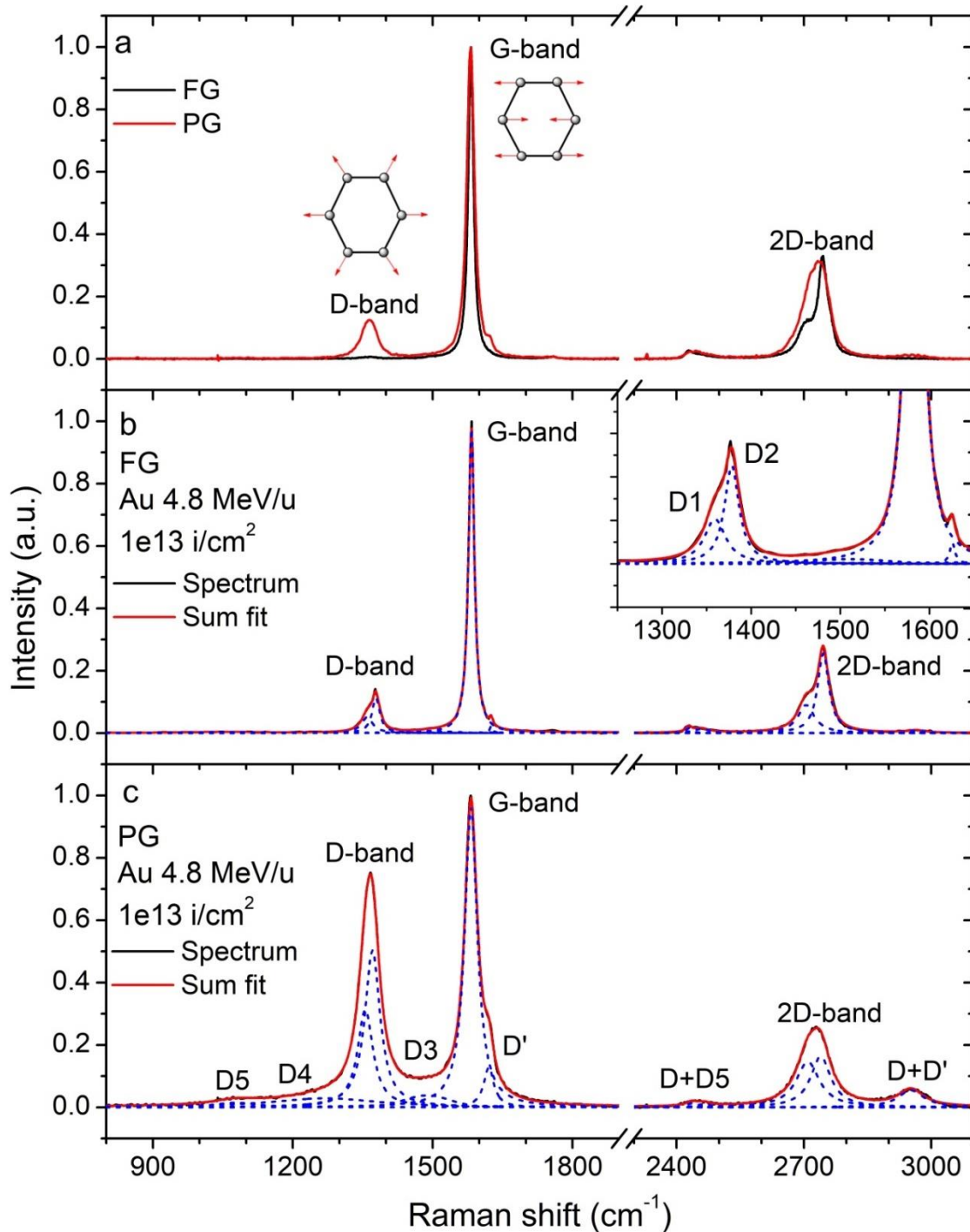


Figure 5.3 Raman spectra and fitted peaks of pristine (a) and ion irradiated flexible (b) and polycrystalline (c) graphite with main vibration modes. The inset graph shows a zoomed view on the D-band.

The intensity of the Raman spectra is proportional to the material concentration and overall depends on the setup parameters, e.g. laser power and polarization, grating, aperture size, etc. Thus, for the analysis the Raman spectra relative intensities are typically used instead of absolute intensities of individual peaks. The width of the Raman bands is connected to the lifetime of the corresponding scattering process. The most common parameters used for

analysis of the graphite Raman spectra are the ratios of peak intensities  $I_D/I_G$  and  $I_D/I_D$ , area ratio  $A_D/A_G$ , and the G band linewidth  $\Gamma_G$ .

Raman spectroscopy is mostly applied for quantification of two types of defects in graphene and graphite: point defects (0D) and line defects (1D). For this purposes either the ratio  $I_D/I_G$  or  $A_D/A_G$  is used. The recent approach to connect structural defects of graphene with recorded Raman spectra is called “local activation model”. It was first proposed for the characterization of point defects induced by ion beam irradiation of graphene [14,84,85], and later applied also for the estimation of crystallite size  $L_a$  [86]. The scheme, illustrating the model is shown in Figure 5.4. In this model one considers three sets of parameters. The first set consist of the so-called structural parameter  $r_s$ , describing the radius of a disordered region around point defects, and the width of the disordered linear region at crystallite boundary  $l_s$ . The second group includes the dynamical parameters  $r_A$  and  $l_A$ , defining electron coherence length and the limit of the “activated region”. On a distance larger than  $r_s$  ( $l_s$ ) but smaller than  $r_A$  ( $l_A$ ) the lattice is not disturbed, but the proximity of defects causes changes in the electronic structure of graphite and allows a double resonance mechanism responsible for the D band. The third group of parameters consists of the Raman cross-sections for structural disordered and activated regions  $C_S$  and  $C_A$  for point and line defects.  $L_D$  is the average distance between point defects and in the case of ion irradiation of graphite can be connected to the accumulated fluence  $\Phi$  as  $L_D = 1/\sqrt{\Phi}$ . The evolution of  $I_D/I_G$  for 0D and 1D defects is described by equation 5.2 and 5.3, respectively [14,84–86]. These equations were obtained by using the mentioned phenomenological model, considering contributions to the intensity of the D-peak from the disordered and activated fraction areas of the entire probed region. As the intensity of the G-band depends on the excitation laser energy  $E_L$  as  $E_L^4$ , the ratios  $I_D/I_G$  and  $A_D/A_G$  are multiplied by  $E_L^4$  in order to eliminate the dependence on the excitation energy and to make it possible to compare with other published data.  $E_L$  can be calculated from the laser wavelength using equation 5.4.

$$\frac{I_D}{I_G} E_L^4 = C_A \frac{r_A^2 - r_S^2}{r_A^2 - 2r_S^2} \left( e^{-\frac{\pi r_S^2}{L_D^2}} - e^{-\frac{\pi(r_A^2 - r_S^2)}{L_D^2}} \right) + C_S \left( 1 - e^{-\frac{\pi r_S^2}{L_D^2}} \right) \quad 5.2$$

$$\frac{I_D}{I_G} E_L^4 = \frac{1}{L_a^2} \left[ C_A l_A (L_a - 2l_S) \left( 1 - e^{-\frac{2(L_a - 2l_S)}{l_A}} \right) + 4C_S l_S (L_a - l_S) \right] \quad 5.3$$

$$E_L (eV) = \frac{hc}{\lambda} \approx \frac{1239.8}{\lambda (nm)} \quad 5.4$$

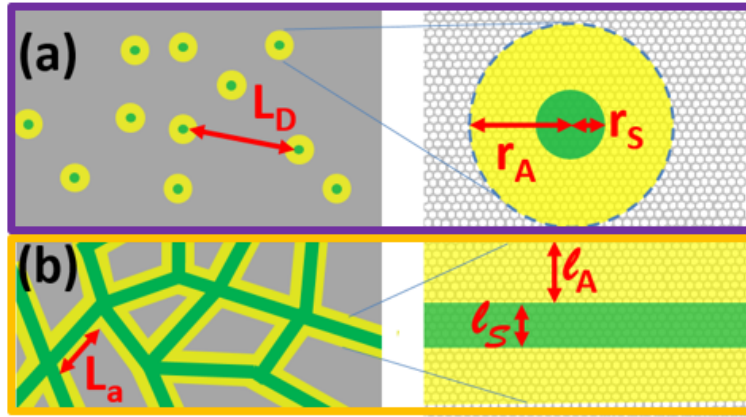


Figure 5.4 Local activation model for point defects (a) and crystallite boundaries (b), adapted from [73]. The right graphs show zoomed in schemes of the 0D and 1D defects. The disordered and activated regions are marked green and yellow, respectively.

In the limit of large crystallite size  $L_a \gg l_S$ , equation 5.3 can be simplified to a simple dependence on  $I_D/I_G$ , similar to the one which was used in earlier works [87–89]

$$L_a \approx \frac{(490 \pm 100)}{E_L^4} \left( \frac{I_D}{I_G} \right)^{-1} \quad 5.5$$

Ferrari and Robertson observed a change in the proportionality between  $L_a$  and  $I_D/I_G$  in the highly-disordered regime when  $L_a$  goes to small values and they proposed the relation  $I_D/I_G \propto L_a^2$  for  $L_a < 2$  nm [90]. They describe this stage as a transition from well-ordered graphite towards nanocrystalline graphite (stage 1) with a subsequent transition towards amorphous carbon (stage 2). Equations 5.2 and 5.3 can describe the evolution of both stages 1 and 2 simultaneously in terms of point and line defects, respectively.

In their recent work, Cançado et al [91] proposed a way of disentangling the contribution of point and line defects coexisting in graphene-based materials. In order to do so, it is necessary to introduce an additional independent spectral parameter, which is the G band linewidth  $\Gamma_G$ . The full width at half maximum of the G-band ( $\text{FWHM}(G) = \Gamma_G$ ) monotonously increases with structural disorder in contrast to  $I_D/I_G$  and  $A_D/A_G$ . Thus, the combination of these two quantities allows the unique characterization of structural disorder of graphene-based materials. The linewidth  $\Gamma_G$  dependence on the parameters  $L_a$  and  $L_D$  is described by equation 5.6:

$$\Gamma_G(L_a, L_D) = \Gamma_G(\infty) + C_\Gamma e^{-\frac{\xi}{l_{ph}}} \quad 5.6$$

where  $\Gamma_G(\infty)$  was found to be  $14 \text{ cm}^{-1}$ ,  $C_\Gamma$  equals to  $87 \text{ cm}^{-1}$ , the phonon coherence length  $l_{ph}$  is 16 nm.  $\xi$  can be replaced by  $L_a$  in the case of only line defects and by  $\alpha L_D$  for point defects (the fit value  $\alpha$ , describing experimental data, is 10). For samples with both kinds of defects  $\xi$  is selected as the minimum between  $L_a$  and  $\alpha L_D$ .

An analytical expression of  $A_D/A_G$  as a function of  $L_a$  and  $L_D$  for samples with both point and line defects is given by equation 5.7, coming from a combination of equations 5.2 and 5.3:

$$\begin{aligned}
 \left(\frac{A_D}{A_G}\right) E_L^4(L_a, L_D) = & \\
 = C_S^{0D} \left(1 - e^{-\frac{\pi r_s^2}{L_D^2}}\right) + 4C_S^{1D} l_s \frac{(L_a - l_s)}{L_a^2} e^{-\frac{\pi r_s^2}{L_D^2}} & \\
 + 2\pi C_A^{0D} r_A \frac{(r_A - r_s)}{L_D^2} \left(1 - 4l_s \frac{(L_a - l_s)}{L_a^2}\right) e^{-\frac{\pi r_s^2}{L_D^2}} & \quad 5.7 \\
 + 2C_A^{1D} l_A \frac{(L_a - 2l_s)}{L_a^2} \left(1 - e^{-\frac{L_a - 2l_s}{l_A}}\right) e^{-\frac{\pi r_s^2}{L_D^2}} &
 \end{aligned}$$

The typical behavior of  $\left(\frac{A_D}{A_G}\right) E_L^4$  as a function of FWHM(G) for damaged graphene is presented in Figure 5.5. The increase of 0D type defects is characterized by a steep increase of  $\left(\frac{A_D}{A_G}\right) E_L^4$  values, while FWHM(G) remains around 15-30  $\text{cm}^{-1}$  before a high degree of amorphization is achieved. Changes of the in-plane crystallite size, i.e. development of 1D type of defects, are linked to a significant increase of FWHM(G) with relatively low values of  $\left(\frac{A_D}{A_G}\right) E_L^4$ . A certain combination of the FWHM(G) and  $\left(\frac{A_D}{A_G}\right) E_L^4$  values laying in the most part of the area limited by the lines in Figure 5.5 almost unambiguously corresponds to a simultaneous contribution of both 0D and 1D defects with defined values of  $L_a$  and  $L_D$ .

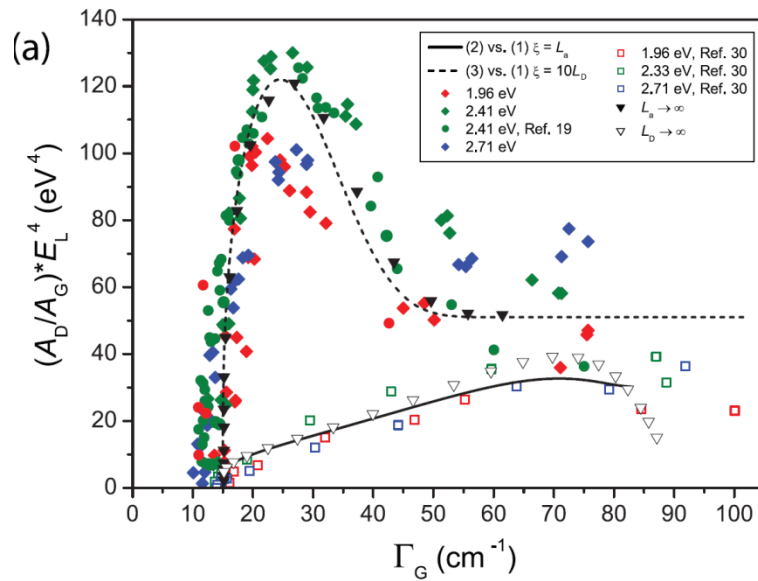


Figure 5.5 The evolution of  $A_D/A_G \cdot E_L^4$  as a function of FWHM(G) of graphene materials with dominant presence of point defects (dashed line and solid symbols) and 1D line defects (solid line and open symbols), adapted from [91].

The ratio  $I_D/I_{D'}$  does not change with the number of defects, but can be used for defect type determination [92,93]. Considering equation 5.2 for both the D- and D'-bands in the low defect concentration limit, the ratio  $I_D/I_{D'}$  has the following form [93]:

$$\frac{I_D}{I_{D'}} \simeq \frac{C_{A,D}(r_{A,D}^2 - r_{S,D}^2)}{C_{A,D'}(r_{A,D'}^2 - r_{S,D'}^2) + C_{S,D'}r_{S,D'}^2} \quad 5.8$$

According to [92], the ratio  $I_D/I_{D'}$  is minimal for boundary-like defects, increases for point defects and reaches maximum for defects associated with  $sp^3$  hybridization, taking values of approximately 3.5, 7 and 13 (measured at an excitation energy of 2.41 eV), respectively. However, the excitation energy can affect the ratio values for different defect species.

Larouche and Stansfield introduced a new Raman graphitization index  $R_{Tor}$ , called the tortuosity ratio, quantifying the effect of tortuosity in the graphene layers [89]. Taking into account the dispersive behavior, the tortuosity ratio is defined as:

$$R_{Tor} = \left(\frac{E_L(eV)}{2.41}\right)^4 \left(\frac{2A_{2D}}{A_G}\right) \quad 5.9$$

By multiplication of  $R_{Tor}$  by the in-plane crystallite size  $L_a$ , one can obtain the average continuous graphene length  $L_{eq}$  (Equation 5.10), which describes the total length of several planar graphene units interconnected into a larger curved graphene layer.

$$L_{eq} = R_{Tor} \cdot L_a \quad 5.10$$

In order to adapt the experimental data with D-band fitted with 2 peaks to the previously developed models, obtained for a single symmetric D-peak, the  $I_D$  value is taken as a maximum intensity of summed D1 and D2, and  $A_D$  is a sum of  $A_{D1}$  and  $A_{D2}$ .

### Experimental setup

A commercial Raman spectrometer LabRAM HR 800 (Horiba Jobin Yvon) was used for spectroscopy measurements. The measurements were performed using a Cobolt Blues CW diode pumped laser with a wavelength of  $\lambda_0=473$  nm ( $E_L=2.62$  eV). The laser power on the sample surface was 5-10 mW, which did not cause any material modification. Depending on the sample roughness, x100, x50 and long working distance x50LWD objectives were used. The theoretical radius of the laser beam spot on a sample surface is defined by the laser wavelength  $\lambda_0$  and the objective numerical aperture N.A.:

$$R \approx \frac{0.6\lambda_0}{N.A.} \quad 5.11$$



However due to a non-ideal optical system, the real beam spot had a larger diameter of  $2.5\ \mu\text{m}$  for the x100 objective (N.A.=0.9) and  $4.5\ \mu\text{m}$  for both x50 (N.A.=0.75) and x50LWD objectives (N.A.=0.45).

The probing depth of Raman spectroscopy in graphite is limited to  $\sim 50\ \text{nm}$  for the used wavelength. The backscattered light is passing through an objective, a confocal hole with size of  $100\ \mu\text{m}$  and a monochromator. After dispersion on the grating with  $1800\ \text{grooves}/\text{mm}^2$ , the light comes to a Peltier cooled CCD detector. The calibration of the spectrometer was done using the  $520\ \text{cm}^{-1}$  Raman band of a Si sample.

For getting structural information along the ion beam path in graphite, the Raman spectra of flexible graphite samples were measured on 25-36 points on the sample at a distance of at least  $50\ \mu\text{m}$  from each other in the central area of the front and back side of each sample. This was applied for set-ups with very thin samples, where the beam was penetrating stacks of samples. The Raman spectra of polycrystalline graphite were recorded along five profiles on freshly fractured sample cross-sections, each with a length of  $100\ \mu\text{m}$ , normal to the irradiated surface and along the incoming ion direction, with a step of  $2\ \mu\text{m}$ . Figure 5.6 provides a sketch of Raman spectroscopy measurements on flexible graphite (a) and polycrystalline graphite (b) samples. All measurements were performed using the reflection autofocus. The Raman spectra were measured in the wavenumber range from  $100$  to  $3200\ \text{cm}^{-1}$  using standard LabSpec 5 and LabSpec 6 software by Horiba Jobin Yvon [94]. The acquisition time was selected to 15 seconds for flexible graphite and to 45 seconds for polycrystalline graphite in order to get an average signal-to-noise ratio for the G-peak of at least 20. During the measurements, each spectral window was recorded 2 times with subsequent averaging. The background correction, normalization and fitting of the Raman spectra was done using the Fityk 1.3.1 software [95].

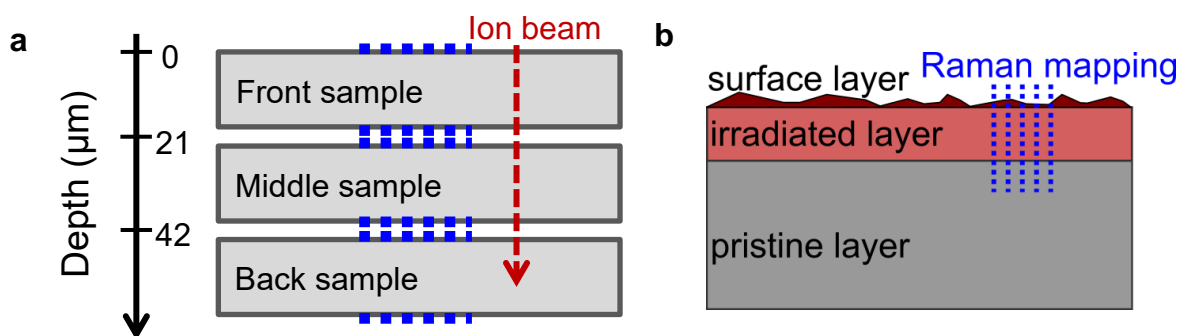


Figure 5.6 Scheme of Raman spectroscopy measurements of a) flexible graphite samples, b) cross-section of polycrystalline graphite samples. Blue dots illustrate probed positions on the samples.



### 5.3 Laser flash analysis

One of the commonly used methods to measure thermal diffusivity and conductivity is laser flash analysis, initially developed by Parker et al in 1961 [96]. This technique is operated in transmission geometry and is based on detecting a time-dependent temperature rise on the rear face of the sample after a short pulse laser shot on the front face. A short summary of this method can be found in [97].

Initially the analytical solution of the heat transport equation was developed for an ideal case, assuming an infinitely short pulse uniformly absorbed within short distance  $g$  of an insulated, homogeneous, isotropic sample of thickness  $l$ . In these conditions a flash causes a one dimensional heat flow through a sample with the temperature dependence on the rear surface as a function of time described by equation 5.12:

$$T(t) = T_{\infty} \left[ 1 + 2 \sum_{n=1}^{\infty} (-1)^n \frac{\sin(\pi n g/l)}{\pi n g/l} \exp(-n^2 \omega) \right] \quad 5.12$$

$$T_{\infty} = \frac{Q}{\rho c l}; \quad \omega = \frac{\pi^2 a t}{l^2} \quad 5.13$$

Here  $Q$  is the deposited energy, the product of the density and the specific heat  $\rho c$  is the volumetric heat capacity, and  $a$  is the thermal diffusivity. To deduce the thermal diffusivity it is necessary to measure the relative temperature change  $T/T_{\infty}$ . Considering a moment  $t_{1/2}$ , when half of the maximum temperature rise is reached on the rear face (see Figure 5.7), one gets the equation for the thermal diffusivity:

$$a = 1.37 \frac{l^2}{\pi^2 t_{1/2}} = 0.1388 \frac{l^2}{t_{1/2}} \quad 5.14$$

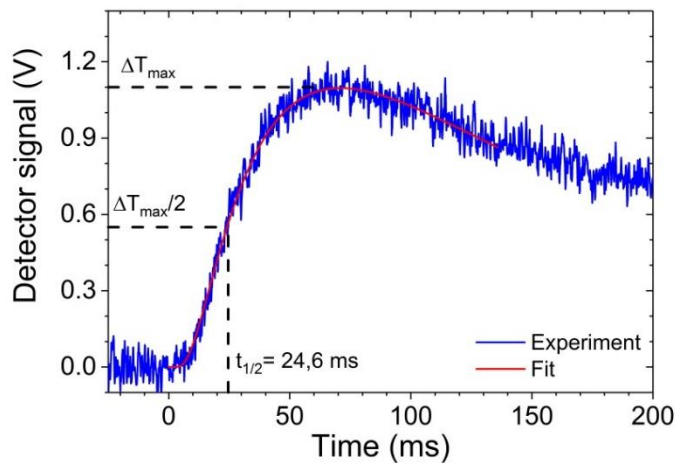


Figure 5.7 Temperature rise on the rear side of a sample induced by a laser flash.

Later the model was improved in order to take into account the effect of heat losses [98,99] and the finite duration of the laser pulse [99–104]. It is observed, that in the case of high conductive materials the characteristic thermal diffusion time, which is required for the heat to propagate from the front to the rear side of a sample, becomes comparable with the length of the laser pulse. The instant approximation is no longer valid and the obtained values of the thermal diffusivity show significant deviations from the reference. For example, Figure 5.8a shows the evolution of the recorded signal for polycrystalline graphite samples with thicknesses from 65  $\mu\text{m}$  to 1.8 mm. For the thickness below 1 mm, the temperature rise is very fast and the characteristic half-time becomes comparable with the pulse duration (0.3 ms). The apparent thermal diffusivity for polycrystalline graphite, as well as for Cu, Al and Ti samples of different thickness is shown in Figure 5.8b.

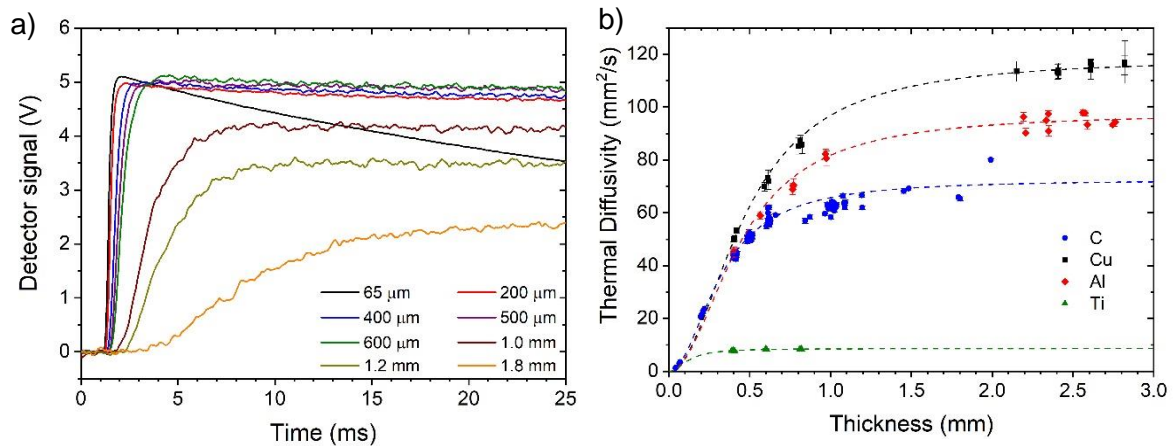


Figure 5.8 a) Recorded LFA signal for PG samples of different thickness measured with a laser pulse of 0.3 ms; b) Apparent thermal diffusivity values as a function of thickness for Cu, Al, C and Ti samples.

The laser flash analysis was further improved by using a more accurate experimental setup and a non-linear fit of the temperature rise curve at the rear side of a sample [105–107].

In order to measure thin and high conductive samples an in-plane laser flash set-up was developed [108–110]. In this type of measurements, a small central part of the front side of the sample is heated up by a laser pulse and the temperature rise is detected at an annular area with a larger radius (see Figure 5.9). This geometry increases the heat propagation distance and time, diminishing the effect of finite laser pulse. This method can also be applied for thermal diffusivity analysis of anisotropic samples.

Transversal laser flash analysis is also applicable for the measurements of multilayer samples. The early models were based on the same assumptions as in a single layer approach and estimated the unknown thermal diffusivity of one layer using a half-time  $t_{1/2}$  [111–114]. For



this type of calculations, it is necessary to know the thickness, density and heat capacity of the unknown layer and these parameters together with the thermal diffusivity for all other layers in the system. Further models were based on the non-linear fit of the temperature rise curve at the rear side of a sample [115–117]. This approach provides more reliable results and also allows considering thermal resistance at the interface between layers. Although just one fit parameter from the equation should be unknown, in some situation it is possible to use several uncorrelated parameters simultaneously.

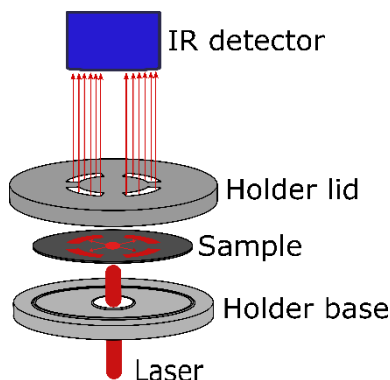


Figure 5.9 Scheme of an in-plane laser flash measurement.

### Experimental setup

Laser flash measurements were performed on a LFA427 device from NETZSCH. The setup is presented in Figure 5.10. The sample is located in the furnace chamber allowing operation from room temperature up to 2000°C in vacuum or protective atmosphere. A laser pulse with a wavelength  $\lambda=1064$  nm is coming to the chamber via fiber optics and illuminates the bottom surface of the sample through a fused silica window. Temperature evolution on the top surface of the sample is recorded using a liquid nitrogen cooled IR detector. The pulse length is adjustable from 0.3 to 1.2 ms with an applied laser voltage from 400 to 800 V, leading to a maximum energy of 25 J/pulse. An optical filter, which reduces the power of the laser down to 10%, can be used optionally in order to avoid overheating of sensitive samples.

The pristine and the irradiated samples were measured at 20°C with 10-20 laser shots. The pulse length and the laser voltage were adjusted for each series of measurements to have a signal amplitude of  $\sim 1$  V, providing a good signal-to-noise ratio without overheating the sample. The laser induced temperature increase would affect the measured value of thermal diffusivity. The influence of laser voltage and the pulse length on the thermal diffusivity values in the case of in-plane polycrystalline graphite measurements is demonstrated in Figure 5.11.

Thermal diffusivity of the measured samples was calculated using the NETZSCH Proteus<sup>®</sup> 6.0 software [118]. In most of the cases the best fit was achieved by the Cowan model, which takes into account the heat loss with a pulse correction.

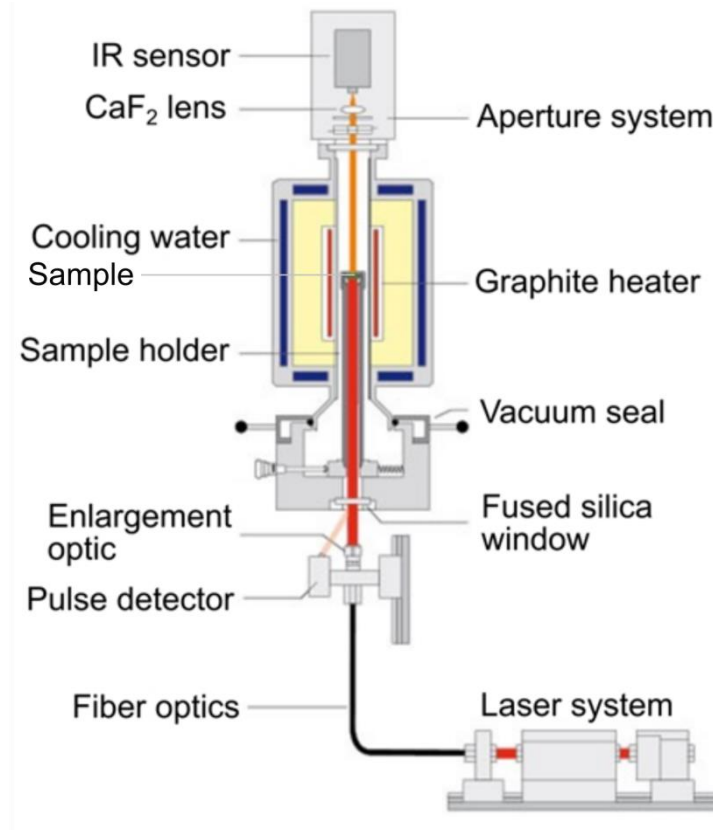


Figure 5.10 Scheme of laser flash setup LFA427 adapted from [119].

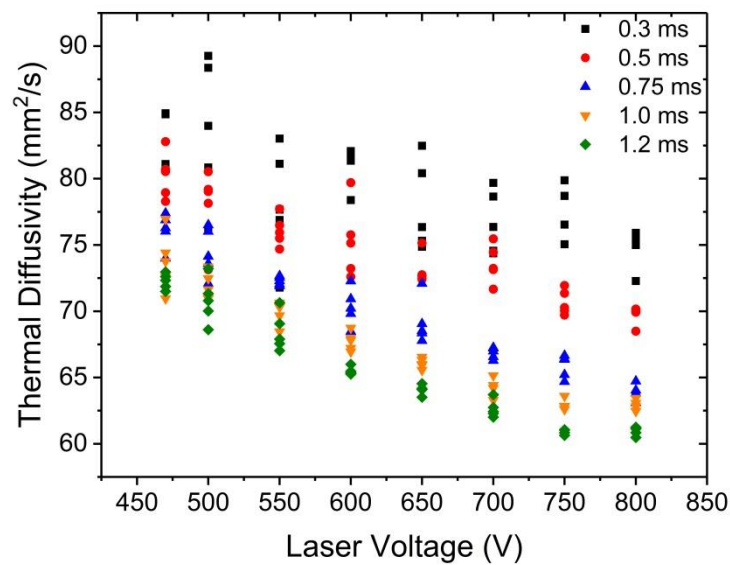


Figure 5.11 Measured in-plane thermal diffusivity of pristine polycrystalline graphite as a function of the laser voltage for different pulse length.

---

## 5.4 Photothermal radiometry

---

Photothermal radiometry (PTR) is a non-destructive material characterization technique based on the detection of the emitted IR response of materials to modulated heat excitation. This method was initially presented in 1979 by Nordal and Kanstad [120] and has been used for testing of optical and thermophysical properties. The basics and different aspects of PTR are described in [121].

Modulated heating of a material leads to the generation and propagation of so-called thermal waves. The term thermal wave is usually used because the induced temperature oscillations in the sample can be mathematically expressed in a similar way as highly damped waves, however during heat propagation there is no energy transfer that corresponds to the standard wave nature [122]. The penetration depth of the thermal waves defines the probing thickness at a given frequency and is given by the thermal diffusion length  $\mu = \sqrt{a/(\pi \cdot f)}$ , where  $a$  is the thermal diffusivity of a given material and  $f$  is the excitation laser frequency. Thus, scanning the frequency in a broad range from Hz to hundreds of kHz provides a depth resolved characterization of the sample. At low frequency the sample is thermally thin (sample thickness  $L \ll \mu$ ) and the approximated heat transport solution results in the amplitude being proportional to  $f^{-1}$  and the phase equal to  $-90^\circ$ . In the limit of high frequency, the sample is thermally thick ( $L \gg \mu$ ), the amplitude is proportional to  $f^{-\frac{1}{2}}$  and the phase is  $-45^\circ$ . A detailed theoretical description and limit cases can be found in [123].

The modulated heat transfer through a layered system can be described using the thermal quadrupole method [124]. The solution of the one dimensional heat diffusion equation is obtained by the Laplace transform. The temperature and the heat flux on the front and rear sample surfaces are connected via a system of equations represented in a matrix form (equation 5.15). A matrix  $Q_i$  corresponds to each layer of a sample where the matrix elements depend on the properties of the layer. In the case of a modulated laser excitation, these elements are defined as shown in equations 5.16 and 5.17.

$$\begin{pmatrix} T_{front}(z=0) \\ \varphi_{front}(z=0) \end{pmatrix} = \prod_{i=1}^n [Q]_i \begin{pmatrix} T_{rear}(z=L) \\ \varphi_{rear}(z=L) \end{pmatrix}, [Q]_i = \begin{pmatrix} A_i & B_i \\ C_i & D_i \end{pmatrix} \quad 5.15$$

$$\begin{cases} A_i = D_i = \cosh(\sigma_i L_i) \\ B_i = \sinh(\sigma_i L_i) / (k_i \sigma_i) \\ C_i = k_i \sigma_i \cdot \sinh(\sigma_i L_i) \end{cases} \quad 5.16$$

$$\sigma_i = \sqrt{\frac{2\pi i \cdot f}{a_i}} = \frac{1+i}{\mu_i} \quad 5.17$$

Based on theoretical approaches presented in previous work [33,123], the following two independent parameters have to be considered:

(1) the thermal effusivity  $e_i$  (Eq. 5.18) and (2) the product  $L_i \cdot a_i^{-1/2}$ .

$$e_i = \sqrt{k_i \rho_i c_{pi}} = \rho_i c_{pi} \sqrt{a_i} \quad 5.18$$

The thermal effusivity is a function of the thermal conductivity  $k_i$ , density  $\rho_i$ , and specific heat capacity  $c_{pi}$  of each layer.  $L_i$  and  $a_i$  denote the layer thickness and its thermal diffusivity, respectively. The Gauss-Newton algorithm was used to adjust the theoretical model to the experimental data in order to extract the thermophysical properties. To ensure the reliability of the fit and the uniqueness of the obtained fit values, the relative sensitivity [125,126] of a function  $F = F(p_1, p_2, \dots, p_n)$  to the fitting parameters  $p_i$  was estimated by

$$S_p = \frac{\partial F / F}{\partial p / p} = \frac{\partial(\ln F)}{\partial(\ln p)} \quad 5.19$$

It provides the relative variation of a function with respect to the relative variation of one variable, while other parameters remain fixed. Sensitivity value  $S_{F,p} = 0$  means a small variation of parameter  $p$  at the corresponding frequency does not change the resulting function  $F$ . In the case of  $S = -1$ , the function  $F$  depends on the parameter  $p$  as  $F \propto p^{-1}$ . Overlapping or symmetrical shape of the sensitivity curves, corresponding to different parameters, indicates their direct correlation.

### Experimental setup

To analyze the thermophysical properties of the irradiated layers, all samples were measured using a frequency scanning PTR setup (see Figure 5.12) at the Mechanical and Thermal Engineering Lab of The University of Reims Champagne-Ardenne, France. The sample surface is heated with a continuous laser (in this case with a wavelength of 532 nm) modulated in the frequency domain via an acousto-optic modulator (AOM model AA.MTT.AR 05) in the range of 1 Hz to 100 kHz. A beam shaper is used to produce a homogeneous excitation laser beam spot covering the whole sample surface. The infrared radiation emitted from the sample surface is transferred by two off-axis parabolic gold-coated mirrors (Edmund Optics) to a liquid-nitrogen cooled HgCdTe photoconductive detector (Kolmar Technologies, KMPV 11-1-

J1/DC) with a  $1 \text{ mm}^2$  active area. The detector has an antireflection-coated Ge entrance window with sensitivity for IR radiation of wavelength between  $5$  and  $12 \mu\text{m}$ . The detector output signal is analyzed by a lock-in amplifier (Stanford Research Systems: SR865), providing temperature amplitude and phase in relation to the excitation frequency. The signal depends on the variation of the temperature at the surface of the sample and is linked to the thermophysical properties of the investigated material layers. The instrumental dependence of the signal of the detection system on frequency was corrected by normalization of the recorded signal to the electro-optical transfer function (TRF). The low frequency part of TRF, which takes into account the influence of the lock-in amplifier electronic system, was obtained by shooting a laser directly to a photodiode. The high frequency part of TRF, correcting the effect of the IR detector, was determined by measuring a reference material (polished Ti-6Al-4V sample). The fitting of the experimental amplitude and phase to the heat transfer model, described in terms of thermal quadrupoles, sensitivity analysis and uncertainty calculations were done using GNU Octave software.

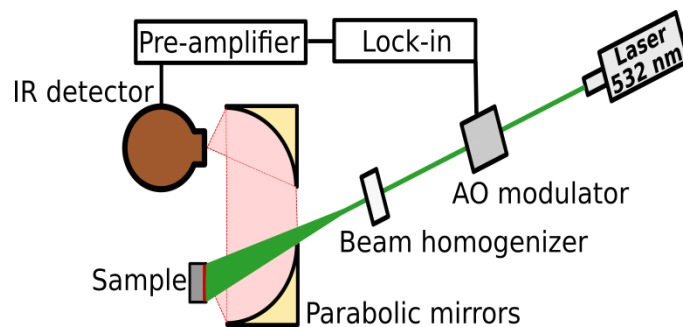


Figure 5.12 Scheme of photothermal radiometry setup.



---

# Results and Discussions

---

## 6 Structural modifications caused by ion irradiation

---

This chapter is focused on the structural changes induced by swift heavy ion irradiation in well-oriented flexible graphite and quasi-isotropic polycrystalline graphite. The morphology of ion-beam irradiated graphite was studied using scanning electron microscopy and Raman spectroscopy.

---

### 6.1 Well-oriented graphite

---

---

#### 6.1.1 Scanning electron microscopy

---

Selected SEM images of pristine (a, c) and 4.8 MeV/u Au ion irradiated (b, d) flexible graphite samples are presented in Figure 6.1. The images show randomly-shaped multilayered flakes of graphite. The low magnification SEM image of the beam facing flexible graphite sample irradiated with Au ions at a fluence of  $1 \times 10^{13}$  ions/cm<sup>2</sup> (Figure 6.1b) has a larger amount of more pronounced bright contrast features, corresponding to the folded edges of graphite flakes as it is seen at high magnification (Figure 6.1d). Even at this high fluence, the large well-oriented graphite flakes of pristine flexible graphite are still preserved. The folding of the edges induced by the irradiation is supposed to be due to stress caused by the creation of vacancies and interstitials in the basal planes.

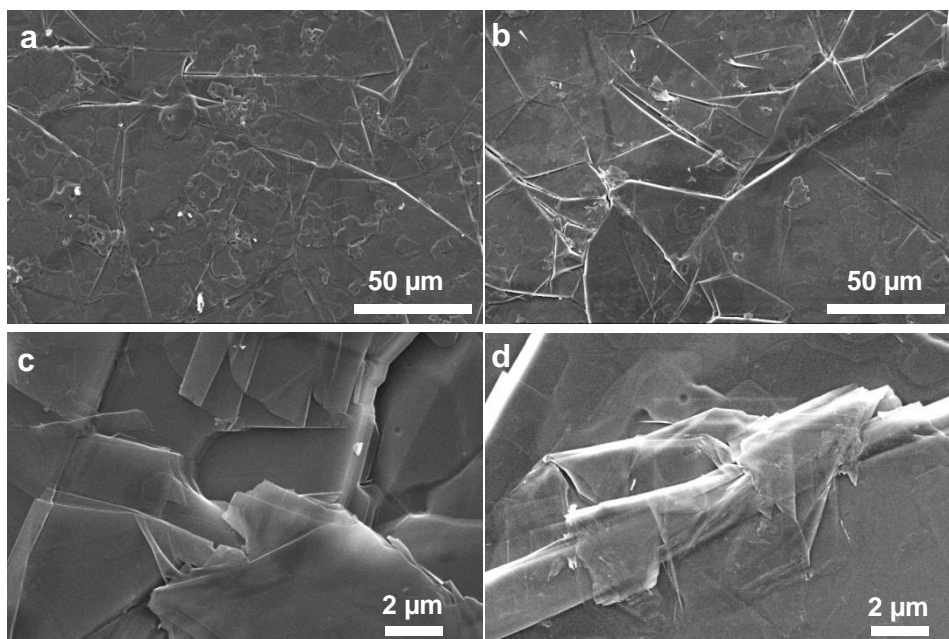


Figure 6.1 SEM images of flexible graphite before (a, c) and after (b, d) irradiation by 4.8 MeV/u Au ions at a fluence of  $1 \times 10^{13}$  ions/cm<sup>2</sup> at low and high magnification.



## 6.1.2 Raman spectroscopy

Raman spectroscopy analysis of thin ( $\sim 21 \mu\text{m}$ ) flexible graphite samples irradiated in stacks with Ca, Xe, Au and U ions allows probing of the beam-induced radiation damage at different position along the ion path corresponding to different energy loss values.

Selected Raman spectra, recorded at different depth and accumulated fluence, are presented in Figure 6.2 normalized to the intensity of the G-band. Comparing Raman spectra of 4.8 MeV/u Ca and Au ions irradiated flexible graphite, one can see a pronounced growth of the D-band intensity with increasing: 1) ion mass, 2) accumulated ion fluence, and 3) depth along the ion range.

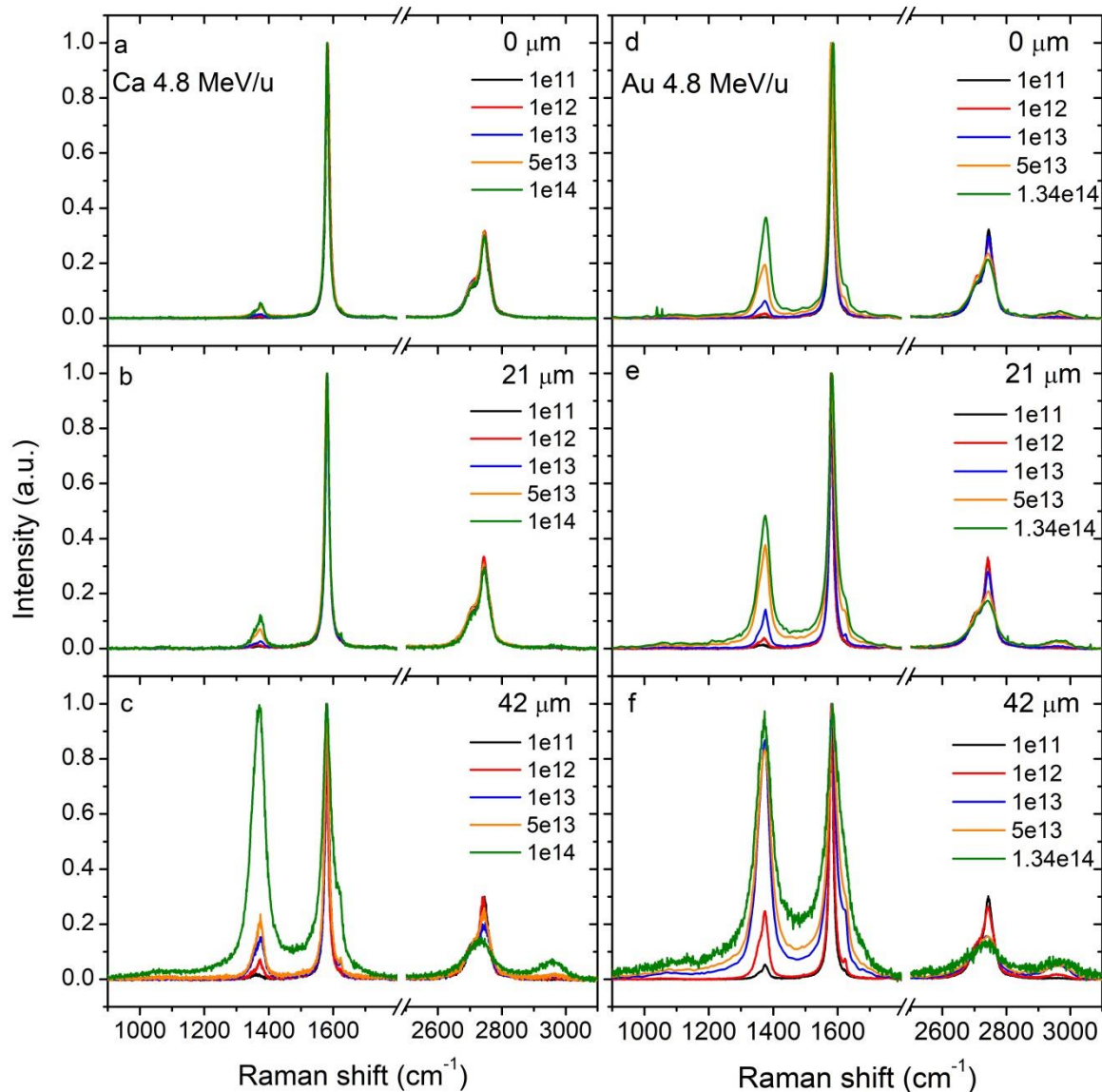


Figure 6.2 Raman spectra of flexible graphite irradiated with 4.8 MeV/u Ca (a, b, c) and Au (d, e, f) ions at fluences from  $1 \times 10^{11}$  to  $1.34 \times 10^{14}$  ions/cm<sup>2</sup>. The measurements correspond to a penetration depth of 0,  $21 \pm 1 \mu\text{m}$  and  $42 \pm 2 \mu\text{m}$  of the ion beam.

As mentioned in section 5.2, the D-band of the ion-beam irradiated flexible graphite is asymmetric and actually consists of two peaks D1 ( $\sim 1355 \text{ cm}^{-1}$ ) and D2 ( $\sim 1375 \text{ cm}^{-1}$ ) for laser wavelength  $\lambda$  of 473 nm. The splitting of the D-band, previously reported for the measurements of graphite edge-planes is caused by folded edges of graphite flakes, as observed with SEM. For further quantitative Raman analysis, the intensity of the D-band  $I_D$  is taken as a maximum of the added up D1 and D2 bands (see Figure 6.3), and the area  $A_D$  is the sum of the areas  $A_{D1}$  and  $A_{D2}$ . The intensity and area of the second order 2D-band are calculated in the same way.

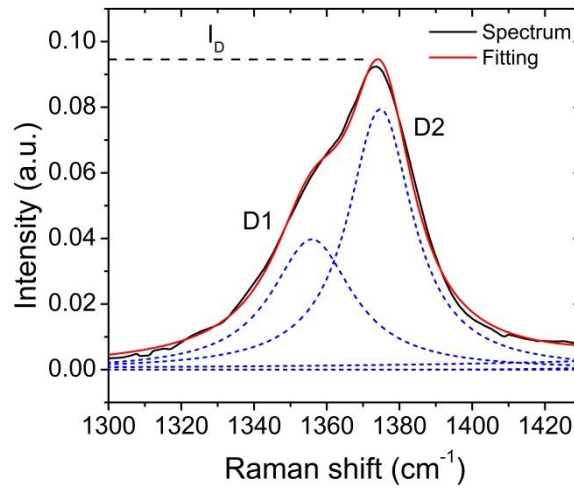


Figure 6.3 Raman D-band of ion irradiated flexible graphite consisting of D1 and D2 peaks.

The fluence dependence of the main Raman parameters is presented in Figure 6.4 for three series of flexible graphite samples irradiated with 4.8 MeV/u Ca, Xe and Au ions.  $I_D/I_G$ ,  $A_D/A_G$ , and FWHM(G) are usually considered for the characterization of structural disorder in graphite. All these Raman parameters show a consistent increase with fluence, evolving faster with the depth increasing from 0 to  $\sim 42 \mu\text{m}$  and with the ion mass increasing from Ca to Au. The  $I_D/I_G$  and  $A_D/A_G$  values follow the same trend and are more sensitive to the ion beam induced damage than FWHM(G), which shows an increase already at an intermediate fluence of  $1 \times 10^{12} \text{ ions/cm}^2$  and approaches saturation for the Au ion irradiation at a depth of  $\sim 42 \mu\text{m}$  and a fluence of  $1 \times 10^{14} \text{ ions/cm}^2$ . The Raman parameters of flexible graphite irradiated by Xe ions at the position of  $\sim 42 \mu\text{m}$  remain at the level of pristine values, indicating that the beam was stopped inside this sample. The relative intensity of the second order defect band  $I_{2D}/I_G$  demonstrates the inverse behavior, decreasing with accumulated beam induced damage. The  $I_D/I_G$  increases with ion fluence as  $I_D/I_G$ . The ratio  $I_D/I_D'$  is around 2 for pristine and low fluence samples irradiated with Ca and Xe ions, indicating grain boundaries as dominant defects [92,93]. For all used ion species, fluences and positions along the ion range,  $I_D/I_D'$

increases and stays around 6, what is typical to point-like defects. This is also the case for the Au-ion irradiated sample at low fluence ( $\sim 1 \times 10^{11}$  ions/cm<sup>2</sup>) at the end of the ion range.

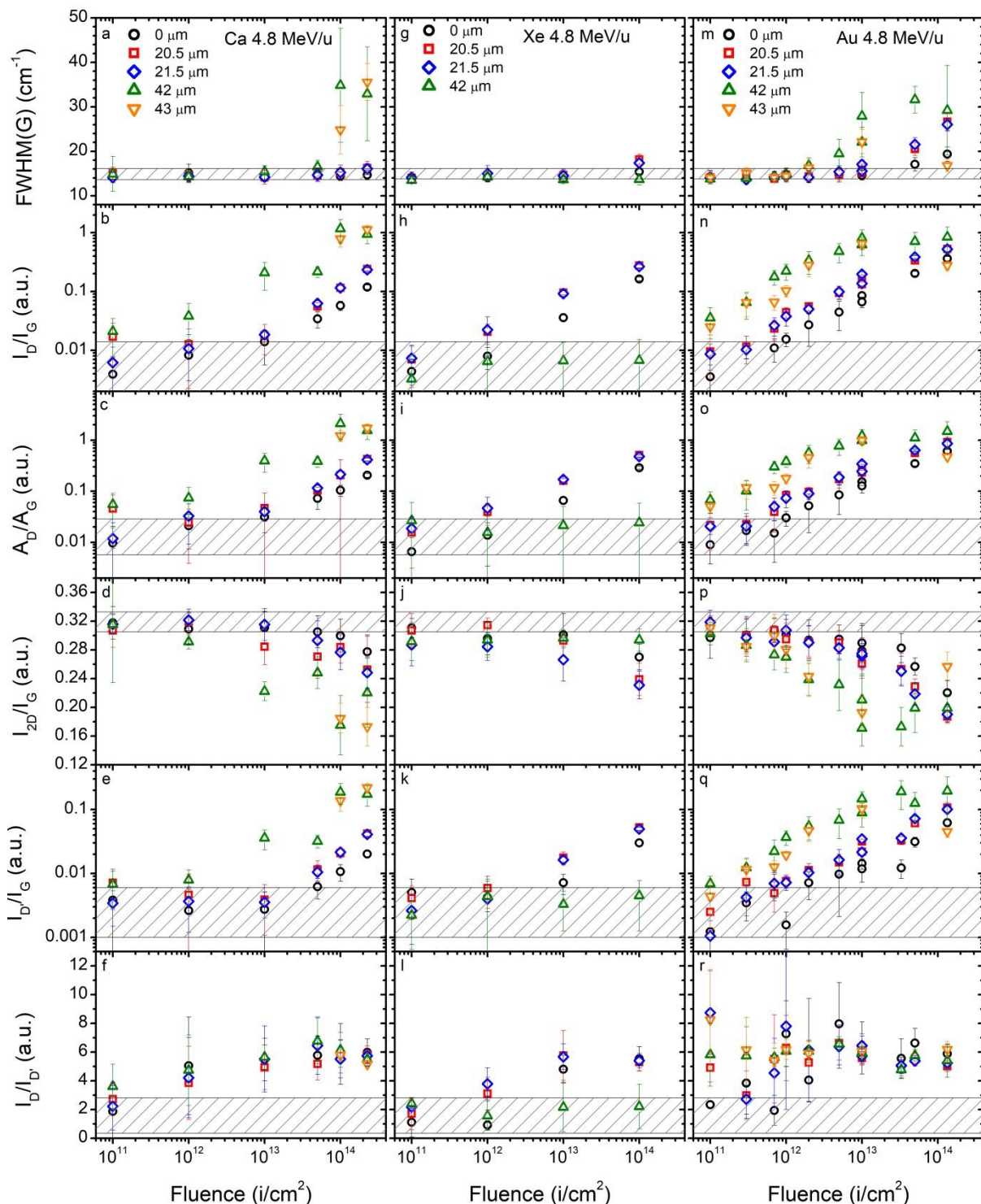


Figure 6.4 Evolution of Raman parameters FWHM(G),  $I_D/I_G$ ,  $A_D/A_G$ ,  $I_{2D}/I_G$ ,  $I_{D'}/I_G$ , and  $I_D/I_{D'}$  with increasing fluence for 4.8 MeV/u Ca, Xe and Au ion irradiated flexible graphite at different depths. Shaded areas denote average pristine values of the respective parameters.

The depth profiles of energy loss and Raman parameters for 4.8 MeV/u Ca, Xe, Au and U ion irradiated flexible graphite are presented in Figure 6.5. The electronic energy loss for all studied ion species is almost constant along the first  $\sim 30 \mu\text{m}$  of the ion range and steeply decreases in the last  $\sim 15 \mu\text{m}$ . The nuclear energy loss, on the contrary, increases monotonically along the whole ion range. The fact that the Raman parameters show an increase of structural disorder with increasing depth indicates that they are rather correlated to the nuclear energy loss dominated damage mechanism.

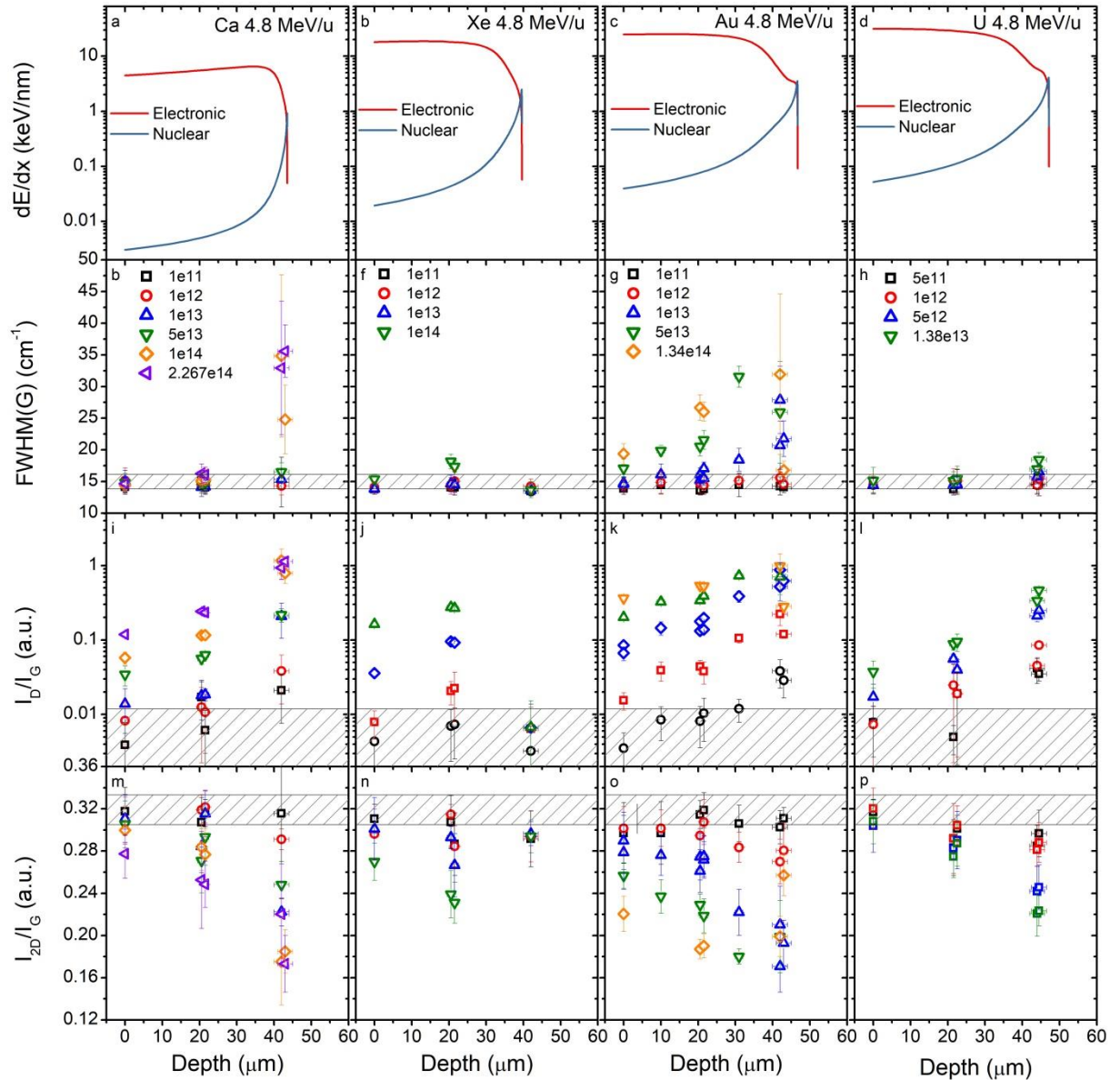


Figure 6.5 a-d) Electronic and nuclear energy loss of 4.8 MeV/u Ca, Xe, Au and U ions in flexible graphite, calculated using SRIM-2013. e-p) Raman parameters FWHM(G),  $I_D/I_G$ , and  $I_{2D}/I_G$  as a function of depth. The Raman spectra were recorded at the front and rear surfaces of three flexible graphite samples irradiated in stacks.



In order to compare results for different ion species and check the correlation between energy loss and induced damage, the accumulated dose  $D$  was calculated inserting just the nuclear or the electronic energy loss in equation 2.4. The obtained dose dependence for  $I_D/I_G$ , FWHM(G) and  $I_{2D}/I_G$  is presented in Figure 6.6. By comparing the behavior of the Raman parameters with increasing dose for different interaction regimes, one sees an obvious trend for all ion species in the case of nuclear dose dependence. At the same time the dependence of Raman parameters on electronic dose does not exhibit a smooth monotonous evolution. This scattering is caused by a higher damage at the end of the ion range, where the electronic energy loss steeply drops (see Figure 6.5). This leads us to the conclusion that in swift heavy ion irradiated flexible graphite the elastic interaction is the dominant mechanism of damage formation.

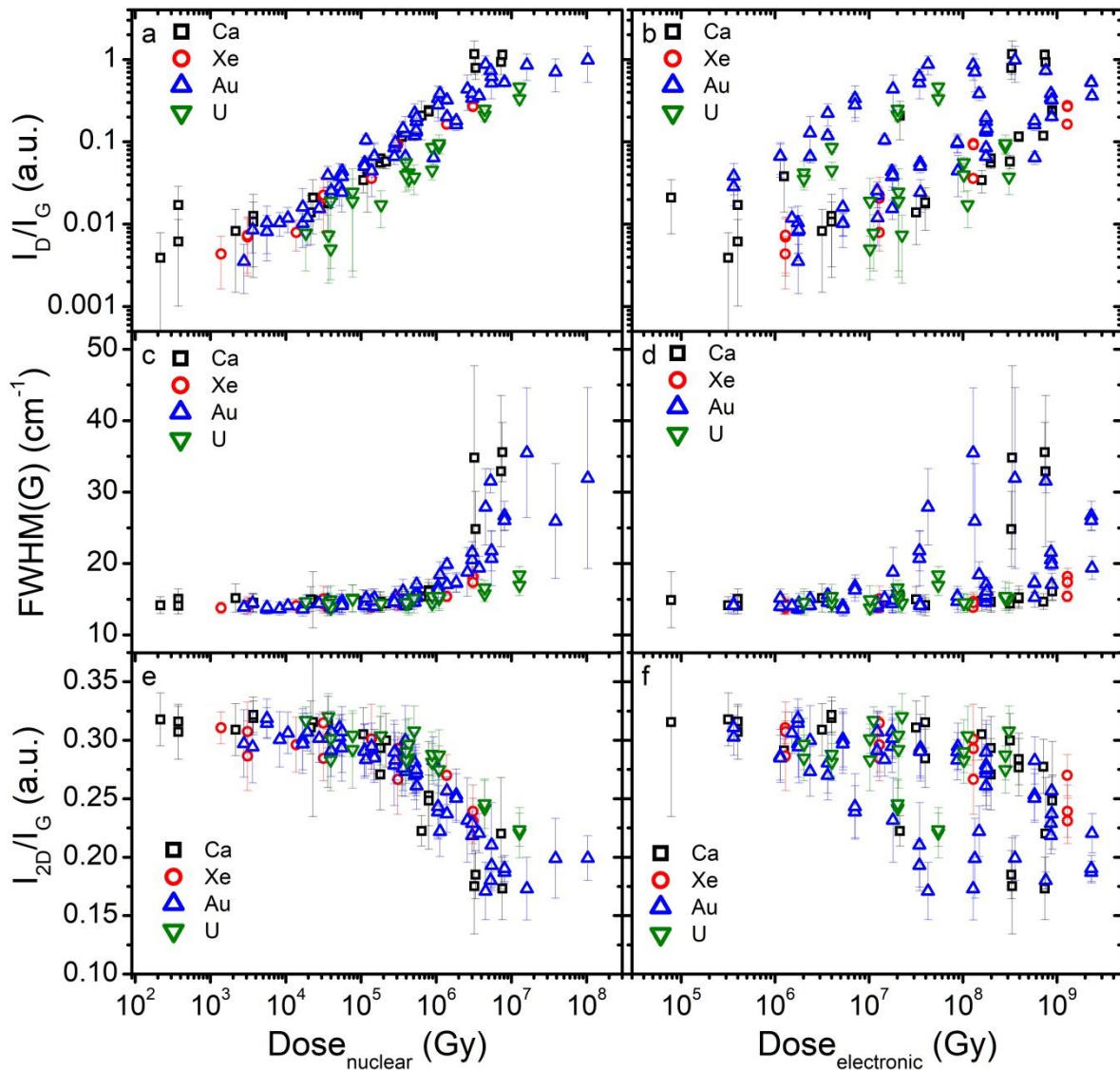


Figure 6.6 Raman parameters  $I_D/I_G$ , FWHM(G) and  $I_{2D}/I_G$  as a function of dose, calculated using nuclear (left) and electronic (right) energy loss of Ca, Xe, Au and U ions in flexible graphite.

As reported in previous works, 0D point defects and 1D ribbon like defects, that define the boundaries of crystallites, cause a rise of the D-band in graphite. In order to disentangle the contribution of each type of structural defects, we analyzed the evolution of FWHM(G). Because either the ratio  $I_D/I_G$  or  $A_D/A_G$  is used in literature, both parameters normalized by the excitation laser energy are shown in Figure 6.7 as a function of the corresponding FWHM(G). For all irradiated flexible graphite samples, the ratios  $I_D/I_G \propto E_L^4$  and  $A_D/A_G \propto E_L^4$  steeply increase at small initial broadening of the G-band. According to reference [91], this indicates the dominance of point defect creation, while the size of the in-plane crystallites stays relatively large.

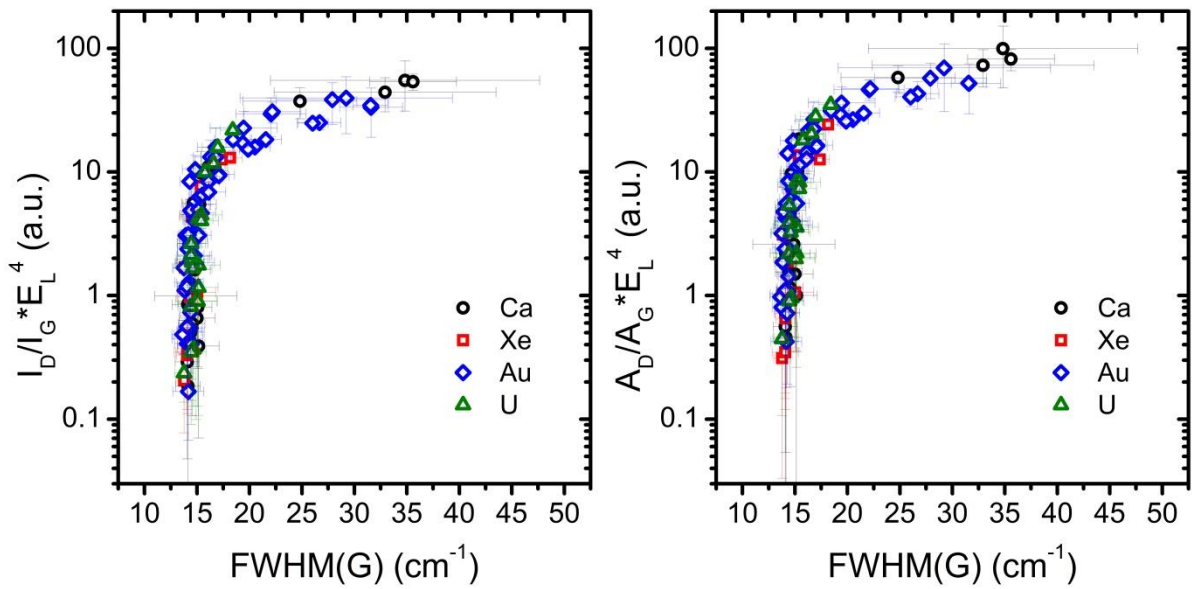


Figure 6.7 Raman parameters  $I_D/I_G$  and  $A_D/A_G$ , normalized by the laser excitation energy  $E_L$ , as a function of FWHM(G) for various ion irradiations.

The almost ideal crystallite structure of flexible graphite makes it more sensitive to the creation of point defects in the nuclear stopping regime. The initial low defect density and large size of the crystallites prevent fast recombination of beam induced defects.

---

## 6.2 Quasi-isotropic polycrystalline graphite

---

### 6.2.1 Scanning electron microscopy

---

Scanning electron microscopy (SEM) images show distinctive contrast features in the cross-section of the irradiated layer. Examples of low and high magnification SEM images of a sample irradiated with U ions at a fluence of  $5 \times 10^{13}$  ions/cm<sup>2</sup> are presented in Figure 6.8. The dashed line on the low magnification image (Figure 6.8a) corresponds to the SRIM calculated ion range. Compared to the non-irradiated substrate (below dashed line), the material of the ion modified layer (above dashed line) seems to have a more homogeneous structure and shows signs of brittle fracture.

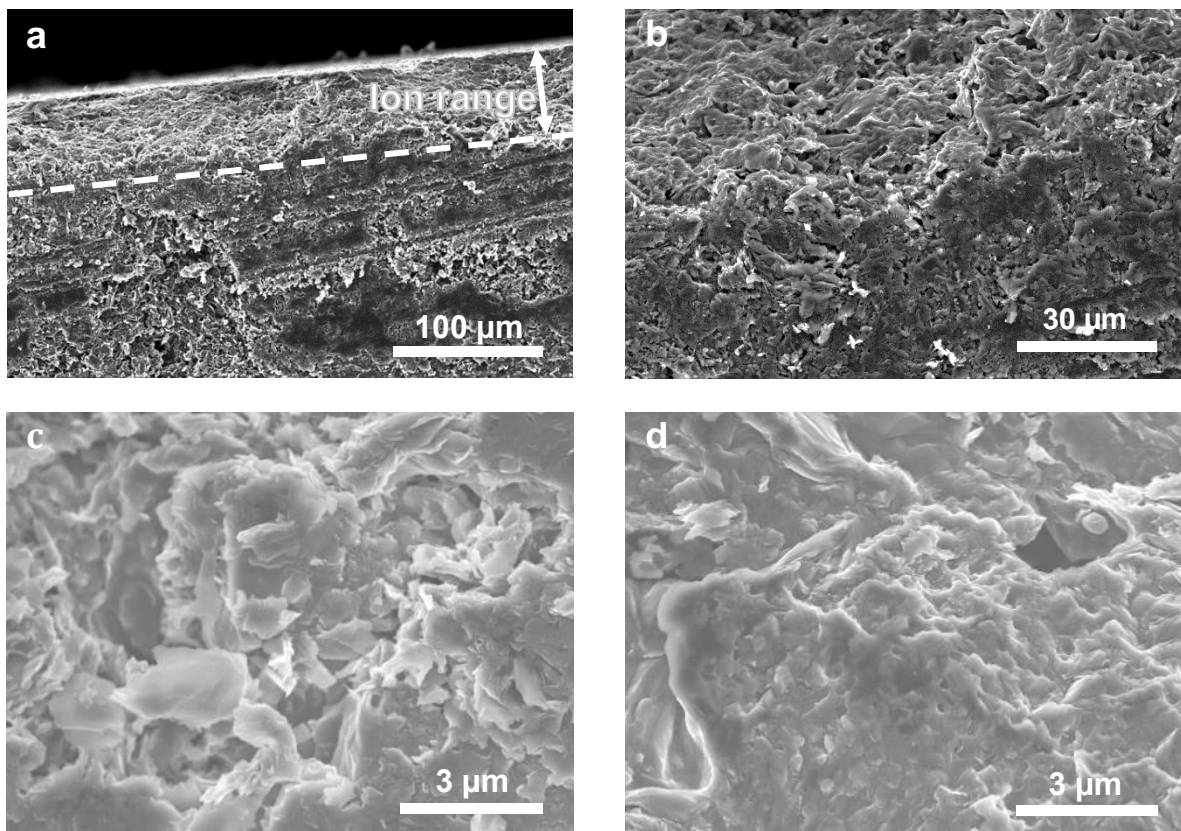


Figure 6.8 SEM images of polycrystalline graphite sample irradiated with 4.8 MeV/u U ions at a fluence of  $5 \times 10^{13}$  ions/cm<sup>2</sup>. a) and b) low magnification images of sample cross-section, the dashed line marks the SRIM calculated ion range (upper area: irradiated and lower area: pristine); c) high magnification image of non-irradiated section (beyond ion range); d) irradiated area of graphite sample within ion range.

The brighter features observed for this layer correspond to the complex topography of this fractured surface producing more secondary electrons in the SEM image. In the high-magnification SEM images (Figure 6.8c and d) the pristine graphite displays a polycrystalline structure with sharp grain boundaries whereas the irradiated graphite shows rounded grain

---

edges. Individual grains look like molten or amorphized indicating a possible allotropic phase change.

---

### 6.2.2 Raman spectroscopy

---

Raman spectroscopy measurements were performed on the surface of the irradiated sample and on cross-sections obtained by cutting or fracturing the irradiated samples. Cross-sections were analyzed by stepwise recording spectra from the sample surface across the irradiated region until deep into the non-irradiated substrate with a step width of  $2\ \mu\text{m}$ . This provided information on the structure of the irradiated layer and the pristine substrate and allowed us to check if the graphite exposed to swift heavy ions preserves the  $\text{sp}^2$  bonding. Examples of Raman spectroscopy depth profiles for samples irradiated with 4.8 MeV/u Ca, Au and U ions at a fluence of  $5 \times 10^{13}$  ions/cm<sup>2</sup> are shown in Figure 6.9. The spectra are background corrected and normalized to the intensity of the G-band (Raman shift  $1582\ \text{cm}^{-1}$ ). The position of the sample surface was identified based on the appearance of the G-band in the spectrum. The corresponding point was set as 0 depth for each line in the depth profile. Because of the finite laser beam spot size ( $\sim 4\ \mu\text{m}$ ) and the surface roughness of the fractured sample, the real sample edge is defined within an uncertainty of several  $\mu\text{m}$ .

Based on the D-band of the Raman spectra for all studied ion species, the ion range can be split in two parts depending on the dominant energy loss regime. Within the first  $\sim 40\ \mu\text{m}$  of the ion range, the inelastic interaction plays the important role, while the effect of elastic collisions becomes prominent in the last  $\sim 15\ \mu\text{m}$  before stopping of the ion. The recorded Raman depth profiles show a different response of polycrystalline graphite for light (Ca) and heavy (Au and U) ion irradiations. At the fluence of  $5 \times 10^{13}$  ions/cm<sup>2</sup> the region of dominant electronic energy loss looks just slightly damaged in the case of the Ca ion irradiation. At the same fluence, this part of the ion range of samples irradiated with Au and U ions exhibits significant changes, namely a rise and broadening of the D-band together with associated D3 ( $\sim 1500\ \text{cm}^{-1}$ ), D4 ( $\sim 1200\ \text{cm}^{-1}$ ) and D5 ( $\sim 1080\ \text{cm}^{-1}$ ) bands. The Raman spectra of graphite in the dominant nuclear energy loss part of the range look similar for all ions and is characterized by a large and sharp D-band. A comparison of the Raman spectra evolution from the regions with dominant electronic and nuclear energy loss for Ca, Au and U ions with increasing fluence can be found in Figure 6.10. The beam induced changes in the second order defect 2D band ( $\sim 2730\ \text{cm}^{-1}$ ) are also visible there. Caused by double phonon scattering mechanism, the 2D band becomes weaker with increasing defect density.



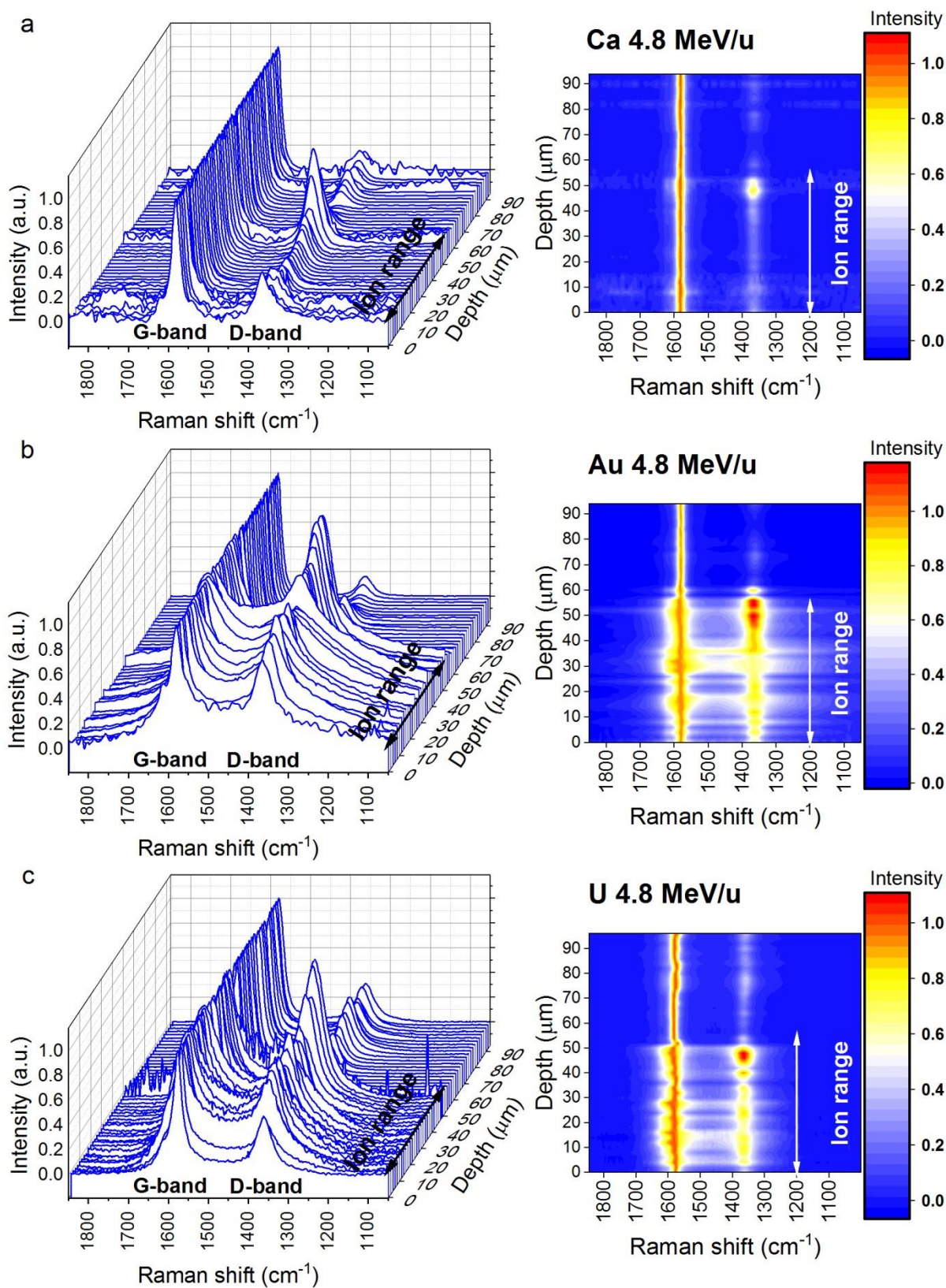


Figure 6.9 (Left) Stacked Raman spectra recorded on polycrystalline graphite sample cross-sections along the ion range for 4.8 MeV/u (a) Ca, (b) Au and (c) U ion irradiation at a fluence of  $5 \times 10^{13}$  ions/cm<sup>2</sup>; (Right) Corresponding intensity maps. All spectra are normalized to the intensity of the G-band.

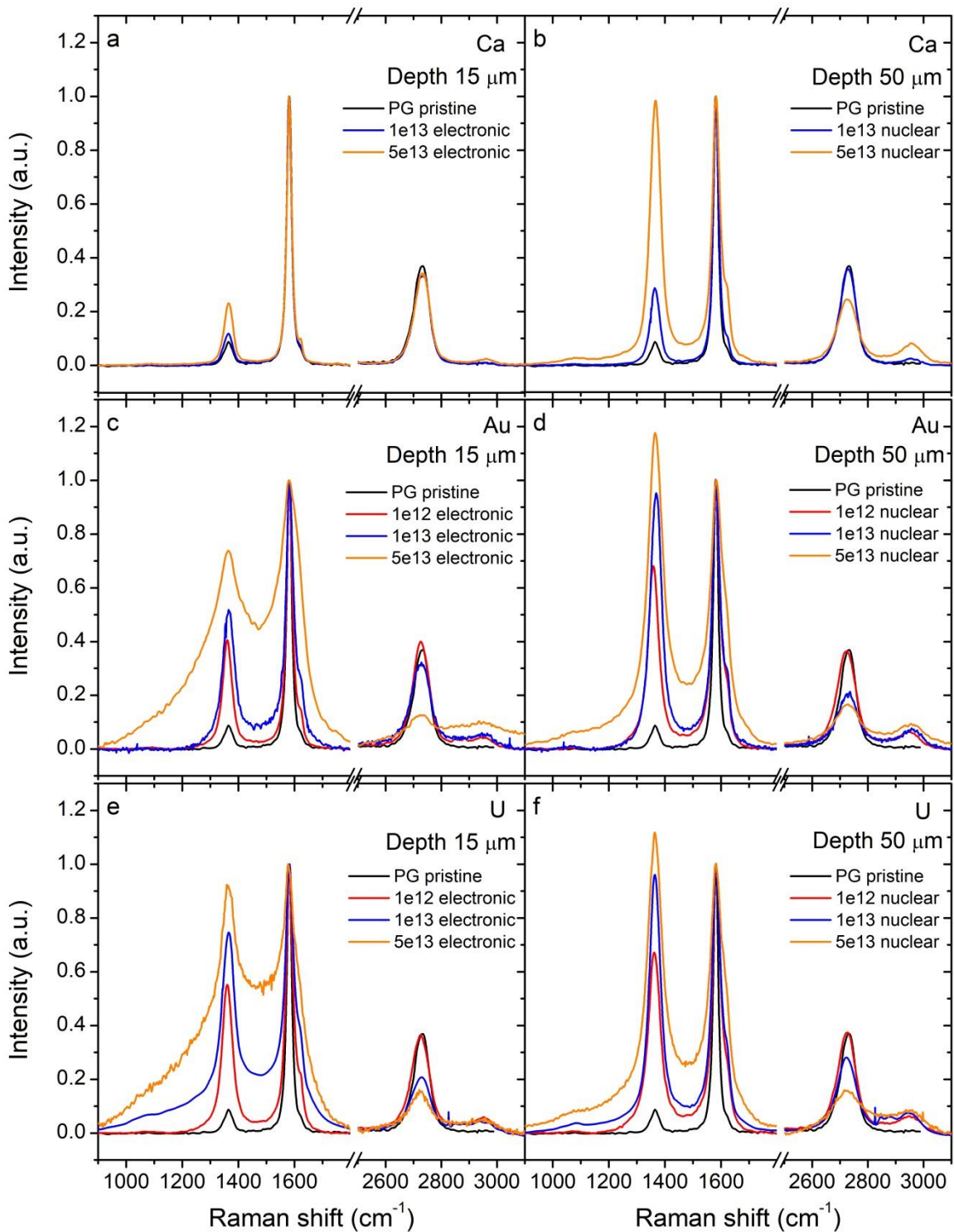


Figure 6.10 Raman spectra of pristine as well as 4.8 MeV/u Ca (a, b), Au (c, d) and U (e, f) ion irradiated polycrystalline graphite at different fluences, measured at the depth with dominant electronic ( $\sim 15 \mu\text{m}$ ) and nuclear ( $\sim 50 \mu\text{m}$ ) energy loss.

The Raman spectra of polycrystalline graphite are similar to flexible graphite, but there are minor variations. In polycrystalline graphite the D-band is symmetrical and does not show a splitting into the D1 and D2 peaks.

For fluences of  $1 \times 10^{12}$ ,  $1 \times 10^{13}$  and  $5 \times 10^{13}$  ions/cm<sup>2</sup>, the depth profiles of FWHM(G),  $I_D/I_G$ ,  $I_{D3}/I_G$  and  $I_{2D}/I_G$  parameters along with the calculated energy loss of 4.8 MeV/u Ca, Au and U ions are presented in Figure 6.11. The fluctuations along the profile are ascribed to the rather large grain size ( $\sim 7 \mu\text{m}$ ) of the sample being larger than the size of the laser spot ( $\sim 4 \mu\text{m}$ ) of the Raman spectrometer. For all measured samples, the profiles of the studied Raman parameters follow a similar scheme. For Au and U ions already at the fluence of  $1 \times 10^{12}$  ions/cm<sup>2</sup>, the values of FWHM(G),  $I_D/I_G$ ,  $I_{D3}/I_G$  are larger within the first  $\sim 55 \mu\text{m}$  from the irradiated surface than those for pristine graphite, measured within a depth from 60 to 90  $\mu\text{m}$ . Towards the end of the ion range, the values steeply drop to the average values of pristine polycrystalline graphite within less than 10  $\mu\text{m}$ . The  $I_{2D}/I_G$  ratio seems to follow the inverse dependence of FWHM(G). In the case of the Ca ion irradiation there are no observable changes in the Raman spectra up to the fluence of  $5 \times 10^{13}$  ions/cm<sup>2</sup>. The increased FWHM(G),  $I_D/I_G$ , and  $I_{D3}/I_G$  values and decreased  $I_{2D}/I_G$  ratio in the irradiated layer are a clear evidence for structural changes and disordering of the carbon lattice. The thickness of this beam-modified layer is in good agreement with the range of the ions as calculated by the SRIM-2013 code. For all studied ion species (Ca, Au and U ions), the values of the  $I_D/I_G$  ratio increase at a sample depth of approximately 50  $\mu\text{m}$  following the trend of the nuclear energy loss. This correlation indicates a dominant contribution of point defects due to the nuclear energy loss at the end of the ion range. In contrast, the values of FWHM(G) and  $I_{D3}/I_G$  are almost constant within the whole ion range, steeply decreasing close to the depth where the ions stop. This suggests a correlation to the electronic energy loss without excluding some contributions by the nuclear energy loss. Additionally, preserving of FWHM(G) and  $I_{D3}/I_G$  values on the pristine level for Ca ion irradiated graphite up to fluence of  $5 \times 10^{13}$  ions/cm<sup>2</sup> indicates a possible existence of an electronic energy loss threshold required for this specific material modification. The loss of crystalline order, corresponding to larger values of FWHM(G) and the formation of amorphous carbon ( $I_{D3}/I_G$ ) is significantly more pronounced at the highest fluence ( $5 \times 10^{13}$  ions/cm<sup>2</sup>) for Au and U ions. In spite of the high defect density and disordering, the corresponding Raman spectra still show the predominance of  $\text{sp}^2$  bonds, characteristic to graphite basal planes. In order to better distinguish the specific contributions of the electronic and nuclear energy loss, the studied Raman parameters were averaged along the first 40  $\mu\text{m}$  from the surface (electronic  $\text{dE}/\text{dx}$ ) and for the depth range from 40 to 56  $\mu\text{m}$  (nuclear  $\text{dE}/\text{dx}$ ). The mean values of the different Raman parameters for increasing fluence of Ca, Au and U ion irradiated polycrystalline graphite are presented in Figure 6.12.



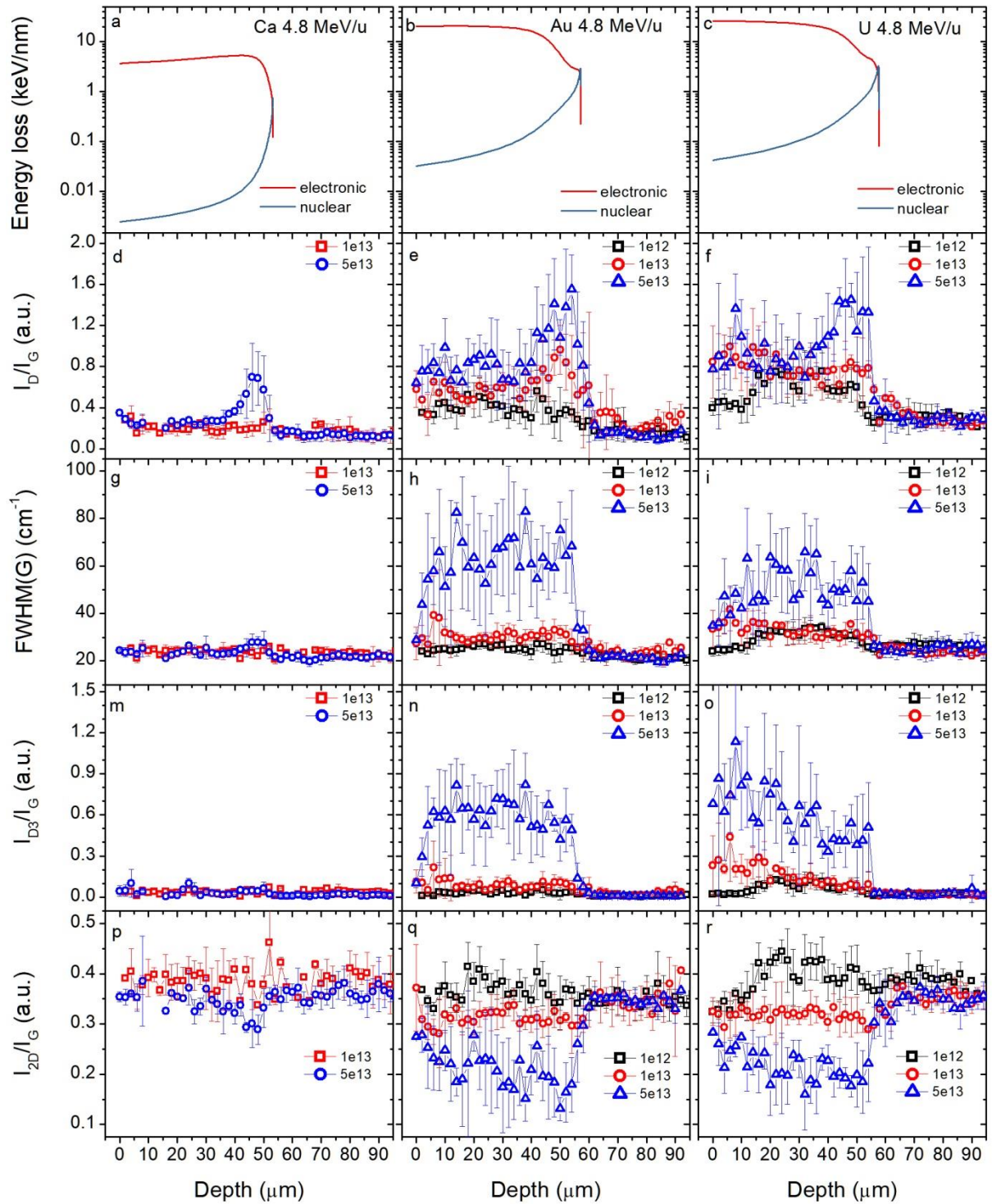


Figure 6.11 a, b, c – Electronic and nuclear energy loss of 4.8 MeV/u Ca, Au and U ions in polycrystalline graphite. The ratio of intensities  $I_D/I_G$  (d, e, f),  $I_{D3}/I_G$  (g, h, i), FWHM(G) (j, k, l) and  $I_{2D}/I_G$  (p, q, r) averaged over five line profiles measured on fractured cross-section of samples irradiated with 4.8 MeV/u Ca, Au and U ions at fluences of  $1 \times 10^{12}$ ,  $1 \times 10^{13}$  and  $5 \times 10^{13}$  ions/cm<sup>2</sup>.

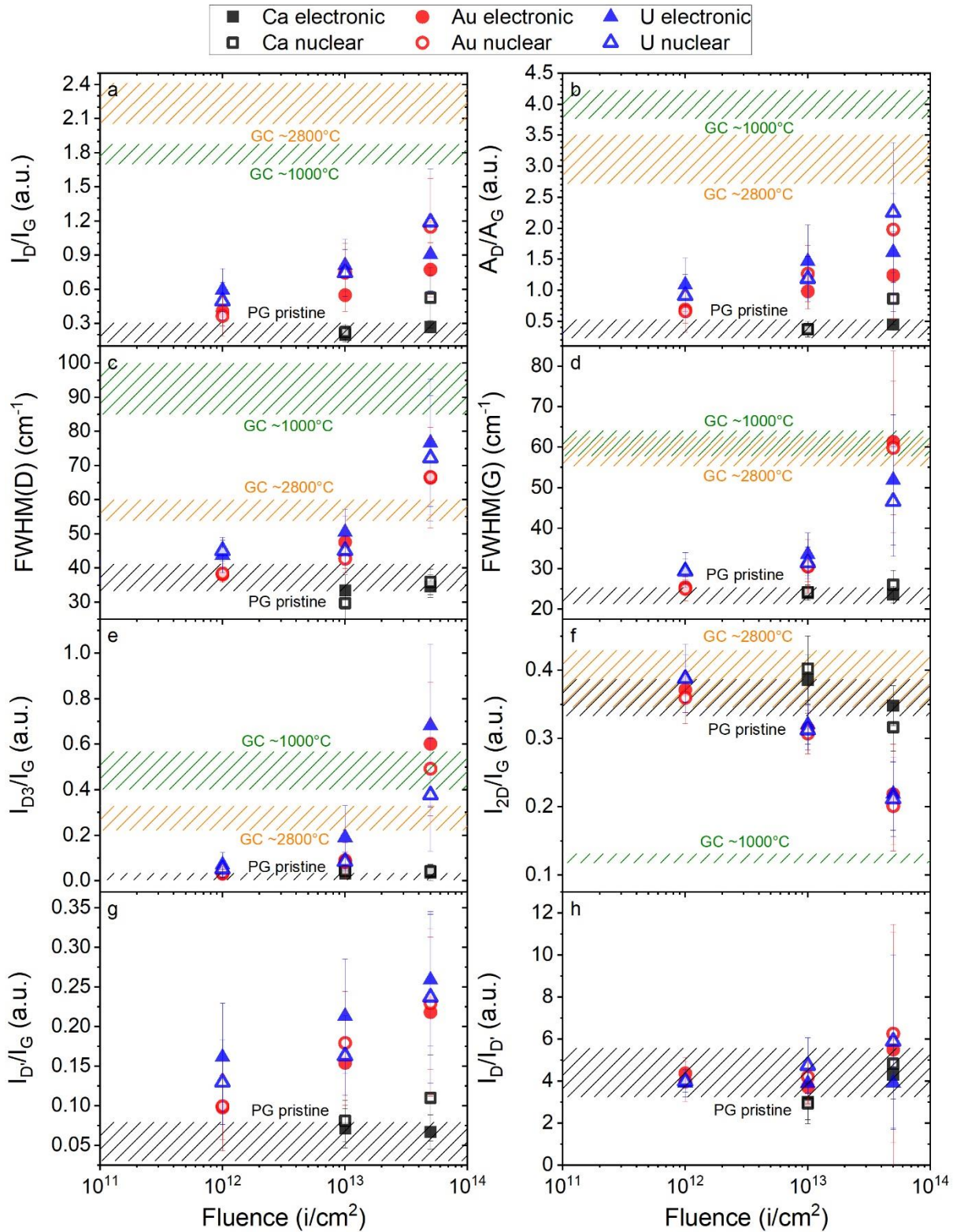


Figure 6.12 Evolution of the Raman parameters with increasing fluence of 4.8 MeV/u Ca, Au and U ion irradiated polycrystalline graphite. Full symbols are averaged values from 0 - 40  $\mu\text{m}$  sample depth dominated by electronic stopping and open symbols are averaged values from 40 - 56  $\mu\text{m}$  sample depth dominated by nuclear stopping. The average values of pristine polycrystalline graphite and two kinds of glassy carbon processed at different temperatures (discussed further in the text) are marked by shaded areas.

In general, the studied Raman parameters seem to follow an exponential dependence on the ion fluence, showing stronger effects of Au and U ion irradiations in comparison with Ca. The connected  $I_D/I_G$  and  $A_D/A_G$  parameters show higher values in the region dominated by nuclear energy loss in contrast to the  $I_{D3}/I_G$ , being higher in the region dominated by electronic energy loss. The other parameters do not demonstrate any significant difference between both energy loss regimes. The  $I_D/I_{D'}$  values stay around 4-5 for all samples studied, indicating that the nature of the structural disorder is related to point defects (Figure 6.12h).

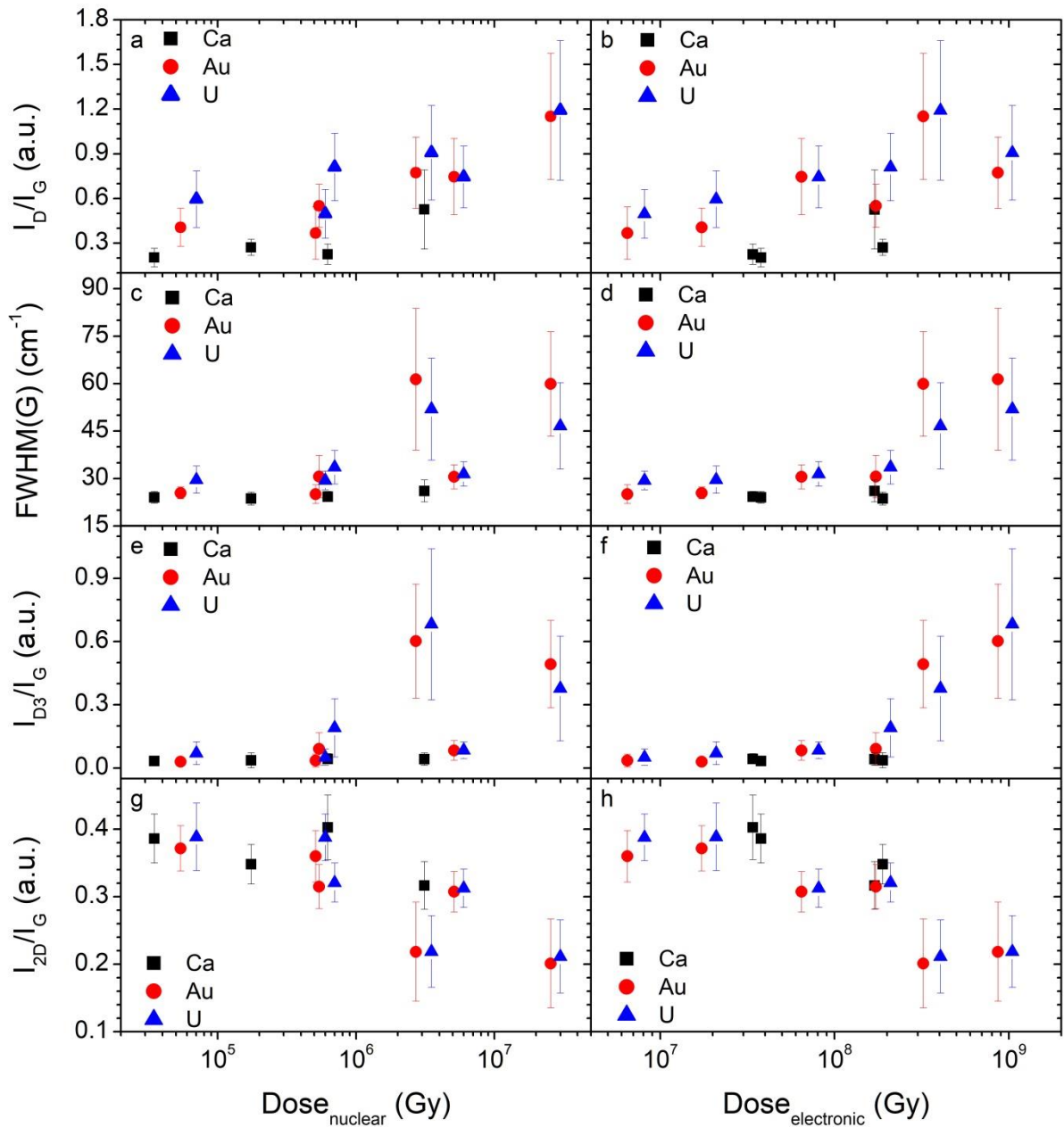


Figure 6.13 Dependence of  $I_D/I_G$ , FWHM(G),  $I_{D3}/I_G$  and  $I_{2D}/I_G$  on the calculated nuclear (left) and electronic (right) fraction of dose, induced by Ca, Au and U ion irradiation of polycrystalline graphite.



---

For a better comparison of the effects of the Ca, Au and U ion irradiation, the Raman parameters are presented as a function of nuclear and electronic dose in Figure 6.13. For the dose calculation, the average values of energy loss were obtained by integration the SRIM curves in the intervals from 0 to 40  $\mu\text{m}$  (electronic energy loss) and from 40 to 56  $\mu\text{m}$  (nuclear energy loss) divided by the respective length of the interval. Based on evolution of the Raman parameters with increasing dose, we tried to identify correlations with the nuclear and/or electronic energy loss. As in the case of flexible graphite, the  $I_D/I_G$  data of polycrystalline graphite irradiated with Au and U ions monotonically increases with nuclear dose (Fig. 6.13a). Thus the damage accumulation seems to be connected to the nuclear energy loss, possibly with some contribution of the electronic energy loss (Fig. 6.13b). The effect is less obvious for Ca ions. An interpretation of the other Raman parameters is more difficult because of large scattering of the data and somehow similar trends for the nuclear and electronic dose dependence. The FWHM(G) and  $I_{D3}/I_G$  data for the irradiation with Au and U ions seem to increase above an electronic dose of about 0.2 GGy corresponding to a fluence regime of  $1 \times 10^{13}$  -  $5 \times 10^{13}$  ions/cm<sup>2</sup>. We interpret this as a possible indication for an electronic energy loss threshold.

The analysis of the Raman spectra of the graphite samples irradiated at the highest fluence of  $5 \times 10^{13}$  ions/cm<sup>2</sup> with Au and U ions (see Figure 6.10) indicates a beam-induced transition from fine grained polycrystalline graphite to a damaged structure similar to glassy carbon (see Figure 6.14). This conclusion is supported by the observation of the increased intensity of the D-bands in the region from 1000 to 1500  $\text{cm}^{-1}$ , which are similar to the Raman spectra of Sigradur K and Sigradur G glassy carbon grades produced at 1000°C and 2800°C, respectively (see section 2.1.2.3). The Raman spectra of these glassy carbon grades are in agreement with a previous study on the structural evolution of glassy carbon with temperature (Figure 6.14) [41]. The Raman parameters for glassy carbon with the indicated process temperatures are included in Figure 6.12 as shaded area. For the irradiated graphite samples, the shift and broadening of the G-band leads to a strong overlap with the D' peak, which makes the deconvolution of the later less consistent. The  $I_D/I_G$ , FWHM(D),  $I_{D3}/I_G$  and  $I_{2D}/I_G$  parameters seem to be more sensitive and allow a more reliable assignment to the different temperature grades of glassy carbon. Based on the evolution of these parameters, we conclude that polycrystalline graphite irradiated with the Au and U at high fluence becomes quite similar to the typical low-temperature (below 1000°C) glassy carbon characterized by smaller, disordered sp<sup>2</sup> building blocks.

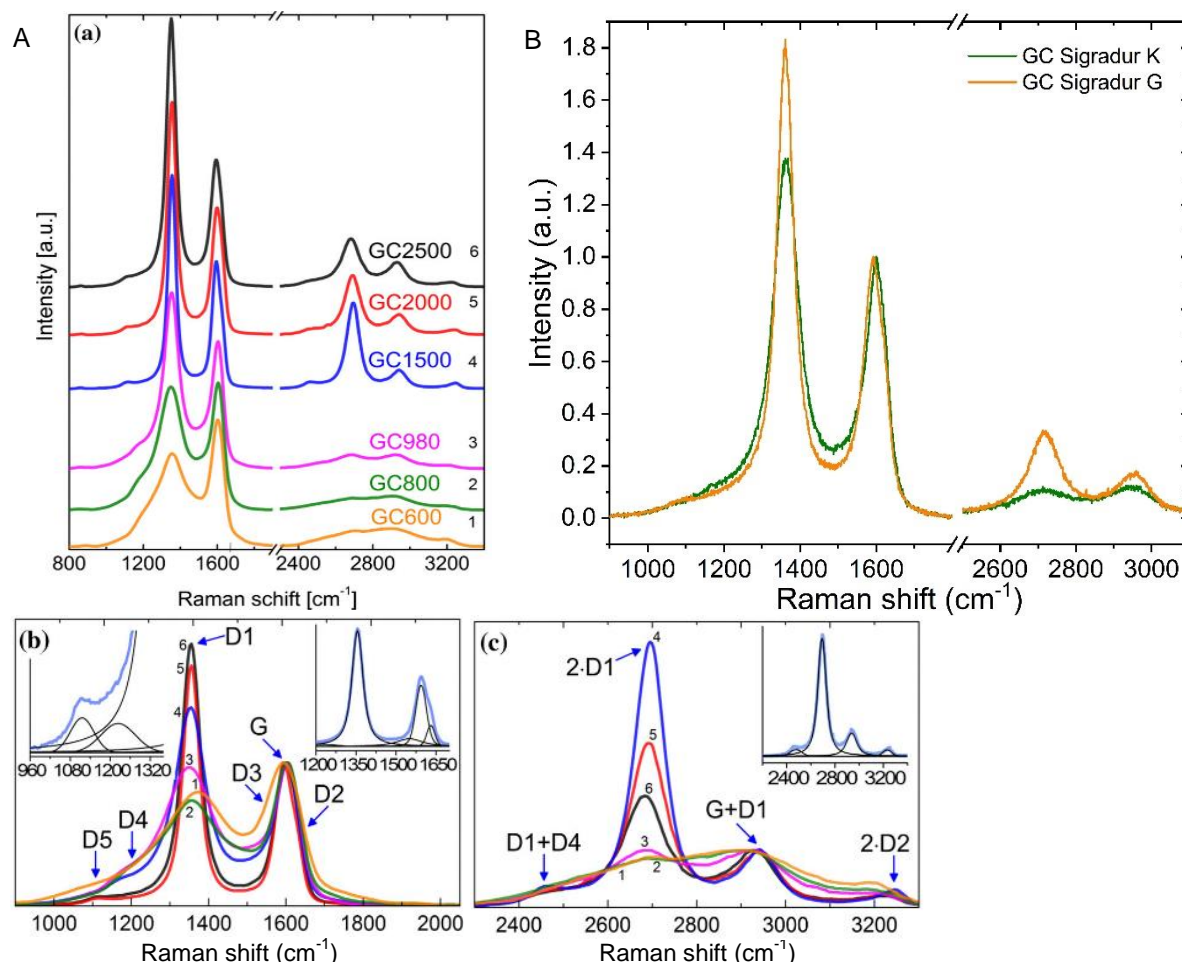


Figure 6.14 A – (a) Raman spectra of glassy carbon, processed at different temperatures from 600°C to 2500°C, adapted from [41]. Comparison of the spectra for the first order (b) and the second order (c) wavenumber regions of the different D bands. B – Raman spectra of the Sigradur K and Sigradur G glassy carbon grades.

Beam induced structural changes and defect formation in graphite can be followed by the evolution of stress in the irradiated area and at the interface between damaged and pristine material. We tested the shift of the position of the G-band as an indication of such stresses. The shift towards lower or higher wavenumbers is usually assigned to tensile or compressive stresses, respectively. Positions of the Raman G-band averaged over several profiles for Ca, Au and U ion irradiated polycrystalline graphite along the ion range are presented in Figure 6.15. Similar to the results mentioned above, the irradiation with Ca ions does not lead to stress formation up to a fluence of  $5 \times 10^{13}$  ions/cm<sup>2</sup>. In the case of the irradiation with Au ions at the fluence of  $1 \times 10^{13}$  ions/cm<sup>2</sup>, tensile stress seems to appear mostly in the irradiated region of the sample. The stress changes to compressive stress in the irradiated range for fluences up to  $5 \times 10^{13}$  ions/cm<sup>2</sup>. For the sample irradiated with U ions, such effects are less pronounced. The analysis of the precise position of the G-band of the high fluence samples is difficult



because of the large spectral background. Thus a conclusive interpretation of the stress evolution is not possible due to the large uncertainties.

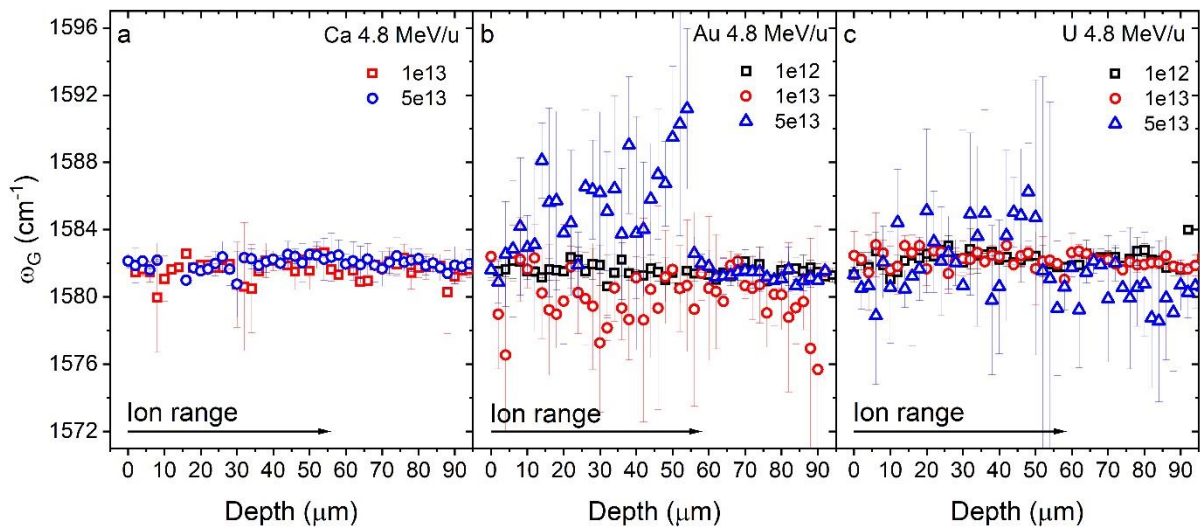


Figure 6.15 G-band position of Ca, Au and U ion irradiated polycrystalline graphite measured along the ion range at fluence of  $1 \times 10^{12}$ ,  $1 \times 10^{13}$  and  $5 \times 10^{13}$  ions/ $\text{cm}^2$ . The arrow indicates the interface between the irradiated and non-irradiated zone.

### 6.3 Discussion and summary

Swift heavy ion irradiation leads to the creation of structural damage in flexible and polycrystalline graphite. As discussed in Section 5.2, based on the two independent Raman parameters,  $A_D/A_G$  and  $\text{FWHM}(G)$ , it is possible to distinguish between the contribution of 0D point defects and 1D disordered crystalline boundaries. The values of these parameters, corresponding to swift heavy ion irradiated flexible and polycrystalline graphite, are presented in Figure 6.16. According to Ref. [91], the radiation damage in irradiated flexible graphite is mainly ascribed to point defects because the  $\text{FWHM}(G)$  values remain below  $20 \text{ cm}^{-1}$  with increasing  $A_D/A_G$ . At higher fluences/doses, the  $\text{FWHM}(G)$  values become larger with increasing  $A_D/A_G$  indicating a decrease of the in-plane crystallite size. In the case of polycrystalline graphite, both point defects and crystallite boundaries already exist in pristine material and swift heavy ion irradiation causes the simultaneous increase of the defect density and a decrease of the in-plane crystallite size.

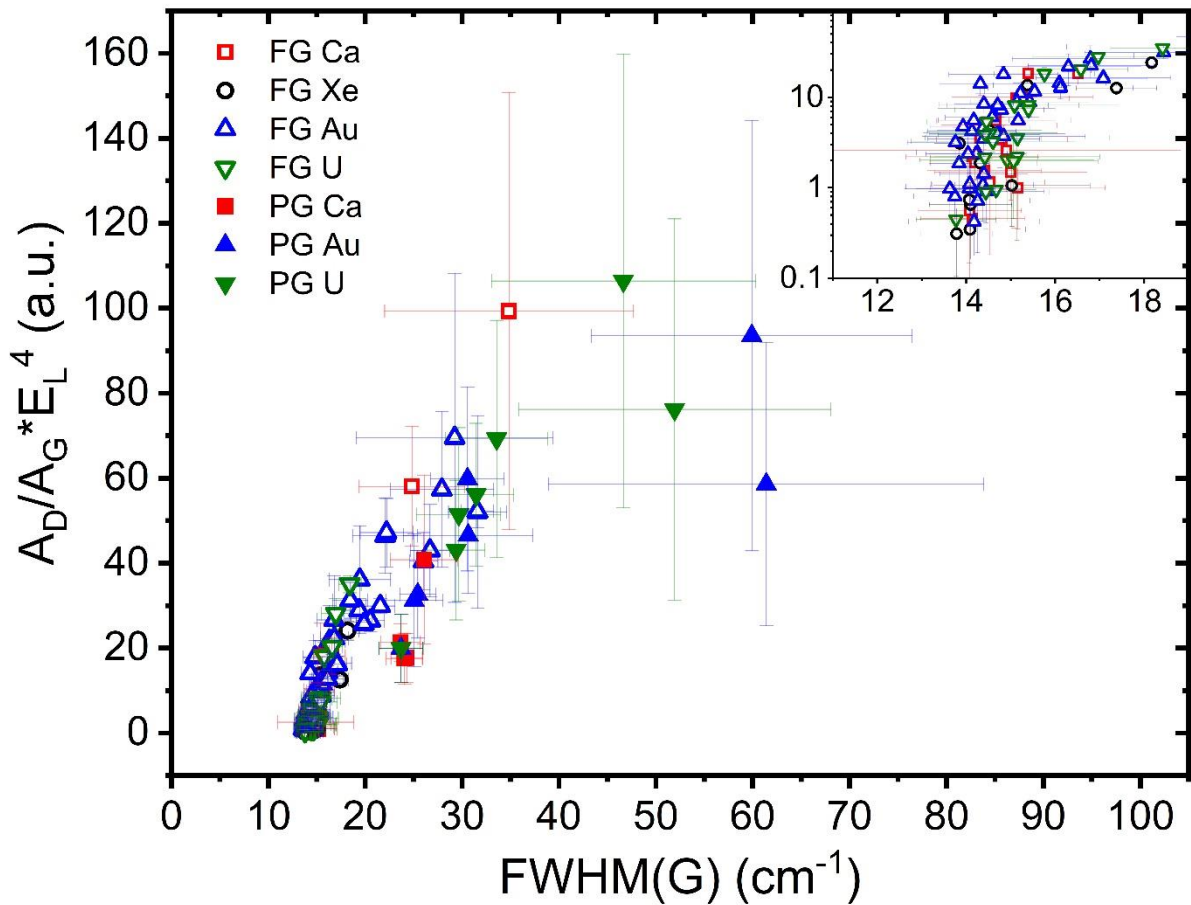


Figure 6.16  $A_D/A_G$  normalized by the laser excitation energy as a function of  $\text{FWHM}(G)$  for ion irradiated flexible and polycrystalline graphite

---

The results obtained for the Raman spectroscopy parameters clearly show a different response of flexible graphite (almost ideal, highly anisotropic structure) and polycrystalline graphite (quasi-isotropic fine grained with initially large amount of defects and grain boundaries). The damage evolution in flexible graphite is weak or not correlated with the electronic energy loss up to the maximum tested values of 30 keV/nm. In the case of polycrystalline graphite, the contribution of the nuclear energy loss remains prominent especially at the end of the ion range where the nuclear energy loss is maximal. However, in contrast to flexible graphite, polycrystalline graphite shows a higher sensitivity to the electronic energy loss in the case of Au and U ion irradiations corresponding to 20 and 25 keV/nm, respectively. As this effect is not observed for the Ca ion irradiation (electronic energy loss of 4 keV/nm), the threshold of the electronic energy loss is expected to be between 4 and 20 keV/nm. Above this value, the structural changes in polycrystalline graphite are no longer just related to point defects. This effect can be connected to the initial structural difference between flexible and polycrystalline graphite. Polycrystalline graphite is formed of randomly oriented small grains, consisting of multiple crystallites of well-structured graphite. On the scale of single crystallites, this material has the structure of ideal HOPG, but due to the random orientation, the properties are quasi-isotropic. In contrast, flexible graphite consists of HOPG-like parallel oriented flakes, which lead to a very high conductivity in the basal plane and an efficient dissipation of the energy, deposited in the electronic subsystem. This attenuates electronic energy loss induced structural changes in the lattice of flexible graphite. Due to the fine and defective crystallite structure of polycrystalline graphite, its conductivity is limited causing confinement of the deposited ion energy and consequent structural transformation. At the same time, although the nuclear energy loss is much smaller, elastic scattering processes and resulting formation of point defects are very efficient.

The observed structural changes of swift heavy ion irradiated graphite show a similar trend to the previously studied evolution of highly oriented pyrolytic graphite (HOPG) exposed to low [76,84] and high [14,16] energy ions, as well as to low energy ion irradiated polycrystalline graphite [127] and glassy carbon [128]. All this data supports the idea of a high sensitivity of  $sp^2$  based carbon structure to radiation damage dominated by nuclear energy loss. The elastic collisions and the resulting damage cascades lead to the development of dislocations, fragmentation and misorientation of carbon crystallites, reaching finally a highly disordered turbostratic structure and complete amorphization at a very high fluence (e.g. the 250 keV Cl ion irradiation at a fluence of  $1 \times 10^{16}$  ions/cm<sup>2</sup>) as supported by HRTEM analysis [127].

---

Regarding the effect of electronic energy loss on damage creation in graphite, there exist only very few studies [14,16]. For a direct comparison with earlier results, the different experimental conditions have to be taken into account. When comparing Raman results, we considered that the intensity of the D-band has to be normalized by the energy  $E_L$  of the excitation laser [85], and find a similar behavior as reported in [14,16].

SEM and Raman spectroscopy demonstrate bending and folding of basal plane in flexible graphite due to ion irradiation. This can be linked to the formation of faulty  $sp^2$  structures and non-6-membered carbon rings in the basal planes as shown in MD simulations [29]. Such defects induce fragmentation, bending, and interconnections of basal planes, but the predominant  $sp^2$  structure is retained. Under extensive irradiation, fine grain polycrystalline graphite evolves towards a structure that is similar to glassy carbon.

Flexible and polycrystalline graphite show pronounced defect formation that we mainly ascribe to nuclear energy loss. The influence of electronic energy loss varies, depending on the structure of graphite and energy loss values. There are evidences of the enhancement of damage formation in polycrystalline graphite with combined contributions of nuclear and electronic energy loss. The data available to date are not conclusive enough to discuss synergistic effects of the electronic and nuclear energy loss as previously reported for oxides [129–133].

---

## 7 Thermophysical modifications caused by ion irradiation

---

This chapter is focused on the changes of the thermophysical properties of ion beam irradiated well-oriented flexible graphite and fine grained quasi-isotropic polycrystalline graphite. As the main heat carriers in graphite are phonons, one can expect that the structural modifications caused by the ion beam may lead to the degradation of the thermal conductivity and thermal diffusivity.

---

### 7.1 Well-oriented graphite

---

Based on the structure, well-oriented flexible graphite has highly anisotropic properties. The thermal conductivity of flexible graphite in basal planes is two orders of magnitude larger in comparison with the thermal conductivity in normal direction.

---

#### 7.1.1 In-plane laser flash analysis

---

In-plane laser flash analysis gives average thermal diffusivity value of the irradiated flexible graphite samples and does not take into account non-homogeneous structural changes along the ion range.

Examples of the LFA signals, which represent the temperature response of a sample after applying the laser pulse, measured on the front (0-21  $\mu\text{m}$ ) and middle (21-42  $\mu\text{m}$ ) flexible graphite sample of a stack irradiated with Ca and Au ions, are shown in Figure 7.1 (the time scale for the Ca and Au ion irradiated samples is different). In most of the cases, the ion beam stopped at the end of the second sample or beginning of the third one. Thus, measurements of the thermal diffusivity of the last sample in a stack are not presented here. The response time of samples from the front of the stack (0-21  $\mu\text{m}$ ) is not significantly (Ca ions) or only slightly (Au ions) influenced by the ion fluence. For the middle samples irradiated with Ca or Au ions, the response time becomes longer with increasing fluence, indicating a stronger effect of the radiation damage on the heat propagation inside the samples.

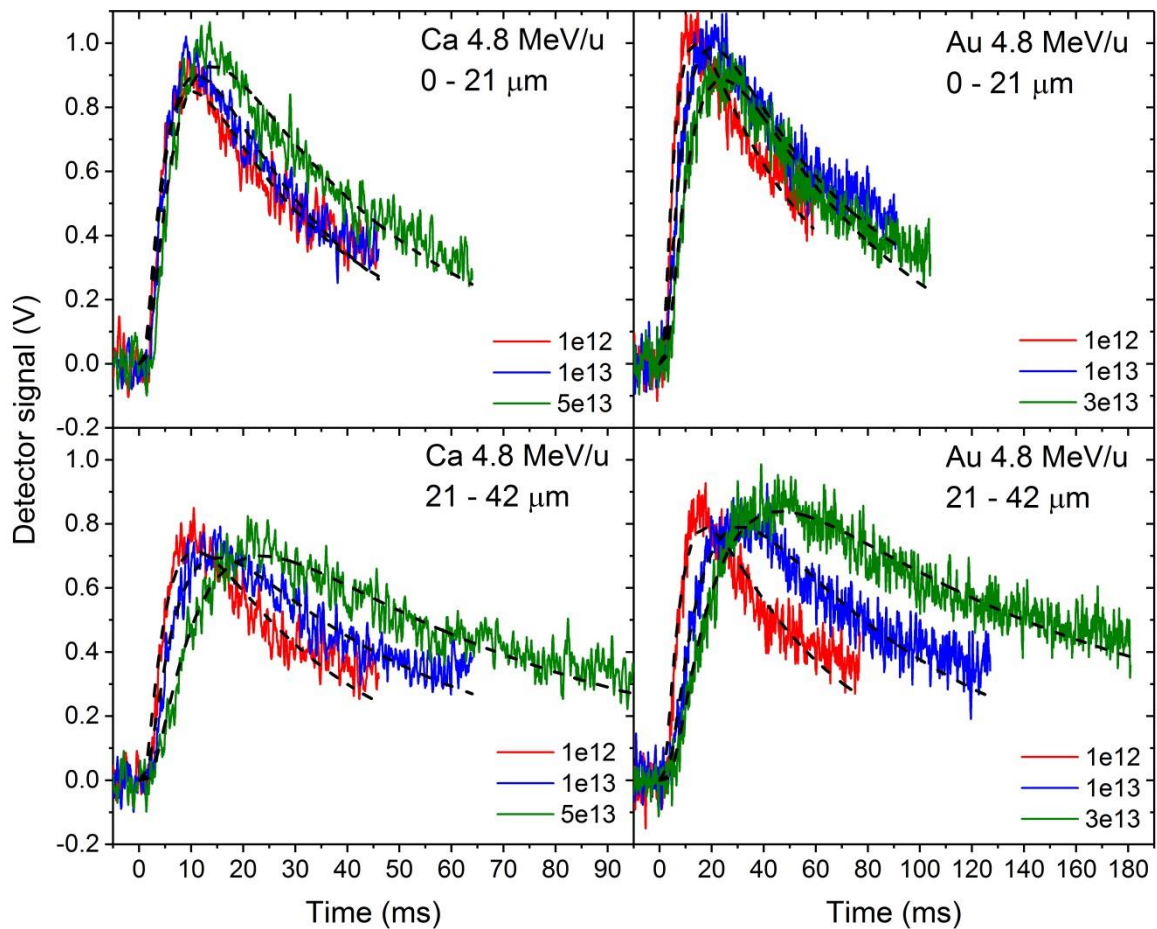


Figure 7.1 LFA detector signals of flexible graphite from a sample stack irradiated with 4.8 MeV/u Ca (left) and Au (right) ions of various fluences: 0-21  $\mu\text{m}$  represents the front sample and 21-42  $\mu\text{m}$  represents the middle sample. For both samples the entire volume is irradiated.

For flexible graphite, absolute and relative values of the in-plane thermal diffusivity as deduced from the LFA signals are presented in Figure 7.2. The in-plane thermal diffusivity is very sensitive to the beam induced radiation damage. The degradation appears faster and reaches lower values of the thermal diffusivity the heavier the ions ( $\text{Au} > \text{Xe} > \text{Ca}$ ). In agreement with the increase of the damage along the ion range revealed by Raman spectroscopy, the LFA measurements also demonstrate a higher degradation of thermal diffusivity for the second sample in the stack. This provides an indication of a dominant contribution of point defects produced via elastic collisions in the beam induced disordering in flexible graphite.

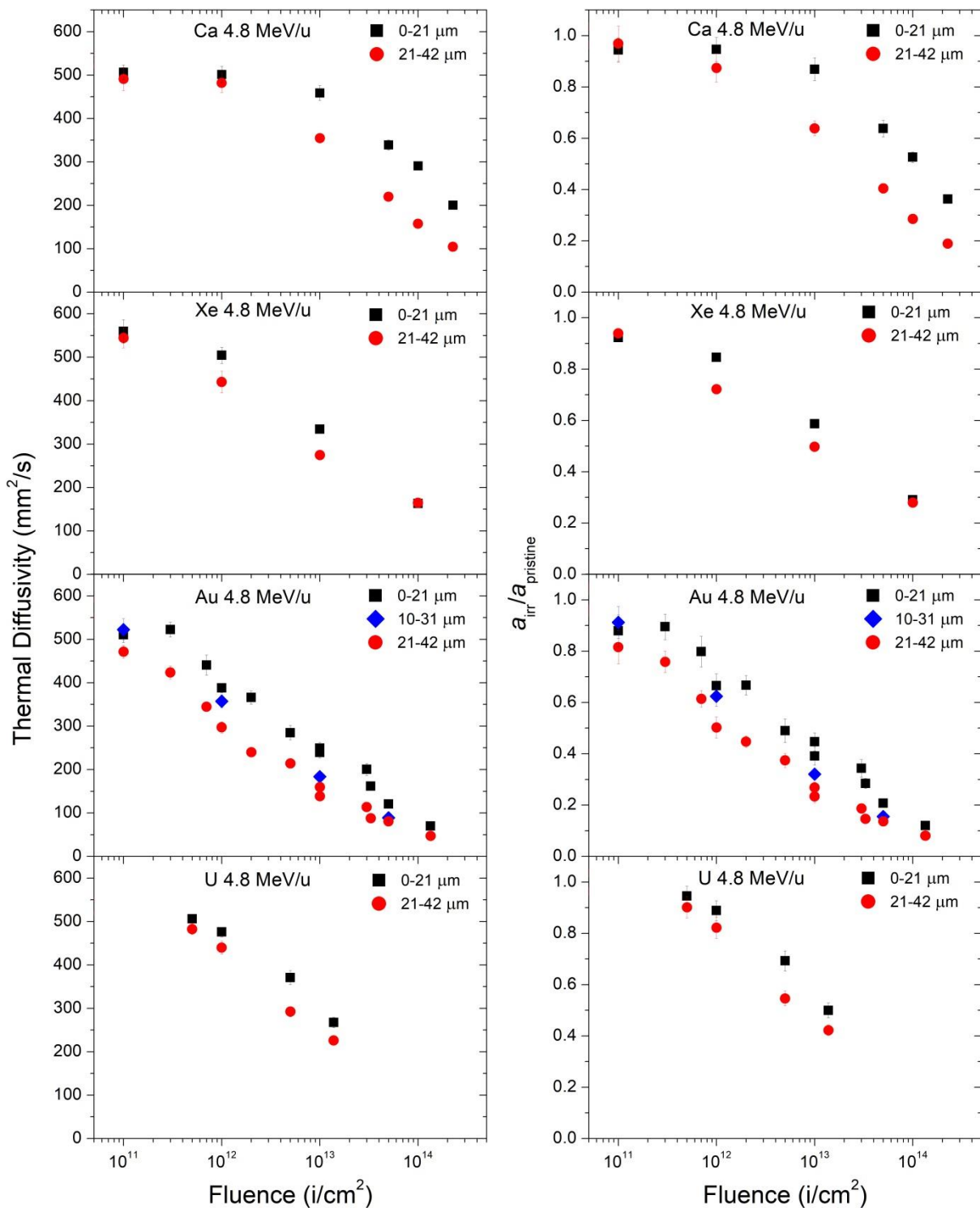


Figure 7.2 Absolute (left) and relative (right) in-plane thermal diffusivity as a function of fluence of 4.8 MeV/u Ca, Xe, Au and U ion irradiated flexible graphite.

A comparison of the thermal diffusivity degradation, induced by the different ion species in both the front and middle samples of the irradiated stacks, is shown in Figure 7.3 as a function of the deposited electronic and nuclear dose. Similar to the dose dependence of the



Raman parameters, the degradation of the thermal diffusivity seems to follow the nuclear dose (especially for Ca, Au and only partly for Xe ions), while the data scatter much more in the case of the electronic dose dependence. We assume that the deviation of some of the Xe data has to be ascribed to the fact that the Xe ions did not completely penetrate through the middle samples and the deduced thermal diffusivity thus includes a small contribution of the pristine material. In the case of U ions, the degradation of the thermal diffusivity shows the same trend but is shifted towards higher dose values. This effect was also observed for the dose evolution of the Raman parameters and is probably assigned to the different beam structure (short pulses with a high intensity) or to a systematic overestimation of the fluence of the U ion irradiation.

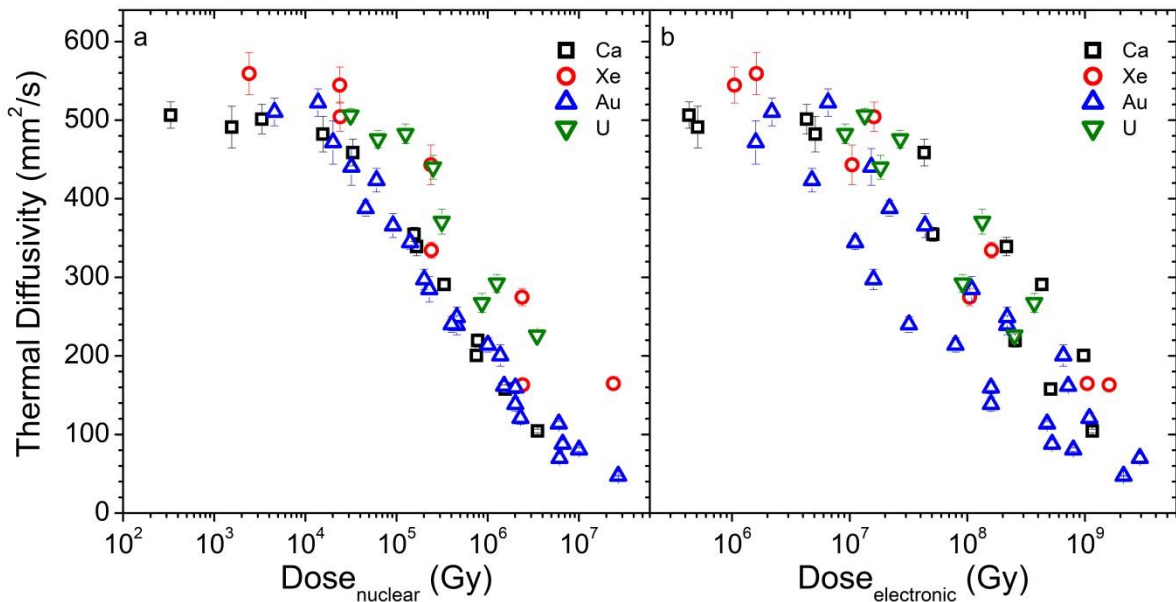


Figure 7.3 In-plane thermal diffusivity of flexible graphite as a function of dose, calculated using nuclear (left) and electronic (right) energy loss of Ca, Xe, Au and U ions.

### 7.1.2 Transversal laser flash analysis

Due to the very small thickness ( $\sim 21 \mu\text{m}$ ) of the tested flexible graphite samples, standard transversal laser flash analysis cannot provide reliable absolute values of out-of-plane, transversal thermal diffusivity. However, it is possible to measure the effect of ion beam irradiation on the thermal diffusivity relative to the pristine value. The thermal diffusivity in the direction of the c-axis of well oriented graphite is usually in the range of 3-20  $\text{mm}^2/\text{s}$  [134–136].

The evolution of the relative transversal thermal diffusivity values of flexible graphite irradiated with Ca, Xe and Au ions is shown in Figure 7.4. Similar to the in-plane thermal

diffusivity, the transversal thermal diffusivity of irradiated flexible graphite decreases with accumulation of radiation damage, although the degradation is smaller. The increase of the beam induced effect for heavier ions and closer towards the end of the ion range indicate a correlation with the nuclear energy loss. Thus, interstitials and vacancies produced by elastic collisions also disturb the lattice and increase the phonon scattering in the c-axis direction.

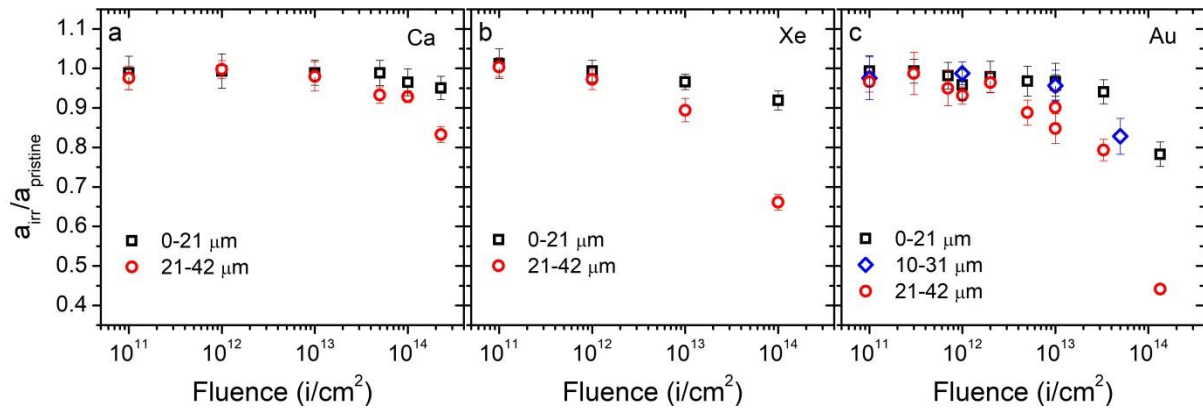


Figure 7.4 Relative transversal thermal diffusivity of flexible graphite irradiated with 4.8 MeV/u Ca, Xe and Au ions.

---

---

## 7.2 Quasi-isotropic polycrystalline graphite

---

Consisting of small anisotropic crystallites, fine grained polycrystalline graphite has quasi-isotropic properties on the macroscopic level. As a result, the average thermal conductivity is limited in comparison with the in-plane thermal conductivity of well-oriented graphite. Despite the limitation due to the small crystallite size and grain boundaries, the overall conductivity is much higher than the out-of-plane conductivity due to the random orientation of the crystallites.

Thermophysical properties of pristine and ion irradiated polycrystalline graphite were measured using laser flash analysis and photothermal radiometry.

---

### 7.2.1 Laser flash analysis

---

A series of ion beam irradiated polycrystalline graphite samples were measured by laser flash analysis. At first, the transversal LFA measurements were performed on disc samples (diameter 10 mm) with thickness from 40  $\mu\text{m}$  to 1 mm. The thinnest samples were completely penetrated by the beam and were analyzed using the one-layer model. The irradiated samples with thickness more than the ion range were measured using both the 1- and 2-layer model. The 1-layer model gives the average thermal diffusivity of partly irradiated sample, while the 2-layer model yields the thermal diffusivity of the irradiated layer with a set thickness. As discussed above, the transversal LFA measurements are problematic due to the high thermal conductivity of the investigated samples. For a reliable measurement, the characteristic half-time of the laser heating should be much less than the pulse length. When this condition is not fulfilled, the measured thermal diffusivity has a severe systematic error, which does not allow us to deduce the correct absolute value. For thick samples ( $\sim 1$  mm), the contribution of the irradiated layer is very small in comparison with the pristine layer, so the thermal resistance formalism is also not reliable.

In-plane LFA measurements of  $\sim 50$   $\mu\text{m}$  thick pristine and irradiated graphite overcome the limitations of the transversal measurements and provide reliable results. Figure 7.5 illustrates that the measured half time is much longer than the laser pulse length of 0.3-0.7 ms. The signal for all Ca ion irradiated samples stays almost the same up to a fluence of  $5 \times 10^{13}$  ions/cm<sup>2</sup>. Thus, we conclude that the irradiation does not induce significant changes. In the case of the Au ion irradiation, increasing the fluence results in a longer time for the heat to propagate through the sample, which is a clear indication for a reduced thermal diffusivity of the irradiated graphite.

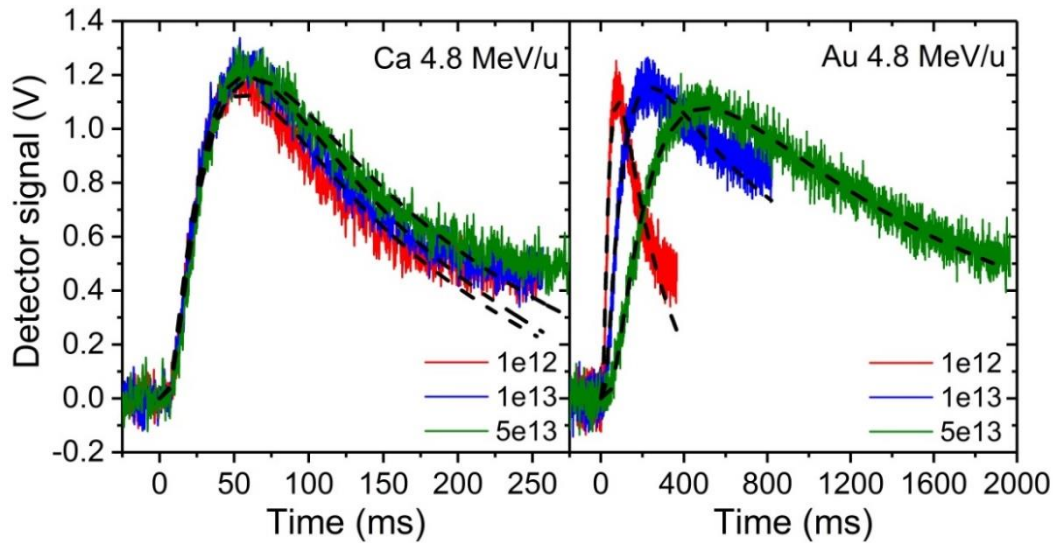


Figure 7.5 Example of LFA detector signal of in-plane measurements of 4.8 MeV/u Ca and Au ion irradiated polycrystalline graphite. Dashed lines are fits to the experimental data.

Absolute and relative thermal diffusivity values of C, Ca and Au ion irradiated polycrystalline graphite were calculated from the fit of the LFA heating curves and are presented in Figure 7.6. The effect of the irradiation with light ions (C and Ca) on the thermal diffusivity is very small and can hardly be observed up to a fluence of  $5 \times 10^{13}$  ions/cm<sup>2</sup>. At this fluence, the Au ion irradiation leads to a thermal diffusivity degradation down to  $\sim 10$  mm<sup>2</sup>/s corresponding to approximately 13% of the initial value. Even at the maximum achieved fluence, the thermal diffusivity decrease does not show any saturation. Thermal diffusivity degradation caused by the Au ion irradiation with slightly different energies of 4.8 and 5.9 MeV/u show a similar trend.

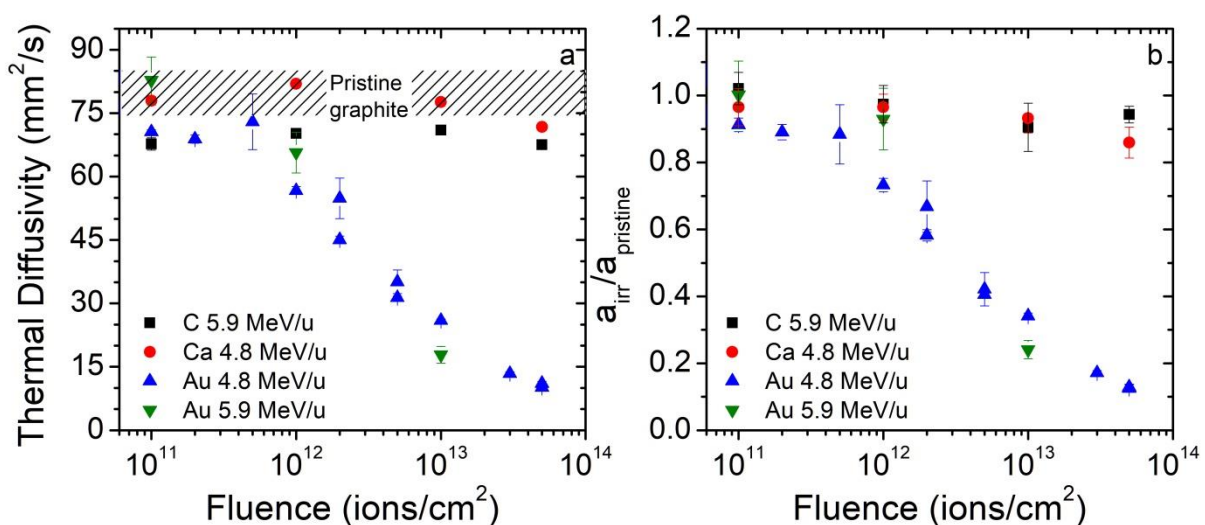


Figure 7.6 In-plane thermal diffusivity of the polycrystalline graphite irradiated with C, Ca and Au ions. (left) - absolute values; (right) - relative thermal diffusivity change with respect to the thermal diffusivity of pristine polycrystalline graphite.

---

## 7.2.2 Photothermal radiometry

---

As transversal laser flash analysis is not a suitable technique to measure relatively thin and multilayered polycrystalline graphite samples, these samples were characterized using photothermal radiometry. The high sensitivity of PTR and the possibility of depth profiling make this method appropriate for characterization of partly irradiated polycrystalline graphite samples.

Before analysis of the irradiated samples, pristine polycrystalline graphite samples were measured using PTR.

---

### 7.2.2.1 Pristine polycrystalline graphite

---

In order to determine the thermophysical properties of the non-irradiated sample layer, PTR measurements were initially performed on a pristine polycrystalline graphite reference sample. The front and the rear surfaces of the sample were machined in a different way, one was cut (mean roughness  $R_a \approx 1.12 \mu\text{m}$  and maximum peak-to-valley height  $R_t \approx 6.15 \mu\text{m}$ ), while the other surface was additionally lapped after cutting (mean roughness  $R_a \approx 0.4 \mu\text{m}$  and maximum peak-to-valley height  $R_t \approx 1.39 \mu\text{m}$ ). The surface roughness was determined using a DEKTAK contact profilometer. The normalized amplitude and phase of the thermal signal of the sample surface as a function of frequency are displayed in Figure 7.7. The estimated frequency where the thermal diffusion length  $\mu$  is equal to the entire thickness of the sample ( $\mu = L$ ) is plotted as a vertical dotted line. The dashed lines are fits using the graphite properties from the material datasheets [64] and considering only one single homogeneous graphite layer. This approach is obviously not able to adequately describe the measured data above about 20 Hz. At low frequencies, when  $\mu \geq L$ , the experimental data for cut and lapped sample surfaces are rather similar. Whereas in the mid to high frequency regime ( $\mu < L$ ), the surface treatment obviously affects the measured thermal response. Therefore, an additional effective surface layer [137,138] with different thermal properties was introduced in the model yielding a much better fit in the entire frequency range (solid lines). Thus the irradiated samples are modelled by a three-layered system consisting of the (i) surface layer, (ii) irradiated layer, and (iii) pristine substrate.

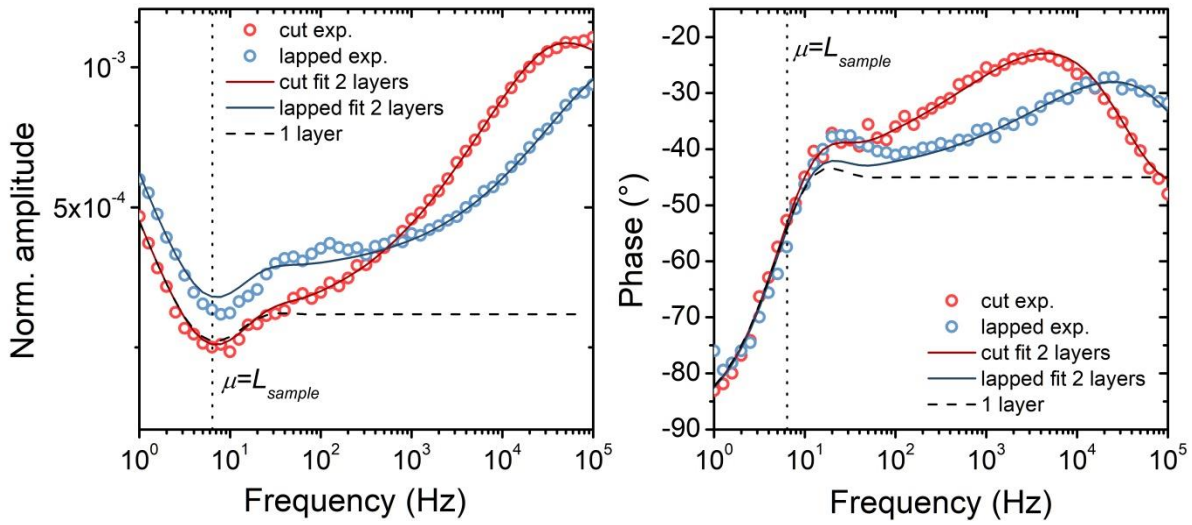


Figure 7.7 Normalized amplitude and phase of the PTR signal for a pristine polycrystalline graphite sample. Open red and blue circle symbols correspond to the respective experimental data measured on the cut only and on the lapped surface of the same sample. Solid lines are fits to the experimental data by implementing an additional surface layer. The dashed lines illustrate that fits considering only a single homogeneous graphite layer cannot describe the measured data adequately above 20 Hz. The vertical dotted line indicates the transition frequency at which the sample becomes thermally thick, i.e.  $\mu = L$ .

Introducing an additional layer to the system increases the number of variables describing the heat transport. Thus it is important to verify if some of these variables are correlated and if it is possible to deduce a correct and unique fit to the experimental data. The sensitivity analysis of the PTR amplitude and phase, recorded on the pristine reference sample, is shown in Figure 7.8. The effusivity values of the effective surface  $e_{surf}$  and substrate  $e_{bulk}$  layers are obviously inversely proportional which does not allow us to provide independent fit values. Thus, the effusivity value of bulk graphite was determined by means of LFA, yielding a thermal diffusivity of  $a = 8.1 \times 10^{-5} \text{ m}^2/\text{s}$  and a heat capacity of  $C_p = 704 \text{ Jkg}^{-1}\text{K}^{-1}$ . Inserting  $\rho = 1.84 \text{ g/cm}^3$  for the bulk density of pristine graphite from the material datasheet [31] gives a thermal effusivity of  $11.6 \times 10^3 \text{ Ws}^{1/2}\text{m}^{-2}\text{K}^{-1}$ . This value was inserted in the heat transport simulation of the layered system for the effusivity of the non-irradiated graphite substrate. The fit parameters obtained for a 2-layer system (effective surface layer on top of pristine graphite) are summarized in Table 7.1.



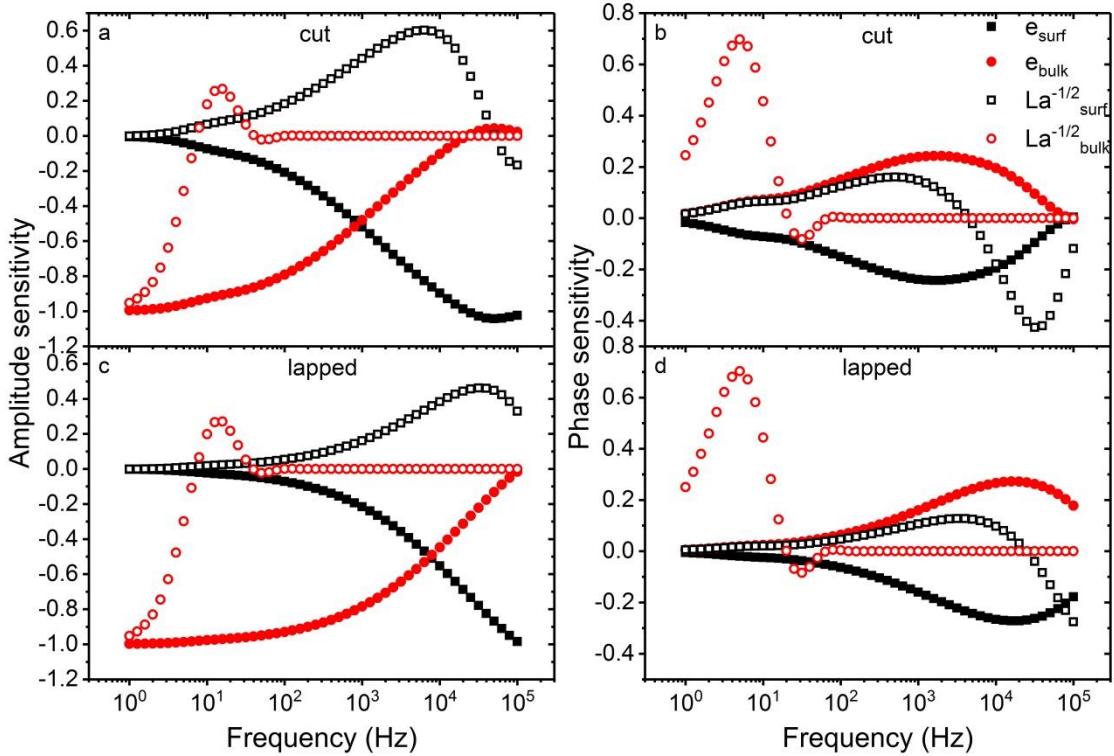


Figure 7.8 Sensitivity of amplitude and phase to the fit parameters for pristine polycrystalline graphite sample with cut (a, b) and lapped (c, d) surfaces.

Table 7.1 Thermal effusivity  $e$  of pristine graphite (SIGRAFINE R6650) from laser flash analysis and PTR results for  $e$  and  $L \cdot a^{-1/2}$  of cut and lapped surface layers.

Pristine Graphite	Method	$e$ ( $\text{Ws}^{1/2}\text{m}^{-2}\text{K}^{-1}$ , $\times 10^3$ )	$L \cdot a^{-1/2}$ ( $\text{s}^{-1/2}$ , $\times 10^{-3}$ )
Bulk	LFA	$11.60 \pm 1.16$	-
Cut surface	PTR	$3.07 \pm 0.42$	$2.96 \pm 0.05$
Lapped surface	PTR	$4.37 \pm 0.60$	$1.33 \pm 0.06$

Trying to understand the nature of the surface layer detected by PTR, the measurements were performed on different isotropic polycrystalline graphite grades with nominal grain sizes of 1, 7, 10 and 20  $\mu\text{m}$  (Table 7.2).

As shown in Figure 7.9, there is no difference in the phase signal in the entire tested frequency range for the two ways of surface preparation, cutting and lapping, for POCO ZEE grade and there are just minor variations for the grade SGL R6300. In contrast, for grade SGL R6650, SGL R6550 and SGL R6500, the response of cut and lapped sample surfaces shows significant differences above about 100 Hz. We ascribe this behavior at high frequencies to the short probing depth as well as to surface roughness effects due to different grain sizes.



Table 7.2 Density and average grain size of different polycrystalline graphite grades as presented in the datasheets [139,140]; thermal diffusivity values were measured using laser flash analysis.

Graphite grade	Density (g/cm <sup>3</sup> )	Grain size (μm)	Thermal diffusivity (mm <sup>2</sup> /s)
Poco ZEE	1.77	1	28.4 ± 0.2
SGL R6650	1.84	7	80.8 ± 0.6
SGL R6550	1.83	10	81.4 ± 0.6
SGL R6500	1.77	10	73.3 ± 0.9
SGL R6300	1.73	20	61.4 ± 0.6

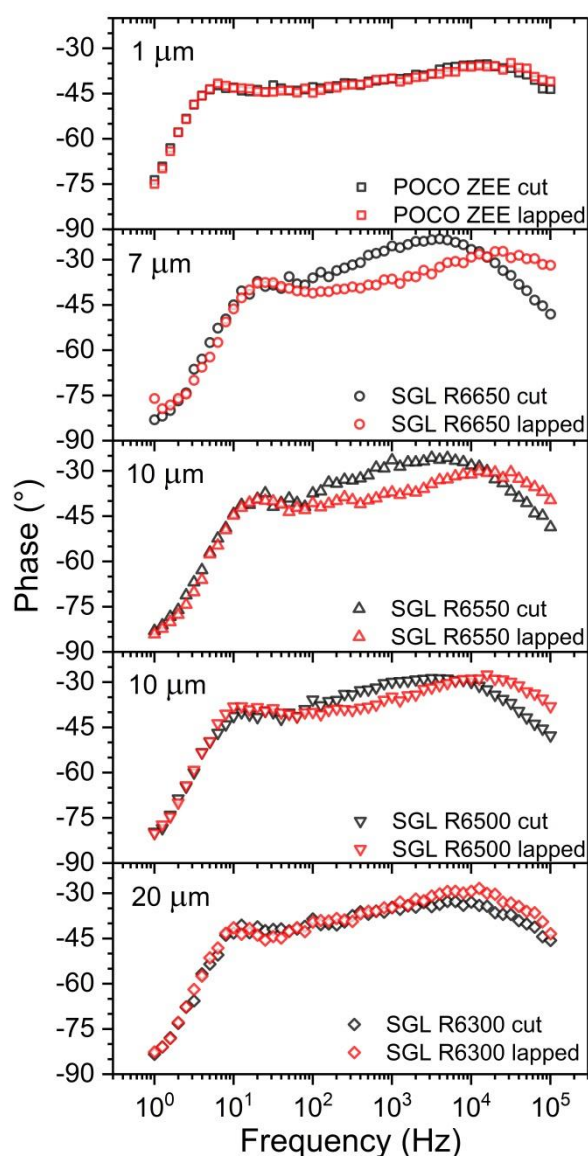


Figure 7.9 Scanning PTR measurements: phase response versus frequency for isotropic polycrystalline graphite grades with a nominal grain size of 1, 7, 10 and 20 μm. The two curves for each grade represent the cut only and the lapped faces of the same sample.

Figure 7.10 compares surface layer properties obtained from PTR analysis for all polycrystalline graphite grades studied in this work. Effusivity and  $La^{-1/2}$  are the fitting parameters. The thermal diffusivity was deconvoluted from the effusivity using the corresponding bulk value of density and heat capacity. The thickness was calculated from  $La^{-1/2}$  and from the estimated value of the thermal diffusivity. All obtained thermal diffusivity values are in the range from 5 to 15  $\text{mm}^2/\text{s}$ , which is comparable to the thermal diffusivity of graphite perpendicular to the basal plane and of disordered graphite. The calculated surface layer thickness ranges from 4 to 10  $\mu\text{m}$  and is comparable with the grain size and measured surface roughness. The thickness of the cut surface layer seems to be slightly correlated with the grain size, while lapping obviously leads to a very similar thickness for all grain sizes studied.

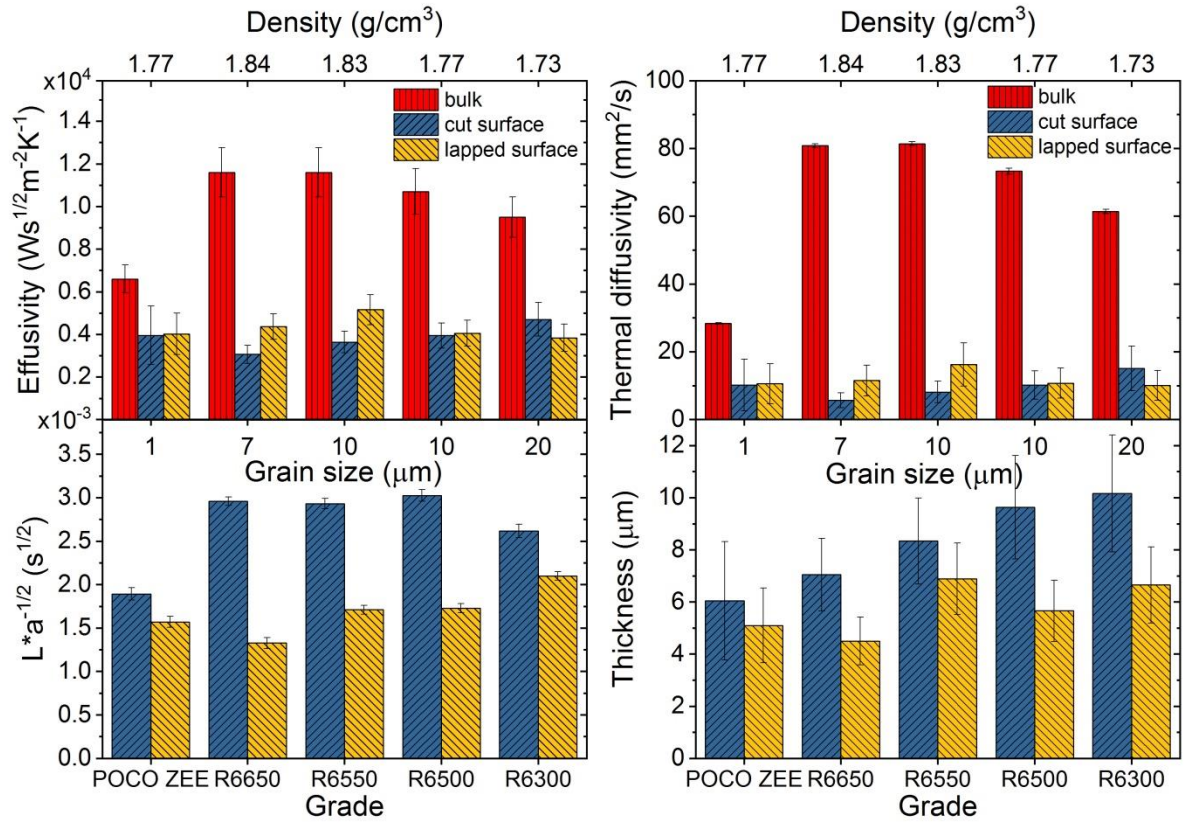


Figure 7.10 Data for different polycrystalline graphite grades (cut and lapped surfaces) including information on density and grain size. (left) effusivity and  $L*a^{-1/2}$ ; (right) thermal diffusivity and thickness calculated from the PTR data. Effusivity and thermal diffusivity of bulk graphite are obtained from the LFA measurements.

In conclusion, the surface layer which we had to introduce to model the PTR measurements seems to be related to the lapping process. Its properties depend also on the mechanical processing resulting in structural modification of the near surface layer, including crystallite refinement and residual stress [141], as well as increased hardness [142] as reported earlier for machined synthetic graphite.

---

### 7.2.2.2 Ion beam irradiated polycrystalline graphite

---

Selected PTR data of fluence series of graphite samples irradiated with C, Ca, Au and U ions are presented in Figure 7.11 showing the normalized amplitude and phase of the PTR signal as a function of frequency together with model calculations. As in the analysis of pristine graphite samples, the PTR signal at low frequencies (approx. <100 Hz) represents bulk properties, while at high frequencies mainly the thin surface layer is probed. There is an obvious difference in the evolution of the PTR signal for samples irradiated with light ions (C and Ca) compared to heavy ions (Au and U). For the C and Ca ion irradiations the low frequency part of the signal does not change with fluence. Small variations in the high frequency part might be due to differences of the surface layers from sample to sample. For the irradiation with Au and U ions, the evolution of the amplitude and phase in the scanned frequency range changes with ion fluence, indicating irradiation-induced modifications of the thermophysical properties. Since the emissivity change with fluence is below a few percent, the change of the amplitude is directly related to modified thermal properties. The overall increase in amplitude with increasing fluence is ascribed to a higher surface temperature due to a decrease of thermal effusivity and thus of thermal conductivity. At low ion fluences, the beam induced variation of thermophysical properties is very small leading to an overlap of the curves.

As mentioned above, the photothermal response of the irradiated graphite samples can be modeled with a 3-layer system (rough surface layer, 60-70  $\mu\text{m}$  thick irradiated layer, and pristine substrate), where the parameters of the pristine layer were fixed (Table 7.1) and its thickness was determined by subtracting the SRIM ion range from the total thickness of the sample. The sensitivity analysis shows no direct correlation between the four fit parameters  $e_{surf}$ ,  $e_{irr}$ ,  $(La^{-1/2})_{surf}$ , and  $(La^{-1/2})_{irr}$ . The sensitivity plots for graphite samples irradiated with 4.8 MeV/u Au are exemplarily shown in Figure 7.12. The low sensitivity of the parameters of the irradiated layer at low fluence causes a high uncertainty of these values. This is due to the relative small and non-homogeneous modification of the irradiated graphite layer in a fluence regime where ion tracks do not overlap. With increasing fluence, changes in the PTR response get more pronounced and the overall modification of the irradiated layer becomes more and more homogeneous.

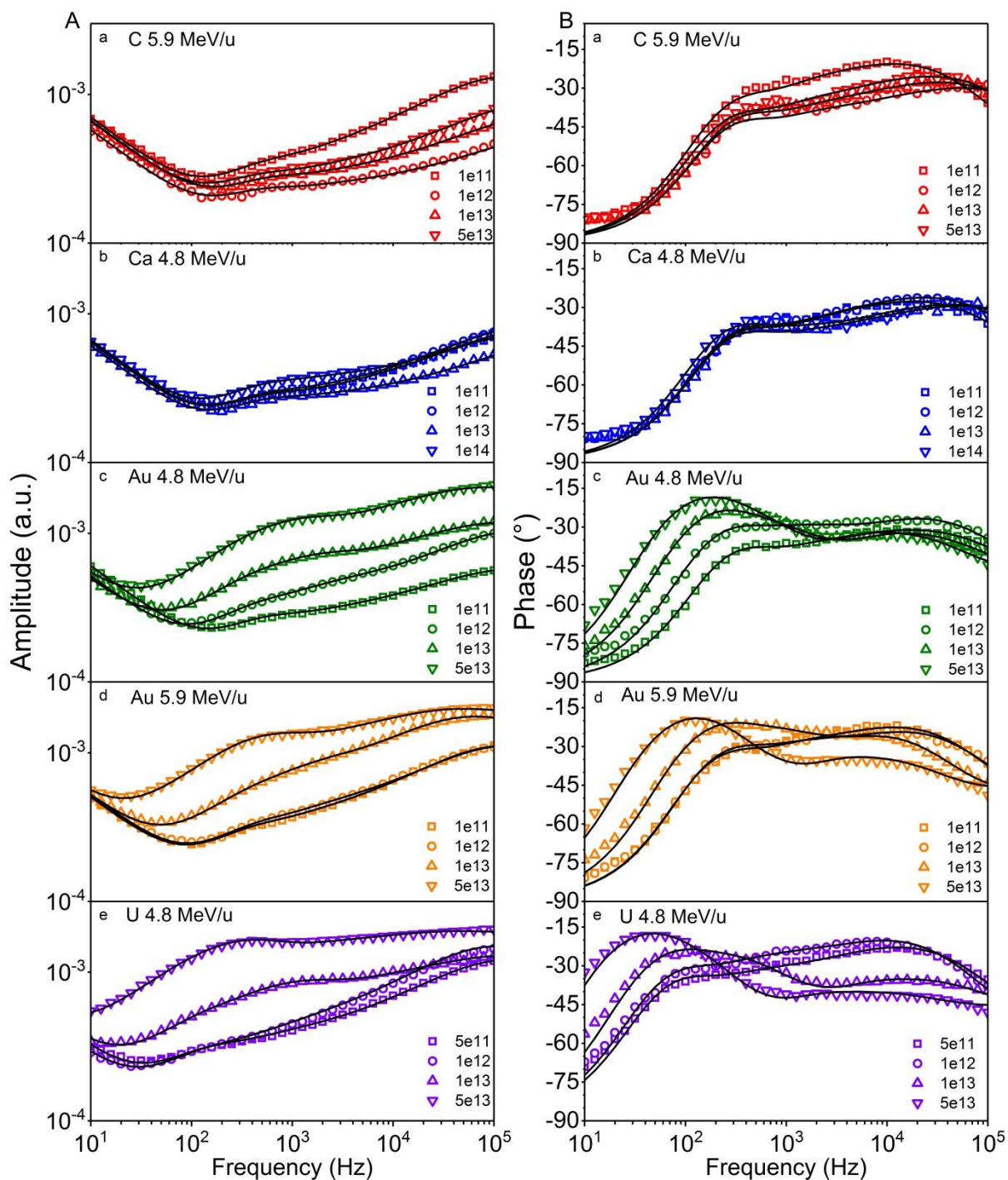


Figure 7.11 Series of PTR data for isotropic polycrystalline graphite samples irradiated with C (5.9 MeV/u), Ca (4.8 MeV/u), Au (4.8 and 5.9 MeV/u) and U (4.8 MeV/u) ions of various fluences: (A) normalized amplitude and (B) phase of thermal signal as a function of frequency. Solid lines are model fits considering a 3-layer system.



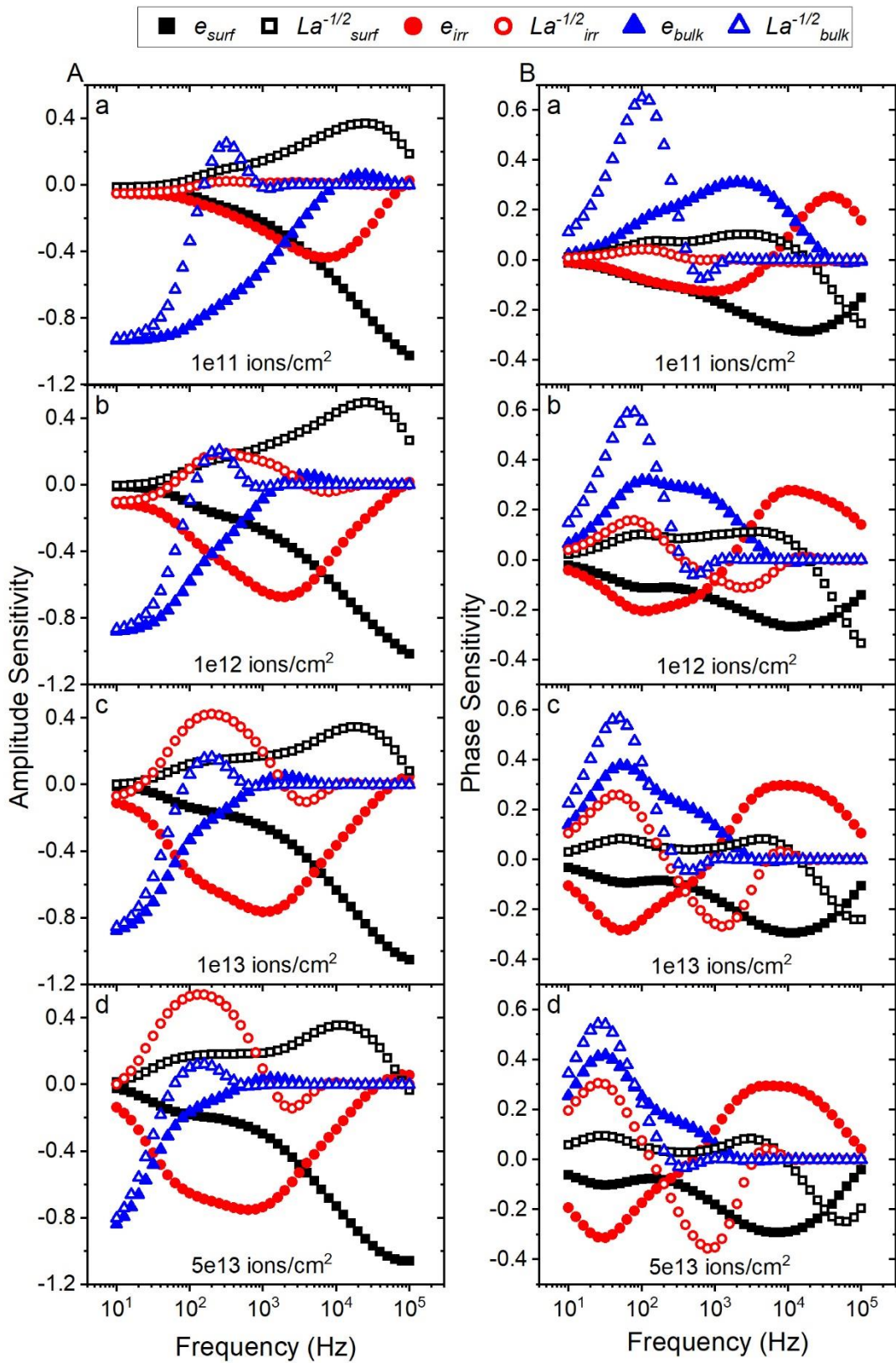


Figure 7.12 Sensitivity of amplitude (A) and phase (B) to the fit parameters for polycrystalline graphite samples irradiated with 4.8 MeV/u Au ions of fluence a)  $1 \times 10^{11}$ , b)  $1 \times 10^{12}$ , c)  $1 \times 10^{13}$ , d)  $5 \times 10^{13}$  ions/cm<sup>2</sup>.

For all irradiations the fit values of thermal effusivity  $e$  and  $La^{-1/2}$  of the modified surface (open symbols) and irradiated layer (full symbols) are presented in Figure 7.13. Ion fluence accumulation leads to degradation of  $e$  and to an increase of  $La^{-1/2}$  for both layers. The trend of the surface and the irradiated layer is the same. At the highest fluence of  $5 \times 10^{13}$  ions/cm<sup>2</sup>, the effusivity of the irradiated graphite approaches the typical value for glassy carbon ( $\sim 1500\text{-}2600 \text{ W s}^{1/2} \text{ m}^{-2} \text{ K}^{-1}$ ) calculated based on the data for Sigradur K and Sigradur G.

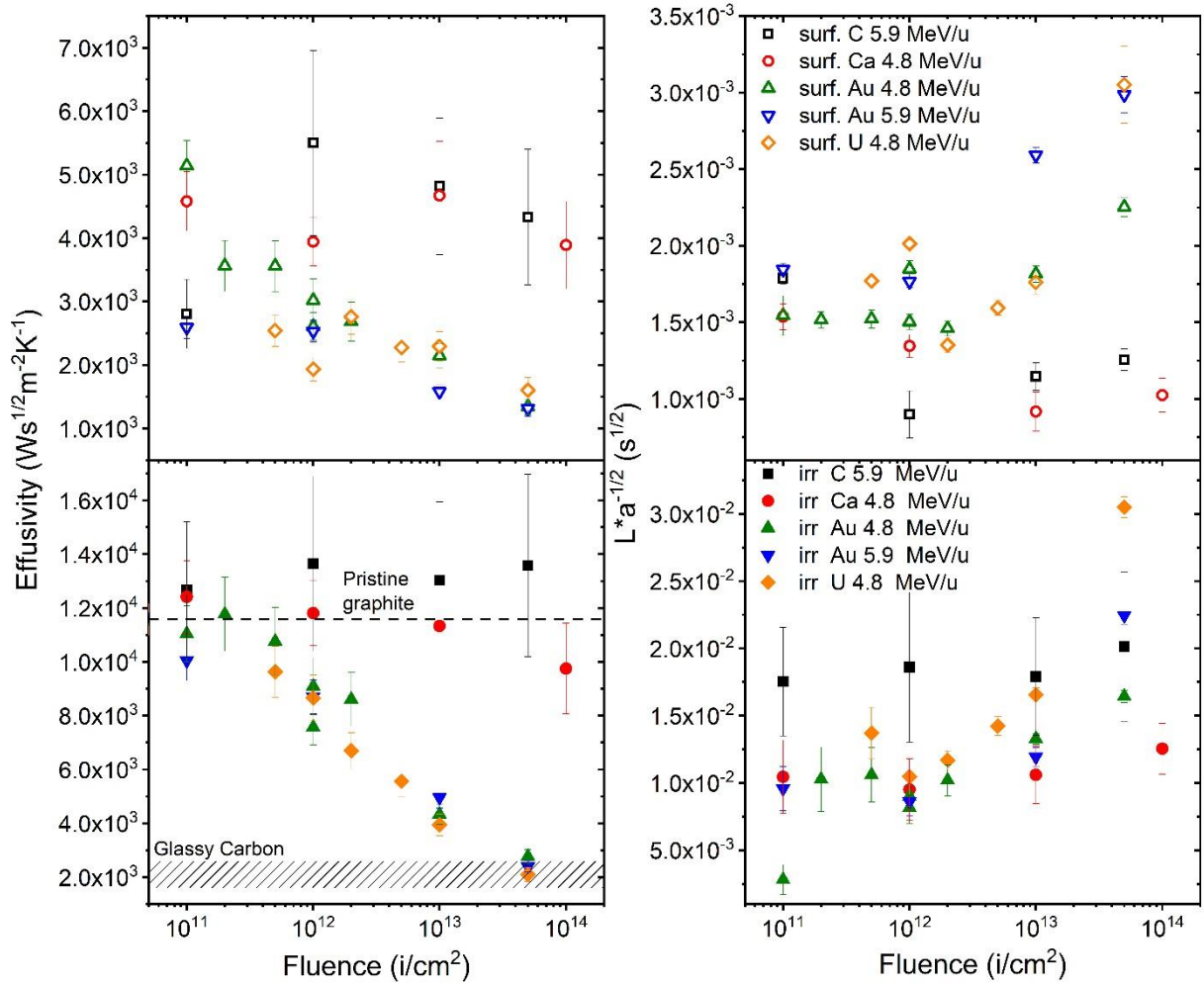


Figure 7.13 Thermal effusivity (left) and  $La^{-1/2}$  (right) values versus fluence as deduced from fits to experimental PRT data: surface layer (open symbols) and irradiated layer (full symbols) for polycrystalline graphite samples exposed to C, Ca, Au and U ion beams.

Although there is a clear increase of the  $La^{-1/2}$  value for both surface and irradiated layers with fluence, the unknown structure of the surface layer makes further deconvolution of each term of the parameter  $La^{-1/2}$  difficult. The surface layer does not show specific characteristics by means of Raman spectroscopy, optical microscopy and SEM. As a result, the estimation of the contribution of the effective surface layer to the irradiated bulk cannot be done with high precision. Nevertheless, it is reasonable to assume that the thickness of the surface layer is of



the order of the surface peak-to-valley roughness and at least an order of magnitude less than the ion range. Since the thermal diffusivity  $a$  derived from  $La^{-1/2}$  depends on the thickness at a power of 2, large thickness uncertainties cause large errors. The increase of  $La^{-1/2}$  with ion fluence for the surface and for the irradiated layer is probably mainly caused by the degradation of the thermal diffusivity  $a$  and thus of the thermal conductivity  $k$  of the layer. Previous study have shown that beam-induced swelling in graphite is only of the order of 1% indicating that a thickness change of the irradiated layer can be neglected in our calculations [143]. In a porous material such as graphite, swelling of individual crystallites may be more pronounced but is assumed to be readily accommodated by the existing porosity. In conclusion, the product  $La^{-1/2}$  qualitatively indicates a degradation of the thermal diffusivity. However, for the determination of the absolute value of the thermal diffusivity, the measured effusivity values are more suitable.

Applying the same analysis for the surface layer as for pristine graphite, it is possible to estimate the evolution of the thermal diffusivity and thickness under ion irradiation. The obtained values are presented in Figure 7.14. There is a small degradation of the thermal diffusivity of the surface layer irradiated with Au and U ions, while the irradiations with C and Ca ions do not have a significant influence. The calculated thickness of the surface layer provides no consistent trend for any of the ions, which is probably due to a variation of the initial surface quality from sample to sample.

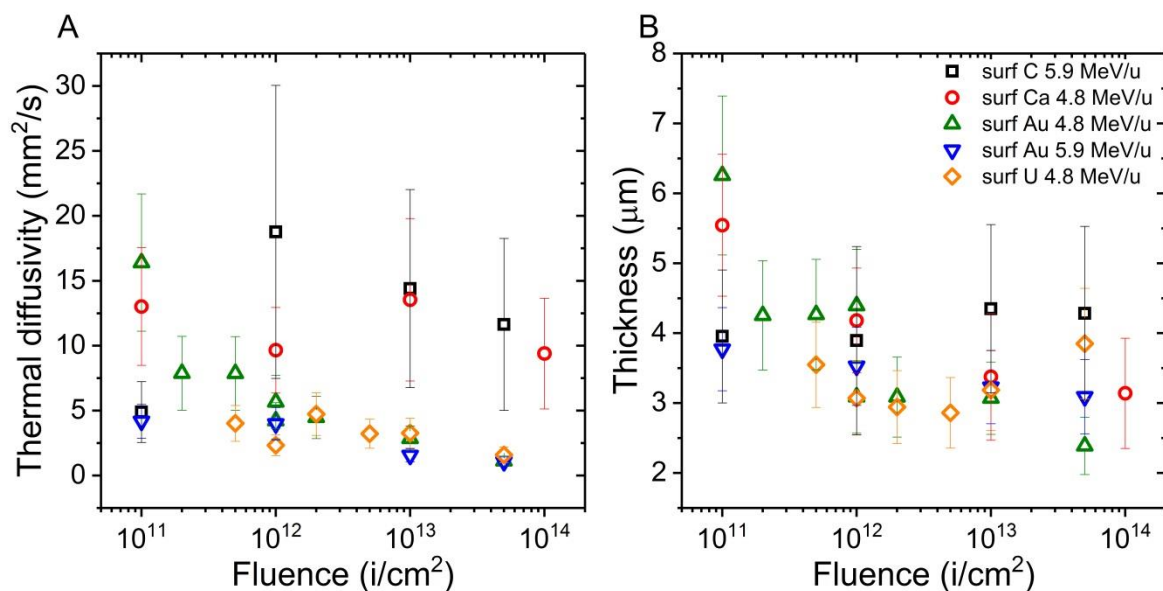


Figure 7.14 Thermal diffusivity (left) and thickness (right) of the irradiated surface layer calculated from fits of effusivity and  $L \cdot a^{-1/2}$ .

Being a general property of a material and regardless of the thickness of a sample, thermal effusivity can be used to compare the effect of the irradiation with different ions and energies. The relative thermal effusivity of the irradiated layer with respect to the pristine value (Figure 7.15) was calculated in order to estimate the degree of modification caused by ion irradiation and eliminate any dependence during fitting. The 5.9 MeV/u C ion irradiation shows no effect on the effusivity up to a fluence of  $5 \times 10^{13}$  ions/cm<sup>2</sup>. The irradiation by 4.8 MeV/u Ca ions causes a slight degradation down to 85% at a fluence of  $1 \times 10^{14}$  ions/cm<sup>2</sup>. Irradiations with 4.8 and 5.9 MeV/u Au ions as well as 4.8 MeV/u U ions lead to a drop to 20% at a fluence of  $5 \times 10^{13}$  ions/cm<sup>2</sup>.

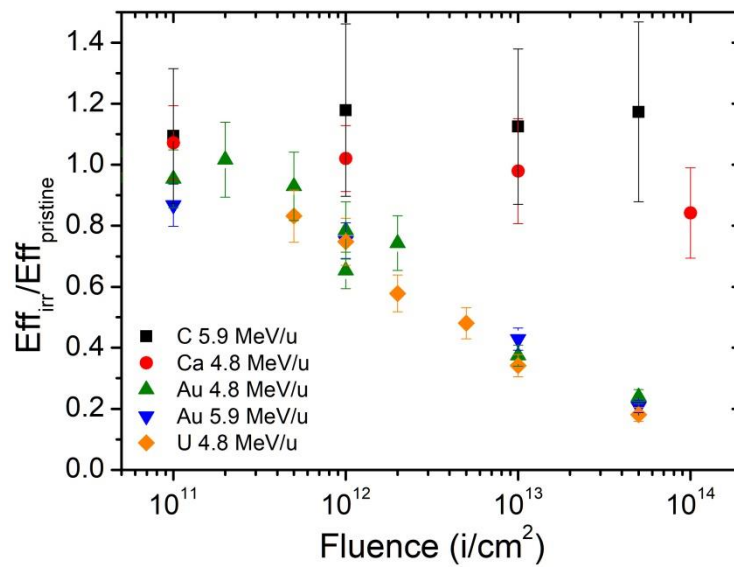


Figure 7.15 Relative thermal effusivity with respect to the pristine value as a function of fluence for polycrystalline graphite irradiated with C, Ca, Au and U ions.

As the thermal effusivity is a function of the thermal conductivity (or diffusivity) and volumetric heat capacity of a given material, we can estimate the contribution of these parameters in the observed beam-induced decrease of effusivity. The change of material density is negligible because swelling is below 1% as mentioned above. Based on results from neutron irradiation [144], we also assume that beam-induced changes of the heat capacity can be neglected. It means that the main contribution of the thermal effusivity degradation is due to the decrease of the thermal conductivity.

For technical applications it is more common to use the thermal conductivity or diffusivity rather than the effusivity. As discussed above, the determination of  $a$  from  $La^{-1/2}$  is affected by large errors. So the thermal diffusivity is quantitatively estimated from the measured  $e$  value. Inserting the volumetric heat capacity and the density of pristine graphite, the thermal diffusivity evolves as a function of fluence as shown in Figure 7.16. The trend for all studied

ions is obviously the same as for the effusivity data. The large uncertainties of the C and Ca ion irradiations are caused by the accumulation of computational inaccuracies. For the Au as well as the U beam, the thermal diffusivity drops from originally  $\sim 81 \text{ mm}^2/\text{s}$  down to only 3-5  $\text{mm}^2/\text{s}$  at the highest fluence of  $5 \times 10^{13} \text{ ions/cm}^2$ . The density difference between polycrystalline graphite and glassy carbon is about 20%. Even if we consider complete phase transition at the highest fluence and take into account the lower density of glassy carbon, the corrected thermal diffusivity does not change much and remains an order of magnitude less than the value of pristine polycrystalline graphite.

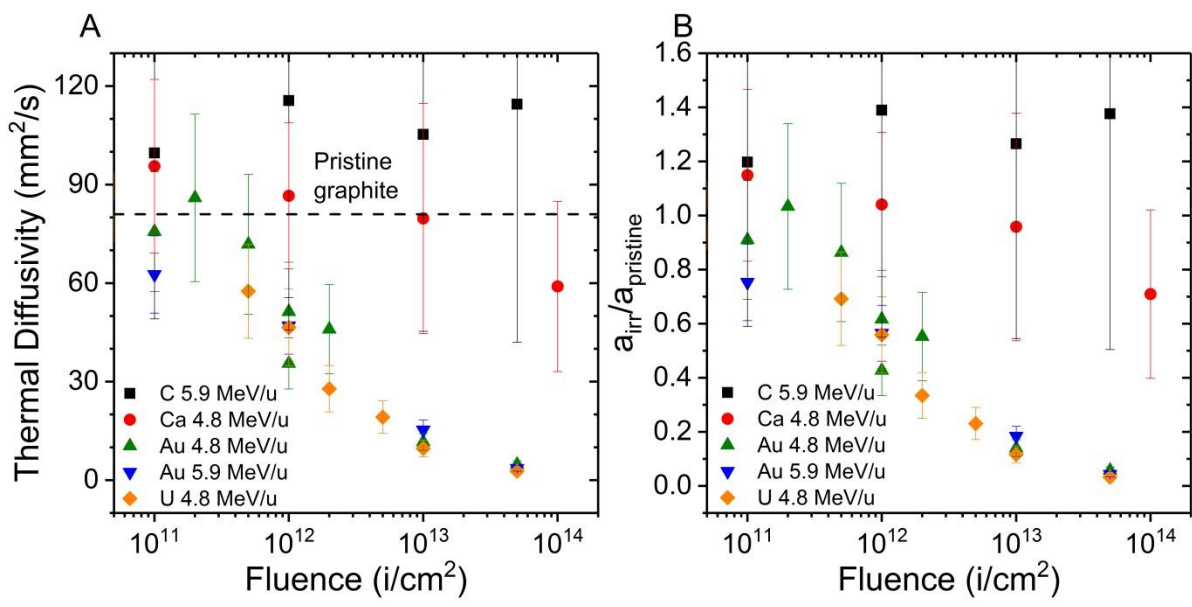


Figure 7.16 Absolute (left) and relative (right) degradation of thermal diffusivity of C, Ca, Au and U ion irradiated graphite as a function of fluence. The data were deduced from thermal effusivity measurements assuming that the pristine value of the volumetric heat capacity does not change.

---

---

### 7.3 Discussion and summary

---

Thermal diffusivity degradation induced by swift heavy ion irradiation is observed for both well-oriented and quasi-isotropic graphite. The degradation rate depends on the initial structure of the material and on the projectile mass.

Well-oriented flexible graphite shows a high sensitivity to radiation damage in both in-plane and through-plane direction when irradiated with light as well as with heavy ions. The small thickness of the samples ( $\sim 21 \mu\text{m}$ ) allowed us to probe beam-induced degradation of the thermal diffusivity in the energy loss regimes dominated by electronic and nuclear stopping. The decrease of thermal diffusivity was found to be highly correlated to the accumulated nuclear dose.

In contrast to flexible graphite, the thermal diffusivity of quasi-isotropic polycrystalline graphite exhibits a strong degradation for heavy (Au and U) ions, while under the irradiation of light ions (C and Ca) it remains almost unchanged up to a fluence of  $1 \times 10^{14}$  ions/cm<sup>2</sup>. Due to the sample geometry of polycrystalline graphite, thermophysical measurements were performed in such a way, that it was impossible to distinguish between the electronic and nuclear energy loss regimes of the different ion species. Both LFA and PTR techniques applied for thermophysical characterization of polycrystalline graphite provide comparable results (see Figure 7.2 and Figure 7.16). Small variation between the two methods can be assigned to the in-plane and through-plane orientation of the measured heat propagation due to incomplete isotropy of fine grain polycrystalline graphite.

Thermal diffusivity degradation induced by swift heavy ions in graphite has not been studied before. The data of radiation effect on thermophysical properties of graphite is available only for neutron irradiated nuclear polycrystalline graphite and can be compared with the present study based on the dpa calculation of collisional-cascade induced displacements along the ion trajectory. For the Au ion irradiation at highest fluence of  $5 \times 10^{13}$  ions/cm<sup>2</sup>, the dpa value calculated using SRIM-2013 Kinchin-Pease Quick [145] with a displacement energy of 25 eV [146,147] is of the order of  $10^{-3}$  for the first 80 % of the irradiated layer thickness. For the last 20 % of this layer the dpa value gradually increases to  $5 \times 10^{-2}$ . The relative change of the thermal diffusivity (conductivity) of polycrystalline graphite samples induced by swift heavy ions is larger than the one caused by room temperature neutron irradiations at the same dpa value [18,20]. This indicates that elastic collisions are not the only responsible mechanism for the degradation of the thermal transport properties of graphite irradiated with swift heavy

---

ions. Obviously the electronic energy loss, i.e. damage creation via ionization/excitation processes and coupling to the atomic lattice also plays an important role.

The strong degradation of the thermal diffusivity with increasing fluence is in good agreement with structural transformations in irradiated graphite observed by Raman spectroscopy. The large number of defects produced along the entire length of the projectile path has a strong influence on the properties of graphite. Previous molecular dynamics simulations showed that carbon materials have the tendency to recrystallize into faulty  $sp^2$  structures with non-6-membered carbon rings during the ultrafast cooling of the lattice in the ion tracks [29]. Such defects induce fragmentation, bending, and interconnections of basal planes, but the predominant  $sp^2$  structure is retained. Taking into account that the main heat carriers in graphite are phonons [61–63,135,148], the degradation of the conductivity  $k$  is ascribed to a decrease of the phonon mean free path due to enhanced phonon scattering at defects and newly formed grain boundaries. This is supported by the finding of Fugallo et al [148] who demonstrated a pronounced decrease of the lattice thermal conductivity of graphene and graphite when the crystallite size becomes smaller than 10  $\mu\text{m}$ . Irradiation-induced point defects have also an important contribution to the degradation of thermal conductivity in graphene and graphite as shown by means of molecular dynamics simulations [27,149].

---

## 8 Ion damage cross-section

---

Analyzing the fluence dependence of the different parameters studied, it is possible to estimate the damage cross-section corresponding to a single ion impact.

As discussed in section 6.1.2, the finite crystallite size has a negligible contribution in the evolution of the D-band of irradiated flexible graphite. At the same time even at the highest achieved fluence the ratio  $I_D/I_G$  monotonously increases, and there is no observable transition to amorphous carbon at which the ratio  $I_D/I_G$  decreases while FWHM(G) still increases. This is in agreement with reference [14], reporting no turning point in the evolution of  $I_D/I_G$  for the ion irradiated HOPG in contrast to graphene, for which the local activation model was developed (see section 5.2) [84].

For swift heavy ions, the damage in many materials is produced by a direct ion impact. The corresponding damage cross section  $\sigma$  can be deduced from the exponential dependence of a measured parameter on the fluence  $\Phi$  by equation 8.1:

$$Y = Y_0 + A \cdot (1 - e^{-\sigma\Phi}) \quad 8.1$$

where  $Y$  is a measured quantity,  $Y_0$  is its initial value, and  $A$  defines the amplitude of the change [150]. We applied Eq. 8.1 to the evolution of the different Raman parameters  $I_D/I_G$ , FWHM(G) and  $I_{2D}/I_G$  as a function of fluence  $\Phi$  for flexible graphite irradiated with Ca, Xe, Au and U ions. The corresponding fits by Eq. 8.1 are presented in Figure 8.1. For each Raman parameter a global fit was used for all ions with a common initial value  $Y_0$  limited by the measured pristine value of the corresponding parameter, and an amplitude coefficient  $A$  defining the same final level of the beam induced changes. The obtained damage cross-sections are summarized in Table 8.1.

As shown before, in swift heavy ion irradiated flexible graphite the inelastic interaction has a negligible effect on damage formation. The damage cross-sections for Ca, Xe, Au and U ion irradiated flexible graphite, obtained for different Raman parameters, as a function of the nuclear energy loss calculated using SRIM-2013 is shown in Figure 8.2. In some cases, the beam induced changes on the front face of the front samples are too small for a reliable fit leading to large uncertainties. These points are excluded from the figure. The calculated damage cross-section overall consistently increases with increasing nuclear energy loss. The damage cross-sections, calculated based on  $I_D/I_G$ , FWHM(G) and  $I_{2D}/I_G$ , show different values for the corresponding energy loss. This is rationalized by the different origin of the G, D, and 2D bands and hence different sensitivity to impact on them created by defects. As mentioned



before, the D band is linked to the density of point or linear defects in carbon lattice. The linewidth of the G band represents the degree of crystallinity, which requires a large amount of point defects for certain changes in structural order. The damage cross-sections deduced from FWHM(G) are overall smaller than the ones deduced from the relative intensity of the D-band. The 2D-band is associated to the stacking order of graphite basal planes, which is influenced by the produced vacancies and interstitials. The largest damage cross-sections deduced from the relative intensity of the 2D-band might be explained by changes in the stacking order of large carbon flakes which might spread over a broad area. The obtained values of damage cross-section is in agreement with a previous study on HOPG irradiated with highly-charged 4 MeV Kr<sup>19+</sup> ions [14].

It should be noted, that the application of the direct impact model to the analysis of the defect cascade caused by nuclear energy loss yields in most cases very low damage cross sections (below 1 nm<sup>2</sup>) indicating the generally low probability of defect creation and thus high radiation hardness of graphite.

Table 8.1 Damage cross-sections  $\sigma$  deduced from fits to the different Raman data  $I_D/I_G$ , FWHM(G) and  $I_{2D}/I_G$  of ion irradiated flexible graphite.

Ion	Depth ( $\mu\text{m}$ )	$\sigma_{I(D)/I(G)}$ (nm <sup>2</sup> )	$\sigma_{\text{FWHM}(G)}$ (nm <sup>2</sup> )	$\sigma_{I(2D)/I(G)}$ (nm <sup>2</sup> )
Ca	0	0.05 $\pm$ 0.03	0.02 $\pm$ 0.03	0.12 $\pm$ 0.05
	21	0.12 $\pm$ 0.03	0.05 $\pm$ 0.02	0.30 $\pm$ 0.06
	42	3.47 $\pm$ 0.91	1.83 $\pm$ 0.33	12.91 $\pm$ 2.08
Xe	0	0.18 $\pm$ 0.08	0.07 $\pm$ 0.07	0.39 $\pm$ 0.12
	21	0.34 $\pm$ 0.07	0.22 $\pm$ 0.06	1.04 $\pm$ 0.18
Au	0	0.39 $\pm$ 0.08	0.27 $\pm$ 0.06	1.09 $\pm$ 0.15
	10	0.88 $\pm$ 0.21	0.77 $\pm$ 0.18	1.94 $\pm$ 0.37
	21	0.78 $\pm$ 0.09	0.86 $\pm$ 0.10	2.69 $\pm$ 0.29
	31	4.10 $\pm$ 0.80	3.88 $\pm$ 0.70	15.30 $\pm$ 3.97
	42	15.24 $\pm$ 1.66	7.28 $\pm$ 0.78	37.46 $\pm$ 5.77
U	0	0.16 $\pm$ 0.48	0.43 $\pm$ 0.45	0.09 $\pm$ 0.67
	21	0.65 $\pm$ 0.37	0.49 $\pm$ 0.33	2.86 $\pm$ 0.60
	42	4.29 $\pm$ 0.60	1.70 $\pm$ 0.39	11.69 $\pm$ 1.60

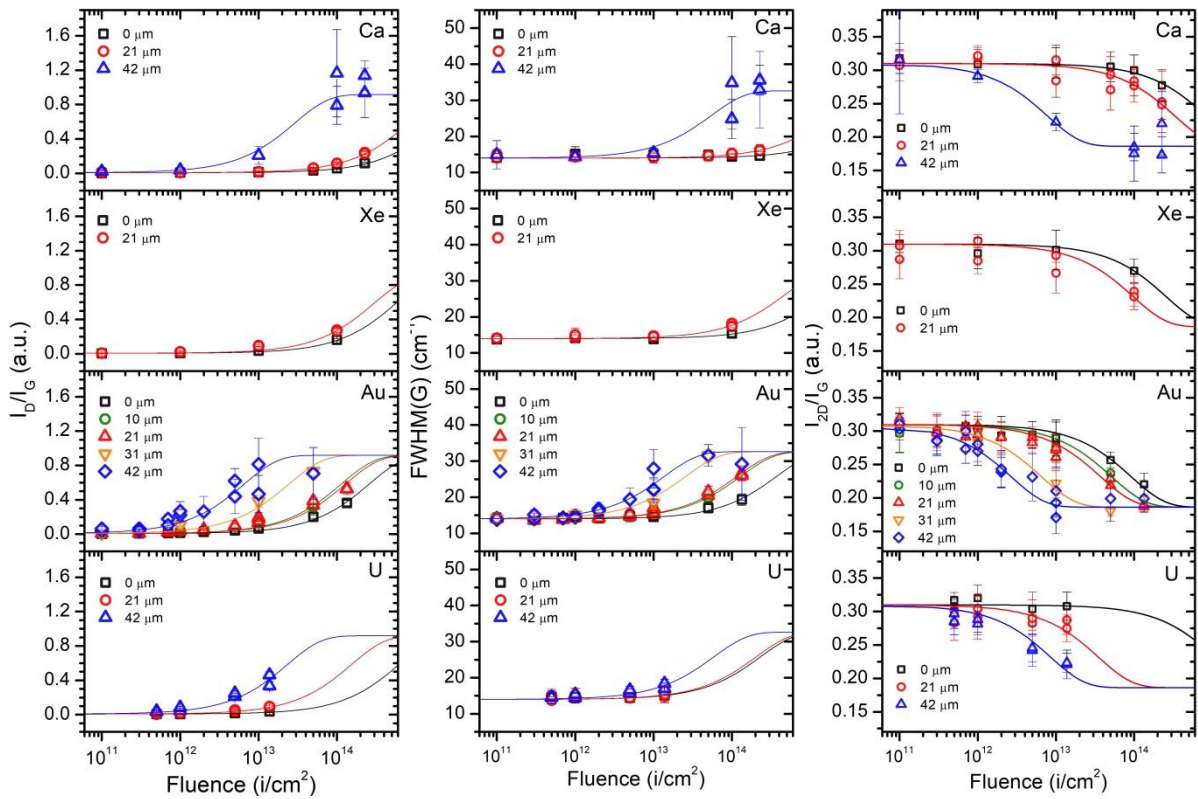


Figure 8.1  $I_D/I_G$ , FWHM(G) and  $I_{2D}/I_G$  (symbols) and corresponding fits (lines) as a function of fluence for flexible graphite irradiated with Ca, Xe, Au and U ions at different depth along the ion range.

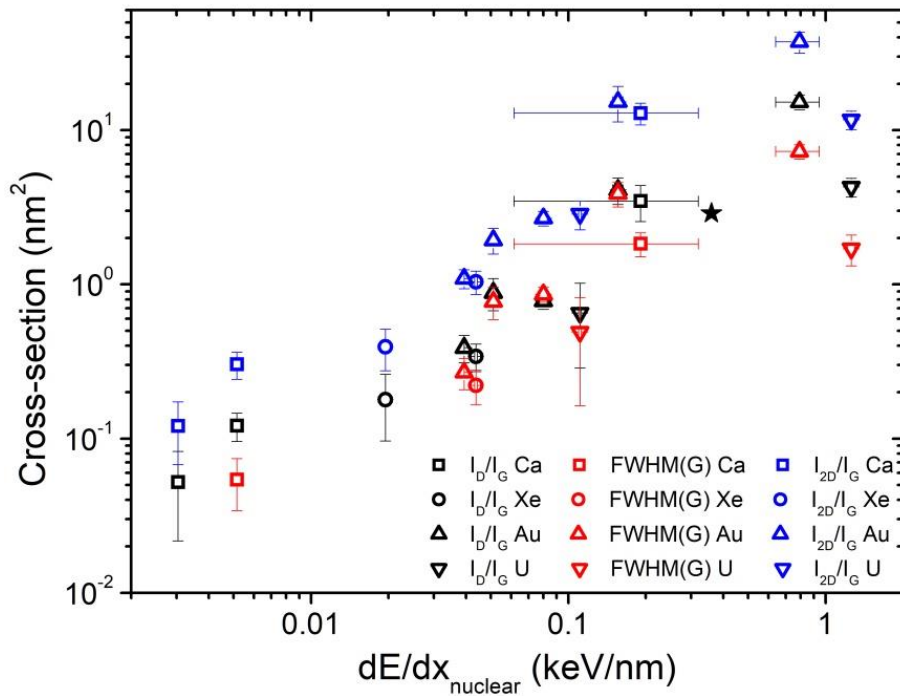


Figure 8.2 Damage cross-section of Ca, Xe, Au and U ions in flexible graphite as a function of nuclear energy loss, calculated based on fits to the fluence evolution of Raman parameters FWHM(G),  $I_D/I_G$ , and  $I_{2D}/I_G$ . The black star shows a value reconstructed for HOPG irradiated with 4 MeV Kr ions from reference [14].

The fit approach based on Eq. 8.1 was also used for the analysis of damage cross-sections deduced from the thermophysical properties degradation of the irradiated flexible and polycrystalline graphite.

The fit of the relative thermal diffusivity of irradiated flexible graphite is presented in Figure 8.3. Although the saturation level was not reached for all ions, we assumed that the final high-fluence value of the thermal diffusivity would reach the same level. The left graph shows a fit for the Ca and Au ions using Equation 8.1 with  $Y_0$  fixed to 1 and a common degradation amplitude  $A$ . The deduced fit parameters are summarized in Table 8.2. There is a significant deviation between the experimental data and the fit functions. In the regime of intermediate fluences ( $\sim 1 \times 10^{11}$  -  $1 \times 10^{13}$  ions/cm<sup>2</sup>) the measured degradation of the thermal diffusivity appears to be more pronounced, and at higher fluences ( $\sim 1 \times 10^{13}$  -  $1 \times 10^{14}$  ions/cm<sup>2</sup>) it is smaller than the fit by a single exponential function.

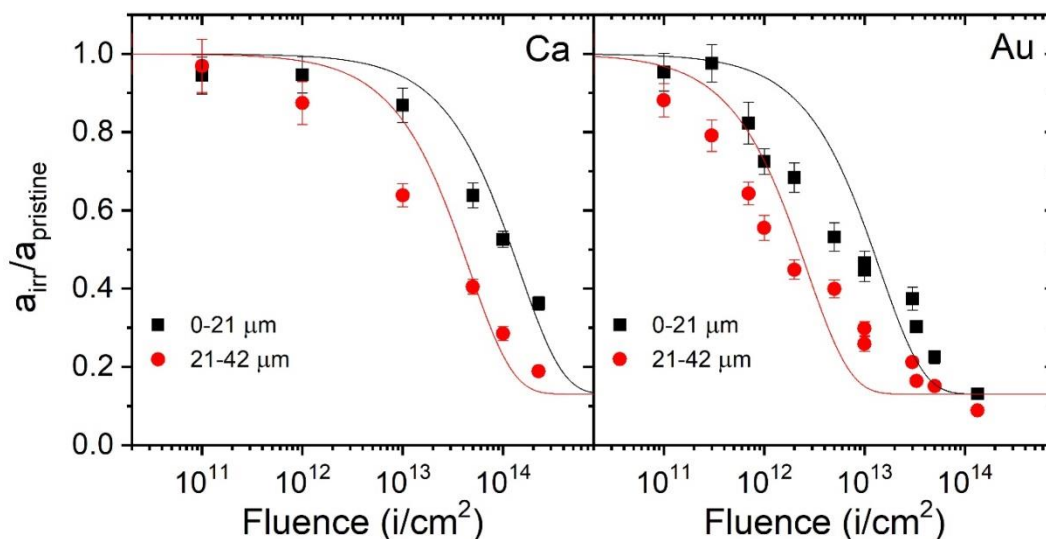


Figure 8.3 Relative thermal diffusivity as a function of ion fluence for flexible graphite irradiated with Ca and Au ions. Lines represent exponential fits (Eq. 8.1) by a single impact model.

Table 8.2 Damage cross sections deduced from fits to LFA data of flexible graphite irradiated with Ca and Au ions. Amplitude  $A$  of Eq. 8.1 is in all cases  $-0.87 \pm 0.01$ , and  $Y_0$  is set to 1.

Ion	Sample	Cross-section $\sigma$ (nm <sup>2</sup> )
Ca	0-21 $\mu\text{m}$	$0.69 \pm 0.14$
	21-42 $\mu\text{m}$	$2.18 \pm 0.49$
Au	0-21 $\mu\text{m}$	$7.06 \pm 1.48$
	21-42 $\mu\text{m}$	$37.73 \pm 9.04$

For flexible graphite, the direct impact model is obviously not suitable to describe the evolution of the thermal diffusivity with increasing fluence. The model considers a continuous material modification as typical for cylindrical ion tracks produced in the electronic energy loss regime, whereas our Raman spectroscopy analysis show that elastic collisions mainly contribute to the radiation damage by producing distributed point defects.

The same exponential function fit was applied to the relative thermal diffusivity and effusivity degradation of polycrystalline graphite irradiated with Au and U ions (see Figure 8.4). The irradiation with C and Ca ions up to the highest fluence have only a slight effect on polycrystalline graphite and the data is not suitable for a reliable fit. Table 8.3 shows the parameters of fits to the thermal diffusivity and effusivity data of polycrystalline graphite irradiated with Au and U ions. In contrast to the flexible graphite data, the degradation of the thermophysical properties of polycrystalline graphite follows quite well the single impact model. This behavior can be correlated with the electronic energy loss, which has a significant impact on structural modifications in PG as discussed before. Thus in polycrystalline graphite, the degradation of the thermal diffusivity and effusivity by 4.8 MeV/u Au and U ions can be reasonably approximated by a damage cross-section of 20-25 nm<sup>2</sup>.

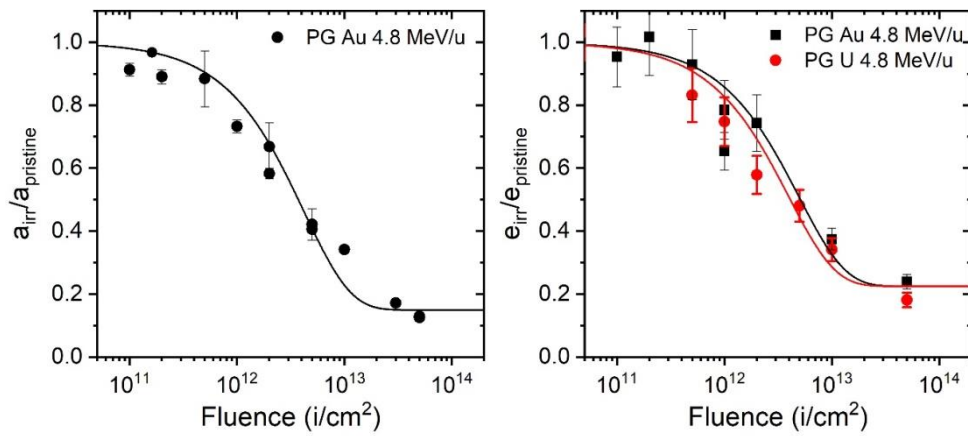


Figure 8.4 Relative thermal diffusivity (left) and effusivity (right) as a function of applied fluence for polycrystalline graphite irradiated with Au and U ions. Lines represent exponential fits (Eq. 8.1) by a single impact model.

Table 8.3 Damage cross sections deduced from fits (Equation 8.1) to thermal diffusivity and effusivity data of polycrystalline graphite irradiated with Au and U ions.

Method	Ion	Amplitude $A$	Cross-section $\sigma$ (nm <sup>2</sup> )
LFA	Au	$-0.85 \pm 0.02$	$23.80 \pm 2.56$
PTR	Au	$-0.78 \pm 0.02$	$20.31 \pm 4.49$
	U		$25.25 \pm 4.74$

---

## 9 Correlation of thermal diffusivity and Raman parameters

---

Although the thermal diffusivity or conductivity measurements are relatively simple, they usually require a bulk sample. Carbon-based samples often cannot be analyzed using standard methods for thermophysical characterization because of a complicated sample geometry or because the samples are too thin. However, this kind of samples can be easily investigated by Raman spectroscopy. Within this thesis, thermal diffusivity and Raman parameters were deduced for a broad variety of ion-irradiated carbon-based samples. Compiling this data together can provide a correlation that allows Raman spectroscopy data to be used for an approximate estimation of the thermal diffusivity.

The thermal diffusivity as a function of the Raman parameters  $I_D/I_G$  and  $I_{2D}/I_G$  for pristine and ion-irradiated flexible graphite and polycrystalline graphite, as well as two grades of glassy carbon (Sigradur K and Sigradur G) is shown in Figure 9.1. The top and bottom images show the same data in a linear and logarithmic scale, respectively. For flexible graphite, the in-plane thermal diffusivity is used. The corresponding values of  $I_D/I_G$  and  $I_{2D}/I_G$  were obtained by averaging this parameter for the front and the back sides of each sample. The thermal diffusivity of polycrystalline graphite was deduced from the photothermal radiometry measurements. The respective values of  $I_D/I_G$  and  $I_{2D}/I_G$  were calculated by averaging the values measured on the sample cross-sections along the ion range.

As discussed above, the thermal diffusivity of graphite is correlated with the defect density, which is represented by the ratios  $I_D/I_G$  and  $I_{2D}/I_G$ . The more disorder is present in a sample, the smaller is its thermal diffusivity. This dependence shows good consistency for both well-oriented flexible graphite and quasi-isotropic polycrystalline graphite in pristine and irradiated conditions. The “low temperature” glassy carbon (Sigradur K), which represents a large disorder limit, follows the same trend. The “high temperature” glassy carbon (Sigradur G) demonstrates a noticeable deviation, which can be ascribed to structural rearrangements into larger bent graphite flakes during high temperature treatment, which is not monotonously seen in the corresponding Raman spectra (see Figure 6.14).

By using the mentioned dependences one should keep in mind that the Raman spectroscopy probes just the surface of a sample, while the thermal diffusivity is a property of bulk material. Thus, the estimation of the thermal diffusivity based on the Raman parameters is reasonable only in the case when the surface represents the whole sample and is not additionally altered, for example, by mechanical treatment.

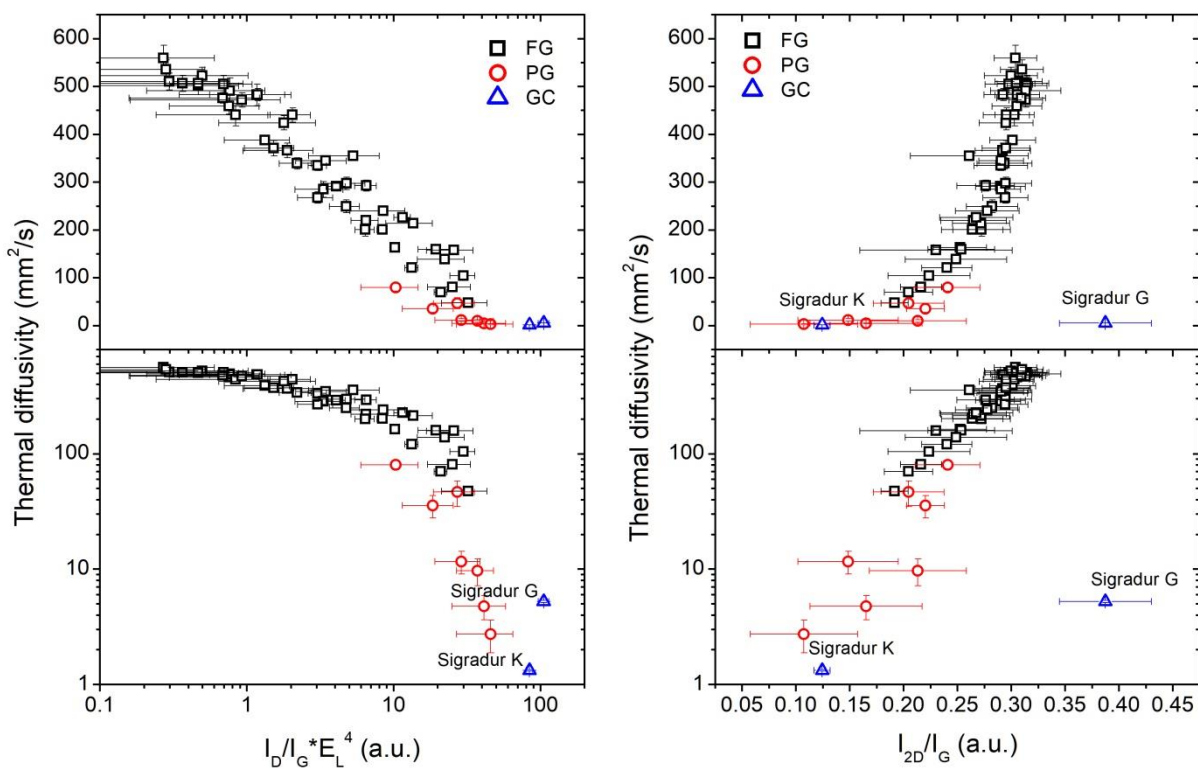


Figure 9.1 Thermal diffusivity as a function of the Raman parameters  $I_D/I_G E_L^4$  (left) and  $I_{2D}/I_G$  (right) for flexible graphite (FG), polycrystalline graphite (PG) and glassy carbon (GC) presented in linear (top) and logarithmic (bottom) scales.



---

## 10 Conclusions

---

In response to swift heavy ion irradiation, structural and morphological changes of well-oriented flexible graphite and fine grained isotropic polycrystalline graphite show quite different effects, which are explained by their different microscopic structure and texture.

Well-oriented flexible graphite, consisting of large graphite flakes, shows a high sensitivity to the elastic collisions in the nuclear energy loss regime. The damage process is dominated by the creation of point defects along the entire ion range for low Z (Ca), intermediate Z (Xe) and high Z (Au, U) ions, particularly in the last micrometers before the ions stop. The initial low defect concentration and absence of grain boundaries in FG prevents efficient recombination of point defects. The split structure of the D-peak in the Raman spectra of the irradiated flexible graphite together with SEM images suggest bending and folding of graphite flakes which is associated with the creation of non-six-member carbon rings. The Raman parameters show a strong correlation with the nuclear dose, calculated using separately nuclear and electronic fractions of the total energy loss. The electronic energy loss does not play a significant role up to 30 keV/nm. An exponential fit of the Raman parameters as a function of fluence yields damage cross-sections, which monotonously increase with nuclear energy loss.

In polycrystalline graphite, consisting of randomly oriented fine grains, both nuclear and electronic energy loss have a direct effect on structural changes. Similar to flexible graphite, the damage related to elastic collisions is for all ions more pronounced at the end of the ion range (last  $\sim 15 \mu\text{m}$ ), where the nuclear energy loss is maximal. In contrast to flexible graphite, polycrystalline graphite appears to be sensitive to the electronic energy loss. For high Z ions (Au and U) a significant defects density is observed already at a low fluence of  $1 \times 10^{12}$  ions/cm<sup>2</sup>. At a fluence of  $5 \times 10^{13}$  ions/cm<sup>2</sup>, polycrystalline graphite undergoes major modifications assigned to disordering, crystallite refinement and misalignment, and partial amorphization. The structure of highly damaged PG seems to become similar to glassy carbon. In the case of low Z ions (Ca), the first slight disordering (no evidences of amorphization) of the PG structure becomes visible at a fluence of  $5 \times 10^{13}$  ions/cm<sup>2</sup>. The difference effects of light and heavy ions are in agreement with a previously reported electronic energy threshold. Below this threshold, the deposited energy is not large enough to induce additional structural modification that are not only due to point defects. The threshold lies between Ca and Au ions, i.e. between 5 and 20 keV/nm.

---

Large flakes in flexible graphite severely suffer from point defects, but the energy deposited in the electronic subsystem seems to dissipate efficiently due to a very high conductivity in the basal planes and the semimetal nature of graphite. In spite of the folded edges of graphite flakes, their initial well-oriented structure and the large size prevents significant misalignment and interconnections of the bended crystallites in a way typical to glassy carbon, observed during irradiation of fine-grained isotropic polycrystalline graphite. The latter is sensitive to elastic collisions too, however, the electronic energy loss plays an additional role supposedly because of the small crystallite size limiting dissipation of the deposited energy.

Beam induced structural changes in flexible and polycrystalline graphite are directly reflected in their thermophysical properties. All trends and effects observed by Raman spectroscopy analysis are in good agreement with thermal diffusivity measurements. Flexible graphite samples show a significant degradation of the heat transport for the irradiation with low Z (Ca), intermediate Z (Xe) and high Z (Au, U) ions. The degradation clearly follows the trend of the nuclear energy loss. At high fluences, this results in a pronounced drop of the in-plane thermal diffusivity by one order of magnitude from  $\sim 550 \text{ mm}^2/\text{s}$  down to  $\sim 50 \text{ mm}^2/\text{s}$  for flexible graphite and from  $80 \text{ mm}^2/\text{s}$  to  $\sim 5\text{-}10 \text{ mm}^2/\text{s}$  for polycrystalline graphite. The irradiation of polycrystalline graphite with light Ca ions at the same fluence has only a weak effect on the thermal diffusivity, causing just  $\sim 10\%$  degradation.

The observed degradation of the thermal conductivity and diffusivity is explained by a decrease of the phonon mean free path and an enhanced phonon scattering on beam-induced point defects and grain boundaries. The strong correlation between the thermal diffusivity and the Raman results, provides an interesting possibility to estimate the thermal diffusivity in cases when standard thermophysical measurements are not possible because of sample size and/or geometry limitations.

---

## 11 Perspectives and open questions

---

A drastic degradation of the thermal diffusivity caused by ion irradiation can affect the heat dissipation in beam-intercepting devices. The dissipation efficiency of the deposited energy will drop leading to an increase of the operating temperature of the device. When designing beam-exposed graphite components, it is mandatory to take into account that the thermophysical properties will decay during operation. Based on the data provided in this thesis, uncontrolled overheating and failure on a long-term perspective can be avoided.

The results obtained extend knowledge on damage creation along the ion range in well-oriented graphite and isotropic polycrystalline graphite. The new data sheds light on the

---

different contributions of the nuclear and electronic energy loss but also raise additional questions.

Under the given experimental conditions, we could not clarify if high-fluence irradiations of polycrystalline graphite with swift heavy ions will eventually lead to complete amorphization as in the nuclear energy loss regime or if it retains a glassy-carbon-like structure. To clarify this final structural stage, fluences of the order of  $10^{15}$  -  $10^{16}$  ions/cm<sup>2</sup> and electronic energy loss values above 20 keV/nm are needed.

Although Raman spectroscopy is widely used for structural characterization of carbon-based materials, this method does not allow to unambiguously distinguish between similar carbon structures. A detailed HRTEM study of swift heavy ion irradiated graphite is required for direct identification of specific beam-induced damage structures.

The obtained experimental results should be compared with a detailed computer simulation (e.g. molecular dynamics) of the structural modification and corresponding changes in thermophysical properties induced by swift heavy ions in different types of graphite. Modeling of fine-grained isotropic graphite might be of special interest due to the observed different response in a high electronic energy loss regime.

In this work, the irradiation and material characterization were performed at room temperature. It is known, that defects in graphite can be annealed at high temperature with changes observed at around 200°C, 500°C and 1200°C. A systematic analysis of the graphite structure (Raman spectroscopy, HRTEM) and thermophysical properties (differential scanning calorimetry, LFA) at these high temperatures should be investigated for understanding annealing and recombination of different types of defects in well-oriented and isotropic polycrystalline graphite.

---

## References

- [1] H. Geissel, M. Winkler, H. Weick, K. Behr, G. Münzenberg, H. Simon, K. Sümmerer, B. Achenbach, D. Acker, D. Ackermann, T. Aumann, J. Äystö, R. Baer, M. Berz, D. Boutin, C. Brandau, A. Brünle, P. Dendooven, G. Fehrenbacher, E. Floch, M. Gleim, W. Hüller, H. Iwase, A. Kalimov, C. Karagiannis, M. Kauschke, A. Kelic, B. Kindler, G. Klappich, E. Kozlova, A. Krämer, A. Kratz, T. Kubo, N. Kurz, K. Kusaka, H. Leibrock, J. Lettry, S. Litvinov, Y. Litvinov, B. Lommel, S. Manikonda, A. Marbs, G. Moritz, C. Mühle, C. Nociforo, J.A. Nolen, H. Penttilä, W. Plass, Z. Podolyak, A. Prochazka, I. Pschorn, T. Radon, H. Ramakers, H. Reich-Sprenger, J. Saren, G. Savard, C. Scheidenberger, P. Schnizer, M. Schwickert, B. Sherrill, B. Sitar, A. Stafinak, R. Stieglitz, M. Svedentsov, N. Tahir, A. Tauschwitz, O. Tarasov, M. Tomut, P. Vobly, H. Welker, R. Wilfinger, C. Will, J. Winfield, Y. Xiang, M. Yavor, A. Yoshida, A. Zeller, Technical Design Report on the Super-FRS, Darmstadt, 2009.
- [2] S. Péraire, P.R. Sala, Beam dumps and beam stoppers for LHC and CNGS transfer lines, Geneva, 2001. <https://cds.cern.ch/record/487075/files/lhc-project-report-465.pdf> (accessed August 15, 2018).
- [3] M. Maslov, M. Schmitz, V. Sychev, Layout Considerations on the 25GeV / 300kW Beam Dump of the XFEL Project, 2006. [http://flash.desy.de/reports\\_publications/tesla\\_fel\\_reports/tesla\\_fel\\_2006/e1129/info\\_boxContent1791/fel2006-05.pdf](http://flash.desy.de/reports_publications/tesla_fel_reports/tesla_fel_2006/e1129/info_boxContent1791/fel2006-05.pdf) (accessed August 15, 2018).
- [4] P. Sigmund, Particle Penetration and Radiation Effects, Springer Berlin Heidelberg, 2006. <https://doi.org/10.1007/3-540-31718-X>.
- [5] D. Kiselev, R. Bergmann, D. Schumann, V. Talanov, M. Wohlmuther, Proton induced activity in graphite - Comparison between measurement and simulation, J. Phys. Conf. Ser. 1046 (2018). <https://doi.org/10.1088/1742-6596/1046/1/012003>.
- [6] C. Hubert, Characterization of radiation damage induced by swift heavy ions in graphite, TU Darmstadt, 2016. <http://tuprints.ulb.tu-darmstadt.de/id/eprint/5466>.
- [7] C. Hubert, K.O. Voss, M. Bender, K. Kupka, A. Romanenko, D. Severin, C. Trautmann, M. Tomut, Swift heavy ion-induced radiation damage in isotropic graphite studied by micro-indentation and in-situ electrical resistivity, Nucl. Instruments Methods Phys. Res. Sect. B Beam Interact. with Mater. Atoms. 365 (2015) 509–514. <https://doi.org/10.1016/j.nimb.2015.08.056>.
- [8] Z. Peng-Fei, J. Liu, Z. Jian, Y. Hui-Jun, D. Jing-Lai, H. Ming-Dong, S. You-Mei, E.R. Charles, Raman spectrum study of graphite irradiated by swift heavy ions \*, Chin. Phys. B. 23 (2014). <https://doi.org/10.1088/1674-1056/23/12/126105>.
- [9] F. Pellemoine, M. Avilov, M. Bender, R.C. Ewing, S. Fernandes, M. Lang, W.X. Li, W. Mittig, M. Schein, D. Severin, M. Tomut, C. Trautmann, F.X. Zhang, Study on structural recovery of graphite irradiated with swift heavy ions at high temperature, Nucl. In-

- 
- struments Methods Phys. Res. Sect. B Beam Interact. with Mater. Atoms. 365 (2015) 522–524. <https://doi.org/10.1016/j.nimb.2015.09.007>.
- [10] S. Fernandes, F. Pellemoine, M. Tomut, M. Avilov, M. Bender, M. Boulesteix, M. Krause, W. Mittig, M. Schein, D. Severin, C. Trautmann, In-situ electric resistance measurements and annealing effects of graphite exposed to swift heavy ions, *Nucl. Instruments Methods Phys. Res. Sect. B Beam Interact. with Mater. Atoms.* 314 (2013) 125–129. <https://doi.org/10.1016/j.nimb.2013.04.060>.
- [11] Facility for Antiproton and Ion Research, FAIR. (2018). [https://www.gsi.de/fileadmin/oeffentlichkeitsarbeit/fair/FAIR-beschriftet\\_MS\\_V\\_EN\\_Feb18.jpg](https://www.gsi.de/fileadmin/oeffentlichkeitsarbeit/fair/FAIR-beschriftet_MS_V_EN_Feb18.jpg) (accessed April 16, 2020).
- [12] G. Compagnini, O. Puglisi, G. Foti, Raman spectra of virgin and damaged graphite edge planes, *Carbon N. Y.* 35 (1997) 1793–1797. [https://doi.org/10.1016/S0008-6223\(97\)00141-3](https://doi.org/10.1016/S0008-6223(97)00141-3).
- [13] J. Liu, R. Neumann, C. Trautmann, C. Müller, Tracks of swift heavy ions in graphite studied by scanning tunneling microscopy, *Phys. Rev. B.* 64 (2001) 184115. [https://doi.org/Artn 184115\nDoi 10.1103/Physrevb.64.184115](https://doi.org/Artn%20184115%20nDoi%2010.1103/Physrevb.64.184115).
- [14] J. Zeng, J. Liu, H.J. Yao, P.F. Zhai, S.X. Zhang, H. Guo, P.P. Hu, J.L. Duan, D. Mo, M.D. Hou, Y.M. Sun, Comparative study of irradiation effects in graphite and graphene induced by swift heavy ions and highly charged ions, *Carbon N. Y.* 100 (2016) 16–26. <https://doi.org/10.1016/j.carbon.2015.12.101>.
- [15] P. Zhai, J. Liu, J. Zeng, J. Duan, L. Xu, H. Yao, H. Guo, S. Zhang, M. Hou, Y. Sun, Evidence for re-crystallization process in the irradiated graphite with heavy ions obtained by Raman spectroscopy, *Carbon N. Y.* 101 (2016) 22–27. <https://doi.org/10.1016/j.carbon.2016.01.076>.
- [16] J. Zeng, H.J. Yao, S.X. Zhang, P.F. Zhai, J.L. Duan, Y.M. Sun, G.P. Li, J. Liu, Swift heavy ions induced irradiation effects in monolayer graphene and highly oriented pyrolytic graphite, *Nucl. Instruments Methods Phys. Res. Sect. B Beam Interact. with Mater. Atoms.* 330 (2014) 18–23. <https://doi.org/10.1016/j.nimb.2014.03.019>.
- [17] J.H.W. Simmons, *Radiation Damage in Graphite*, Elsevier, 1965. <https://doi.org/10.1016/C2013-0-05555-7>.
- [18] T. Maruyama, M. Harayama, Neutron irradiation effect on the thermal conductivity and dimensional change of graphite materials, *J. Nucl. Mater.* 195 (1992) 44–50. [https://doi.org/10.1016/0022-3115\(92\)90362-O](https://doi.org/10.1016/0022-3115(92)90362-O).
- [19] T. Tanabe, T. Maruyama, M. Iseki, K. Niwase, H. Atsumi, Radiation damage of graphite: degradation of material parameters and defect structures, *Fusion Eng. Des.* 29 (1995) 428–434. [https://doi.org/10.1016/0920-3796\(95\)80049-4](https://doi.org/10.1016/0920-3796(95)80049-4).
- [20] L.L. Snead, T.D. Burchell, Thermal conductivity degradation of graphites due to neutron irradiation at low temperature, *J. Nucl. Mater.* 224 (1995) 222–229.

---

[https://doi.org/10.1016/0022-3115\(95\)00071-2](https://doi.org/10.1016/0022-3115(95)00071-2).

- [21] S. Ishiyama, T.D. Burchell, J.P. Strizak, M. Eto, The effect of high fluence neutron irradiation on the properties of a fine-grained isotropic nuclear graphite, *J. Nucl. Mater.* 230 (1996) 1–7. [https://doi.org/10.1016/0022-3115\(96\)00005-0](https://doi.org/10.1016/0022-3115(96)00005-0).
- [22] R. Krishna, A.N. Jones, L. McDermott, B.J. Marsden, Neutron irradiation damage of nuclear graphite studied by high-resolution transmission electron microscopy and Raman spectroscopy, *J. Nucl. Mater.* 467 (2015) 557–565. <https://doi.org/10.1016/j.jnucmat.2015.10.027>.
- [23] A.A. Campbell, Y. Katoh, M.A. Snead, K. Takizawa, Property changes of G347A graphite due to neutron irradiation, *Carbon N. Y.* 109 (2016) 860–873. <https://doi.org/10.1016/j.carbon.2016.08.042>.
- [24] C. Trautmann, Micro- and Nanoengineering with Ion Tracks, in: R. Hellborg, H.J. Whitlow, Y. Zhang (Eds.), *Ion Beams Nanosci. Technol.*, Springer Berlin Heidelberg, Berlin, Heidelberg, 2009: pp. 369–387. <https://doi.org/10.1007/978-3-642-00623-4>.
- [25] G.S. Was, *Fundamentals of Radiation Materials Science*, Springer New York, New York, NY, 2017. <https://doi.org/10.1007/978-1-4939-3438-6>.
- [26] I. Suarez-Martinez, N. a. Marks, Effect of microstructure on the thermal conductivity of disordered carbon, *Appl. Phys. Lett.* 99 (2011) 1–4. <https://doi.org/10.1063/1.3607872>.
- [27] L.D.S. Oliveira, P.A. Greaney, Thermal resistance from irradiation defects in graphite, *Comput. Mater. Sci.* 103 (2015) 68–76. <https://doi.org/10.1016/j.commatsci.2015.03.001>.
- [28] R.A. Rymzhanov, S.A. Gorbunov, N. Medvedev, A.E. Volkov, Damage along swift heavy ion trajectory, *Nucl. Instruments Methods Phys. Res. Sect. B Beam Interact. with Mater. Atoms.* 440 (2019) 25–35. <https://doi.org/10.1016/j.nimb.2018.11.034>.
- [29] K. Kupka, A.A. Leino, W. Ren, H. Vázquez, E.H. Åhlgren, K. Nordlund, M. Tomut, C. Trautmann, P. Kluth, M. Toulemonde, F. Djurabekova, Graphitization of amorphous carbon by swift heavy ion impacts: Molecular dynamics simulation, *Diam. Relat. Mater.* 83 (2018) 134–140. <https://doi.org/10.1016/j.diamond.2018.01.015>.
- [30] J. Habainy, Y. Lee, K.B. Surreddi, A. Prosvetov, P. Simon, S. Iyengar, Y. Dai, M. Tomut, Study of heavy ion beam induced damage in tungsten for high power target applications, *Nucl. Instruments Methods Phys. Res. Sect. B Beam Interact. with Mater. Atoms.* 439 (2019) 7–16. <https://doi.org/10.1016/j.nimb.2018.11.017>.
- [31] B.K. Bein, J. Gibkes, J.H. Gu, R. Hüttner, J. Pelzl, D.L. Balageas, A.A. Déom, Thermal wave characterization of plasma-facing materials by IR radiometry, *J. Nucl. Mater.* 191–194 (1992) 315–319. [https://doi.org/10.1016/S0022-3115\(09\)80057-3](https://doi.org/10.1016/S0022-3115(09)80057-3).
- [32] J. Gibkes, B.K. Bein, D. Krüger, J. Pelzl, Thermophysical characterization of fine-grain graphites based on thermal waves, *Carbon N. Y.* 31 (1993) 801–807.



---

[https://doi.org/10.1016/0008-6223\(93\)90018-6](https://doi.org/10.1016/0008-6223(93)90018-6).

- [33] C. Jensen, M. Chirtoc, N. Horny, J.S. Antoniow, H. Pron, H. Ban, Thermal conductivity profile determination in proton-irradiated ZrC by spatial and frequency scanning thermal wave methods, *J. Appl. Phys.* 114 (2013). <https://doi.org/10.1063/1.4821432>.
- [34] A. Prosvetov, G. Hamaoui, N. Horny, M. Chirtoc, F. Yang, C. Trautmann, M. Tomut, Degradation of thermal transport properties in fine-grained isotropic graphite exposed to swift heavy ion beams, *Acta Mater.* 184 (2020) 187–198. <https://doi.org/10.1016/j.actamat.2019.11.037>.
- [35] K. Momma, F. Izumi, VESTA 3 for three-dimensional visualization of crystal, volumetric and morphology data, *J. Appl. Crystallogr.* 44 (2011) 1272–1276. <https://doi.org/10.1107/S0021889811038970>.
- [36] B. Partoens, F.M. Peeters, From graphene to graphite: Electronic structure around the K point, *Phys. Rev. B - Condens. Matter Mater. Phys.* 74 (2006) 1–11. <https://doi.org/10.1103/PhysRevB.74.075404>.
- [37] O. Beyssac, M. Lazzeri, Application of raman spectroscopy to the study of graphitic carbons in the earth sciences, *Eur. Mineral. Union Notes Mineral.* 12 (2012) 415–454. <https://doi.org/10.1180/EMU-notes.12.12>.
- [38] N. Mounet, N. Marzari, First-principles determination of the structural, vibrational and thermodynamic properties of diamond, graphite, and derivatives, *Phys. Rev. B - Condens. Matter Mater. Phys.* 71 (2005) 1–14. <https://doi.org/10.1103/PhysRevB.71.205214>.
- [39] P.J.F. Harris, Fullerene-related structure of commercial glassy carbons, *Philos. Mag.* 84 (2004) 3159–3167. <https://doi.org/10.1080/14786430410001720363>.
- [40] K. Jurkiewicz, S. Duber, H.E. Fischer, A. Burian, Modelling of glass-like carbon structure and its experimental verification by neutron and X-ray diffraction, *J. Appl. Crystallogr.* 50 (2017) 36–48. <https://doi.org/10.1107/S1600576716017660>.
- [41] K. Jurkiewicz, M. Pawlyta, D. Zygadło, D. Chrobak, S. Duber, R. Wrzalik, A. Ratuszna, A. Burian, Evolution of glassy carbon under heat treatment: Correlation structure–mechanical properties, *J. Mater. Sci.* 53 (2018) 3509–3523. <https://doi.org/10.1007/s10853-017-1753-7>.
- [42] S. Sharma, C.N. Shyam Kumar, J.G. Korvink, C. Kübel, Evolution of Glassy Carbon Microstructure: In Situ Transmission Electron Microscopy of the Pyrolysis Process, *Sci. Rep.* 8 (2018) 1–12. <https://doi.org/10.1038/s41598-018-34644-9>.
- [43] B. Gervais, S. Bouffard, Simulation of the primary stage of the interaction of swift heavy ions with condensed matter, *Nucl. Inst. Methods Phys. Res. B.* 88 (1994) 355–364. [https://doi.org/10.1016/0168-583X\(94\)95384-8](https://doi.org/10.1016/0168-583X(94)95384-8).
- [44] J.F. Ziegler, Stopping of energetic light ions in elemental matter, *J. Appl. Phys.* 85 (1999) 1249–1272. <https://doi.org/10.1063/1.369844>.

- 
- [45] J.F. Ziegler, M.D. Ziegler, J.P. Biersack, SRIM - The stopping and range of ions in matter (2010), *Nucl. Instruments Methods Phys. Res. Sect. B Beam Interact. with Mater. Atoms.* 268 (2010) 1818–1823. <https://doi.org/10.1016/j.nimb.2010.02.091>.
- [46] A. Meftah, F. Brisard, J.M. Costantini, M. Hage-Ali, J.P. Stoquert, F. Studer, M. Toulemonde, Swift heavy ions in magnetic insulators: A damage-cross-section velocity effect, *Phys. Rev. B.* 48 (1993) 920–925. <https://doi.org/10.1103/PhysRevB.48.920>.
- [47] E.C.H. Silk, R.S. Barnes, Examination of fission fragment tracks with an electron microscope, *Philos. Mag.* 4 (1959) 970–972. <https://doi.org/10.1080/14786435908238273>.
- [48] M. Lang, F. Djurabekova, N. Medvedev, M. Toulemonde, C. Trautmann, Fundamental Phenomena and Applications of Swift Heavy Ion Irradiations, (2020) 1–73. <http://arxiv.org/abs/2001.03711>.
- [49] F.F. Komarov, Nano- and microstructuring of solids by swift heavy ions, *Uspekhi Fiz. Nauk.* 187 (2017) 465–504. <https://doi.org/10.3367/ufnr.2016.10.038012>.
- [50] N. Itoh, D.M. Duffy, S. Khakshouri, A.M. Stoneham, Making tracks: electronic excitation roles in forming swift heavy ion tracks., *J. Phys. Condens. Matter.* 21 (2009) 474205. <https://doi.org/10.1088/0953-8984/21/47/474205>.
- [51] L.V.T. M.I. Kaganov, I.M. Lifshitz, Relaxation between Electrons and the Crystalline Lattice, *Jetp.* 4 (1957) 173–178.
- [52] M. Toulemonde, W. Assmann, C. Dufour, A. Meftah, F. Studer, C. Trautmann, Experimental Phenomena and Thermal Spike Model Description of Ion Tracks in Amorphisable Inorganic Insulators, in: P. Sigmund (Ed.), *Ion Beam Sci. Solved Unsolved Probl. Mat. Meddelelser, Det Kongelige Danske Videnskabernes Selskab, Copenhagen, 2006*: pp. 263–292.
- [53] M. Toulemonde, W. Assmann, C. Dufour, a. Meftah, C. Trautmann, Nanometric transformation of the matter by short and intense electronic excitation: Experimental data versus inelastic thermal spike model, *Nucl. Instruments Methods Phys. Res. Sect. B Beam Interact. with Mater. Atoms.* 277 (2012) 28–39. <https://doi.org/10.1016/j.nimb.2011.12.045>.
- [54] M.P.R. Waligórski, R.N. Hamm, R. Katz, The radial distribution of dose around the path of a heavy ion in liquid water, *Int. J. Radiat. Appl. Instrumentation. Part. 11* (1986) 309–319. [https://doi.org/10.1016/1359-0189\(86\)90057-9](https://doi.org/10.1016/1359-0189(86)90057-9).
- [55] S. Klaumünzer, Thermal-Spike Models for Ion Track Physics: A Critical Examination, in: P. Sigmund (Ed.), *Ion Beam Sci. Solved Unsolved Probl. Mat. Meddelelser, Det Kongelige Danske Videnskabernes Selskab, Copenhagen, 2006*: pp. 293–328.
- [56] G. Szenes, Comparison of two thermal spike models for ion–solid interaction, *Nucl. Instruments Methods Phys. Res. Sect. B Beam Interact. with Mater. Atoms.* 269 (2011) 174–179. <https://doi.org/10.1016/j.nimb.2010.11.009>.

- 
- [57] N.A. Medvedev, R.A. Rymzhanov, A.E. Volkov, Corrigendum: Time-resolved electron kinetics in swift heavy ion irradiated solids (2015 J. Phys. D: Appl. Phys. 48 355303), J. Phys. D. Appl. Phys. 49 (2016). <https://doi.org/10.1088/0022-3727/49/36/369501>.
- [58] T.M. Tritt, Thermal Conductivity. Theory, Properties, and Applications, Kluwer Academic / Plenum Publishers, New York, 2004. <https://doi.org/10.1007/978-1-4899-3751-3>.
- [59] J.M. Ziman, Electrons and Phonons, Oxford University Press, 2001. <https://doi.org/10.1093/acprof:oso/9780198507796.001.0001>.
- [60] J. Issi, J. Heremans, M.S. Dresselhaus, Electronic and lattice contributions to the thermal conductivity of graphite intercalation compounds, Phys. Rev. B. 27 (1983).
- [61] P.G. Klemens, D.F. Pedraza, Thermal conductivity of graphite in the basal plane, Carbon N. Y. 32 (1994) 735–741. [https://doi.org/10.1016/0008-6223\(94\)90096-5](https://doi.org/10.1016/0008-6223(94)90096-5).
- [62] D.F. Pedraza, P.G. Klemens, Effective conductivity of polycrystalline graphite, Carbon N. Y. 31 (1993) 951–956. [https://doi.org/10.1016/0008-6223\(93\)90197-I](https://doi.org/10.1016/0008-6223(93)90197-I).
- [63] A.A. Balandin, Thermal properties of graphene and nanostructured carbon materials., Nat. Mater. 10 (2011) 569. <https://doi.org/10.1038/nmat3064>.
- [64] SGL Group, SIGRAFINE R6650 datasheet, (2015). [https://www.sglgroup.com/cms/\\_common/downloads/products/product-groups/gs/tds/iso/SIGRAFINE\\_TDS-R6650.02.pdf](https://www.sglgroup.com/cms/_common/downloads/products/product-groups/gs/tds/iso/SIGRAFINE_TDS-R6650.02.pdf) (accessed July 17, 2018).
- [65] HTW Hochtemperatur-Werkstoffe GmbH, HTW Germany. SIGRADUR datasheet, (2006). <http://htw-germany.com/technology.php5?lang=en&nav0=2&nav1=16> (accessed August 9, 2018).
- [66] C. Hubert, Characterization of radiation damage induced by swift heavy ions in graphite, Technische Universität Darmstadt, 2016. <http://tuprints.ulb.tu-darmstadt.de/id/eprint/5466> (accessed November 28, 2016).
- [67] “PGS” Graphite Sheets, Panasonic Ind. (2019). <https://industrial.panasonic.com/cdbs/www-data/pdf/AYA0000/AYA0000C27.pdf> (accessed May 8, 2020).
- [68] J.F. Ziegler, M.D. Ziegler, J.P. Biersack, SRIM – The stopping and range of ions in matter (2010), Nucl. Instruments Methods Phys. Res. Sect. B Beam Interact. with Mater. Atoms. 268 (2010) 1818–1823. <https://doi.org/10.1016/j.nimb.2010.02.091>.
- [69] L. Reimer, Scanning Electron Microscopy, Second, Springer, Berlin, Heidelberg, 1998. <https://doi.org/10.1007/978-3-540-38967-5>.
- [70] R.F. Egerton, Physical Principles of Electron Microscopy, Springer International Publishing, Cham, 2016. <https://doi.org/10.1007/978-3-319-39877-8>.
- [71] Scanning Electron Microscopy - Nanoscience Instruments, (n.d.). <https://www.nanoscience.com/techniques/scanning-electron-microscopy/> (accessed

---

March 26, 2020).

- [72] J. Bin Wu, M.L. Lin, X. Cong, H.N. Liu, P.H. Tan, Raman spectroscopy of graphene-based materials and its applications in related devices, *Chem. Soc. Rev.* 47 (2018) 1822–1873. <https://doi.org/10.1039/c6cs00915h>.
- [73] A. Merlen, J. Buijnsters, C. Pardanaud, A Guide to and Review of the Use of Multiwavelength Raman Spectroscopy for Characterizing Defective Aromatic Carbon Solids: from Graphene to Amorphous Carbons, 2017. <https://doi.org/10.1136/bmj.4.5937.162>.
- [74] A.C. Ferrari, D.M. Basko, Raman spectroscopy as a versatile tool for studying the properties of graphene, *Nat. Nanotechnol.* 8 (2013) 235–246. <https://doi.org/10.1038/nnano.2013.46>.
- [75] Y. Kaburagi, A. Yoshida, Y. Hishiyama, Raman Spectroscopy, in: *Mater. Sci. Eng. Carbon*, Tsinghua University Press Limited, 2016: pp. 125–152. <https://doi.org/10.1016/B978-0-12-805256-3.00007-6>.
- [76] K. Niwase, Raman Spectroscopy for Quantitative Analysis of Point Defects and Defect Clusters in Irradiated Graphite, *Int. J. Spectrosc.* 2012 (2012) 1–14. <https://doi.org/10.1155/2012/197609>.
- [77] L.M. Malard, M.A. Pimenta, G. Dresselhaus, M.S. Dresselhaus, Raman spectroscopy in graphene, *Phys. Rep.* 473 (2009) 51–87. <https://doi.org/10.1016/j.physrep.2009.02.003>.
- [78] P. Tan, S. Dimovski, Y. Gogotsi, Raman scattering of non-planar graphite: arched edges, polyhedral crystals, whiskers and cones, *Philos. Trans. R. Soc. A Math. Phys. Eng. Sci.* 362 (2004) 2289–2310. <https://doi.org/10.1098/rsta.2004.1442>.
- [79] S. Reich, C. Thomsen, Raman spectroscopy of graphite, *Philos. Trans. R. Soc. A Math. Phys. Eng. Sci.* 362 (2004) 2271–2288. <https://doi.org/https://doi.org/10.1098/rsta.2004.1454>.
- [80] A.C. Ferrari, Raman spectroscopy of graphene and graphite: Disorder, electron-phonon coupling, doping and nonadiabatic effects, *Solid State Commun.* 143 (2007) 47–57. <https://doi.org/10.1016/j.ssc.2007.03.052>.
- [81] P. Venezuela, M. Lazzeri, F. Mauri, Theory of double-resonant Raman spectra in graphene: Intensity and line shape of defect-induced and two-phonon bands, *Phys. Rev. B - Condens. Matter Mater. Phys.* 84 (2011) 1–25. <https://doi.org/10.1103/PhysRevB.84.035433>.
- [82] A. Sadezky, H. Muckenhuber, H. Grothe, R. Niessner, U. Pöschl, Raman microspectroscopy of soot and related carbonaceous materials: Spectral analysis and structural information, *Carbon N. Y.* 43 (2005) 1731–1742. <https://doi.org/10.1016/j.carbon.2005.02.018>.
- [83] M. Couzi, J.L. Bruneel, D. Talaga, L. Bokobza, A multi wavelength Raman scattering study of defective graphitic carbon materials: The first order Raman spectra revisited,

- 
- Carbon N. Y. 107 (2016) 388–394. <https://doi.org/10.1016/j.carbon.2016.06.017>.
- [84] M.M. Lucchese, F. Stavale, E.H.M. Ferreira, C. Vilani, M.V.O. Moutinho, R.B. Capaz, C. a. Achete, a. Jorio, Quantifying ion-induced defects and Raman relaxation length in graphene, Carbon N. Y. 48 (2010) 1592–1597. <https://doi.org/10.1016/j.carbon.2009.12.057>.
- [85] L.G. Cançado, A. Jorio, E.H. Martins Ferreira, F. Stavale, C.A. Achete, R.B. Capaz, M.V.O. Moutinho, A. Lombardo, T.S. Kulmala, A.C. Ferrari, Quantifying Defects in Graphene via Raman Spectroscopy at Different Excitation Energies, Nano Lett. 11 (2011) 3190–3196. <https://doi.org/10.1021/nl201432g>.
- [86] J. Ribeiro-Soares, M.E. Oliveros, C. Garin, M. V. David, L.G.P. Martins, C.A. Almeida, E.H. Martins-Ferreira, K. Takai, T. Enoki, R. Magalhães-Paniago, A. Malachias, A. Jorio, B.S. Archanjo, C.A. Achete, L.G. Cançado, Structural analysis of polycrystalline graphene systems by Raman spectroscopy, Carbon N. Y. 95 (2015) 646–652. <https://doi.org/10.1016/j.carbon.2015.08.020>.
- [87] F. Tuinstra, L. Koenig, Raman Spectrum of Graphite, J. Chem. Phys. 53 (1970) 1126–1130. <https://doi.org/10.1063/1.1674108>.
- [88] D.S. Knight, W.B. White, Characterization of crystalline quality of diamond films by Raman spectroscopy, Appl. Phys. Lett. 55 (1989) 2608–2610. <https://doi.org/10.1063/1.101951>.
- [89] N. Larouche, B.L. Stansfield, Classifying nanostructured carbons using graphitic indices derived from Raman spectra, Carbon N. Y. 48 (2010) 620–629. <https://doi.org/10.1016/j.carbon.2009.10.002>.
- [90] A. Ferrari, J. Robertson, Interpretation of Raman spectra of disordered and amorphous carbon, Phys. Rev. B. 61 (2000) 14095–14107. <https://doi.org/10.1103/PhysRevB.61.14095>.
- [91] L.G. Cançado, M. Gomes da Silva, E.H.M. Ferreira, F. Hof, K. Kampioti, K. Huang, A. Pénicau, C.A. Achete, R.B. Capaz, A. Jorio, Disentangling contributions of point and line defects in the Raman spectra of graphene-related materials, 2D Mater. 4 (2017) 025039. <https://doi.org/10.1088/2053-1583/aa5e77>.
- [92] A. Eckmann, A. Felten, A. Mishchenko, L. Britnell, R. Krupke, K.S. Novoselov, C. Casiraghi, Probing the nature of defects in graphene by Raman spectroscopy, Nano Lett. 12 (2012) 3925–3930. <https://doi.org/10.1021/nl300901a>.
- [93] A. Eckmann, A. Felten, I. Verzhbitskiy, R. Davey, C. Casiraghi, Raman study on defective graphene: Effect of the excitation energy, type, and amount of defects, Phys. Rev. B - Condens. Matter Mater. Phys. 88 (2013) 1–11. <https://doi.org/10.1103/PhysRevB.88.035426>.
- [94] LabSpec 6 Spectroscopy Suite Software - HORIBA, (2020). [https://www.horiba.com/en\\_en/products/detail/action/show/Product/labspec-6-](https://www.horiba.com/en_en/products/detail/action/show/Product/labspec-6-)

---

spectroscopy-suite-software-1843/ (accessed June 8, 2020).

- [95] M. Wojdyr, Fityk: a general-purpose peak fitting program, *J. Appl. Crystallogr.* 43 (2010) 1126–1128. <https://doi.org/10.1107/S0021889810030499>.
- [96] W.J. Parker, R.J. Jenkins, C.P. Butler, G.L. Abbott, Flash method of determining thermal diffusivity, heat capacity, and thermal conductivity, *J. Appl. Phys.* 32 (1961) 1679–1684. <https://doi.org/10.1063/1.1728417>.
- [97] L. Vozár, W. Hohenauer, Flash method of measuring the thermal diffusivity. A review, *High Temp. - High Press.* 35–36 (2003) 253–264. <https://doi.org/10.1068/htjr119>.
- [98] R.D. Cowan, Pulse method of measuring thermal diffusivity at high temperatures, *J. Appl. Phys.* 34 (1963) 926–927. <https://doi.org/10.1063/1.1729564>.
- [99] R.C. Heckman, Finite pulse-time and heat-loss effects in pulse thermal diffusivity measurements, *J. Appl. Phys.* 44 (1973) 1455–1460. <https://doi.org/10.1063/1.1662393>.
- [100] J.A. Cape, G.W. Lehman, Temperature and finite pulse-time effects in the flash method for measuring thermal diffusivity, *J. Appl. Phys.* 34 (1963) 1909–1913. <https://doi.org/10.1063/1.1729711>.
- [101] K.B. Larson, K. Koyama, Correction for finite-pulse-time effects in very thin samples using the flash method of measuring thermal diffusivity, *J. Appl. Phys.* 38 (1967) 465–474. <https://doi.org/10.1063/1.1709360>.
- [102] T. Azumi, Y. Takahashi, Novel finite pulse-width correction in flash thermal diffusivity measurement, *Rev. Sci. Instrum.* 52 (1981) 1411–1413. <https://doi.org/10.1063/1.1136793>.
- [103] J. Xue, X. Liu, Y. Lian, R. Taylor, The effects of a finite pulse time in the flash thermal diffusivity method, *Int. J. Thermophys.* 14 (1993) 123–133. <https://doi.org/10.1007/BF00522666>.
- [104] Y. Tao, L. Yang, Q. Zhong, Z. Xu, C. Luo, A modified evaluation method to reduce finite pulse time effects in flash diffusivity measurement, *Rev. Sci. Instrum.* 86 (2015). <https://doi.org/10.1063/1.4936590>.
- [105] M. Sheindlin, D. Halton, M. Musella, C. Ronchi, Advances in the use of laser-flash techniques for thermal diffusivity measurement, *Rev. Sci. Instrum.* 69 (1998) 1426–1436. <https://doi.org/10.1063/1.1148776>.
- [106] T. Baba, A. Ono, Improvement of the laser flash method to reduce uncertainty in thermal diffusivity measurements, *Meas. Sci. Technol.* 12 (2001) 2046–2057. <https://doi.org/10.1088/0957-0233/12/12/304>.
- [107] R.L. McMasters, J. V. Beck, R.B. Dinwiddie, H. Wang, Accounting for Penetration of Laser Heating in Flash Thermal Diffusivity Experiments, *J. Heat Transfer.* 121 (2008) 15. <https://doi.org/10.1115/1.2825929>.



- 
- [108] D.A. Watt, Theory of thermal diffusivity by pulse technique, *Br. J. Appl. Phys.* 17 (1966) 231–240. <https://doi.org/10.1088/0508-3443/17/2/311>.
- [109] A.B. Donaldson, R.E. Taylor, Thermal diffusivity measurement by a radial heat flow method, *J. Appl. Phys.* 46 (1975) 4584–4589. <https://doi.org/10.1063/1.321399>.
- [110] F.I. Chu, R.E. Taylor, A.B. Donaldson, Thermal diffusivity measurements at high temperatures by the radial flash method, *J. Appl. Phys.* 51 (1980) 336–341. <https://doi.org/10.1063/1.327377>.
- [111] K.B. Larson, K. Koyama, Measurement by the flash method of thermal diffusivity, heat capacity, and thermal conductivity in two-layer composite samples, *J. Appl. Phys.* 39 (1968) 4408–4416. <https://doi.org/10.1063/1.1656985>.
- [112] T.Y.R. Lee, A.B. Donaldson, R.E. Taylor, Thermal diffusivity of layered composites, in: V. V. Mirkovich (Ed.), *Therm. Conduct.* 15, Springer, Boston, MA, 1978: pp. 135–148. [https://doi.org/https://doi.org/10.1007/978-1-4615-9083-5\\_17](https://doi.org/https://doi.org/10.1007/978-1-4615-9083-5_17).
- [113] N. Araki, A. Makino, J. Mihara, Measurement and evaluation of the thermal diffusivity of two-layered materials, *Int. J. Thermophys.* 13 (1992) 331–349. <https://doi.org/10.1007/BF00504441>.
- [114] N. Araki, A. Makino, T. Ishiguro, J. Mihara, An analytical solution of temperature response in multilayered materials for transient methods, *Int. J. Thermophys.* 13 (1992) 515–538. <https://doi.org/10.1007/BF00503887>.
- [115] J. Hartmann, O. Nilsson, J. Fricke, Thermal diffusivity measurements on two-layered and three-layered systems with the laser-flash method, *High Temp. - High Press.* 25 (1993) 403–410.
- [116] W. Hohenauer, L. Vozár, An estimation of thermophysical properties of layered materials by the laser-flash method, *High Temp. - High Press.* 33 (2001) 17–25. <https://doi.org/10.1068/htwu184>.
- [117] B. Czél, K.A. Woodbury, J. Woolley, G. Gróf, Analysis of parameter estimation possibilities of the thermal contact resistance using the laser flash method with two-layer specimens, *Int. J. Thermophys.* 34 (2013) 1993–2008. <https://doi.org/10.1007/s10765-013-1496-x>.
- [118] Proteus® - NETZSCH Analyzing & Testing, (2020). <https://www.netzsch-thermal-analysis.com/en/products-solutions/software/proteus/> (accessed June 8, 2020).
- [119] LFA 427 - NETZSCH Analyzing and Testing, (2019). <https://www.netzsch-thermal-analysis.com/en/products-solutions/thermal-diffusivity-conductivity/lfa-427/> (accessed September 8, 2019).
- [120] P.-E. Nordal, S.O. Kanstad, Photothermal Radiometry, *Phys. Scr.* 20 (1979) 659–662. <https://doi.org/10.1088/0031-8949/20/5-6/020>.
- [121] P.M. Almond, D.P., Patel, *Photothermal Science and Techniques*, Springer Netherlands,

---

1996.

- [122] A. Salazar, Energy propagation of thermal waves, *Eur. J. Phys.* 27 (2006) 1349–1355. <https://doi.org/10.1088/0143-0807/27/6/009>.
- [123] M. Chirtoc, Investigation of layered systems by photothermal methods with periodic excitation, in: E.M. Moares (Ed.), *Therm. Wave Phys. Relat. Photothermal Tech. Basic Princ. Recent Dev.*, Transworld Research Network, 2009: pp. 29–63.
- [124] D. Maillet, S. André, J.C. Batsale, A. Degiovanni, C. Moyne, *Thermal Quadrupoles: Solving the Heat Equation Through Integral Transforms*, John Wiley and Sons Ltd, 2000.
- [125] R.M. Costescu, M.A. Wall, D.G. Cahill, Thermal conductance of epitaxial interfaces, *Phys. Rev. B.* 67 (2003) 054302. <https://doi.org/10.1103/PhysRevB.67.054302>.
- [126] B.C. Gundrum, D.G. Cahill, R.S. Averback, Thermal conductance of metal-metal interfaces, *Phys. Rev. B.* 72 (2005) 245426. <https://doi.org/10.1103/PhysRevB.72.245426>.
- [127] M.R. Ammar, N. Galy, J.N. Rouzaud, N. Toulhoat, C.E. Vaudey, P. Simon, N. Moncoffre, Characterizing various types of defects in nuclear graphite using Raman scattering: Heat treatment, ion irradiation and polishing, *Carbon N. Y.* 95 (2015) 364–373. <https://doi.org/10.1016/j.carbon.2015.07.095>.
- [128] D.G. McCulloch, S. Praver, A. Hoffman, Structural investigation of xenon-ion-beam-irradiated glassy carbon, *Phys. Rev. B.* 50 (1994) 5905–5917. <https://doi.org/10.1103/PhysRevB.50.5905>.
- [129] W.J. Weber, E. Zarkadoula, O.H. Pakarinen, R. Sachan, M.F. Chisholm, P. Liu, H. Xue, K. Jin, Y. Zhang, Synergy of elastic and inelastic energy loss on ion track formation in SrTiO<sub>3</sub>, *Sci. Rep.* 5 (2015). <https://doi.org/10.1038/srep07726>.
- [130] E. Zarkadoula, H. Xue, Y. Zhang, W.J. Weber, Synergy of inelastic and elastic energy loss: Temperature effects and electronic stopping power dependence, *Scr. Mater.* 110 (2016) 2–5. <https://doi.org/10.1016/j.scriptamat.2015.05.044>.
- [131] N. Sellami, M.L. Crespillo, Y. Zhang, W.J. Weber, Two-stage synergy of electronic energy loss with defects in LiTaO<sub>3</sub> under ion irradiation, *Mater. Res. Lett.* 6 (2018) 339–344. <https://doi.org/10.1080/21663831.2018.1455753>.
- [132] K. Jin, Y. Zhang, W.J. Weber, Synergistic effects of nuclear and electronic energy deposition on damage production in KTaO<sub>3</sub>, *Mater. Res. Lett.* 6 (2018) 531–536. <https://doi.org/10.1080/21663831.2018.1495131>.
- [133] L. Thomé, A. Debelle, F. Garrido, S. Mylonas, B. Décamps, C. Bachelet, G. Sattonnay, S. Moll, S. Pellegrino, S. Miro, P. Trocellier, Y. Serruys, G. Velisa, C. Grygiel, I. Monnet, M. Toulemonde, P. Simon, J. Jagielski, I. Jozwik-Biala, L. Nowicki, M. Behar, W.J. Weber, Y. Zhang, M. Backman, K. Nordlund, F. Djurabekova, Radiation effects in nuclear materials: Role of nuclear and electronic energy losses and their synergy, *Nucl. Instru-*



ments Methods Phys. Res. Sect. B Beam Interact. with Mater. Atoms. 307 (2013) 43–48. <https://doi.org/10.1016/j.nimb.2012.11.077>.

- [134] A.A. Balandin, Thermal properties of graphene and nanostructured carbon materials., *Nat. Mater.* 10 (2011) 569. <https://doi.org/10.1038/nmat3064>.
- [135] H. Zhang, X. Chen, Y.-D. Jho, A.J. Minnich, Temperature-Dependent Mean Free Path Spectra of Thermal Phonons Along the c -Axis of Graphite, *Nano Lett.* 16 (2016) 1643–1649. <https://doi.org/10.1021/acs.nanolett.5b04499>.
- [136] P.H. Chen, D.D.L. Chung, Thermal and electrical conduction in the compaction direction of exfoliated graphite and their relation to the structure, *Carbon N. Y.* 77 (2014) 538–550. <https://doi.org/10.1016/j.carbon.2014.05.059>.
- [137] J. Pelzl, B.K. Bein, Photothermal Characterization of Plasma Surface Modifications, *Pure Appl. Chem.* 64 (1992) 739–744. <https://doi.org/10.1351/pac199264050739>.
- [138] B.K. Bein, S. Krueger, J. Pelzl, Photoacoustic analysis of graphite limiters - changes in the thermal properties due to plasma limiter interaction, *J. Nucl. Mater.* 145–147 (1987) 458–462. [https://doi.org/10.1016/0022-3115\(87\)90381-3](https://doi.org/10.1016/0022-3115(87)90381-3).
- [139] Entegris, Inc, SPECIALTY CHEMICALS AND ENGINEERED MATERIALS Semiconductor Graphite Materials and post processes, 2019. [www.entegris.com](http://www.entegris.com) (accessed May 8, 2020).
- [140] SGL Group, SIGRAFINE ® R6550 datasheet, (2015). [https://www.sglgroup.com/cms/\\_common/downloads/products/product-groups/gs/tds/iso/SIGRAFINE\\_TDS-R6550.02.pdf](https://www.sglgroup.com/cms/_common/downloads/products/product-groups/gs/tds/iso/SIGRAFINE_TDS-R6550.02.pdf) (accessed November 23, 2018).
- [141] B. März, K. Jolley, R. Smith, H. Wu, Near-surface structure and residual stress in as-machined synthetic graphite, *Mater. Des.* 159 (2018) 103–116. <https://doi.org/10.1016/j.matdes.2018.08.041>.
- [142] I. Manika, J. Maniks, R. Zabels, J. Gabrusenoks, M. Krause, M. Tomut, K. Schwartz, Nanoindentation and raman spectroscopic study of graphite irradiated with swift 238U ions, *Fullerenes Nanotub. Carbon Nanostructures.* 20 (2012) 548–552. <https://doi.org/10.1080/1536383X.2012.656064>.
- [143] M. Tomut, B. Achenbach, K.H. Behr, W. Ensinger, H. Geissel, A. Hubner, A. Keli, B. Kindler, M. Krause, B. Lommel, I. Manika, R. Neumann, C. Scheidenberger, K. Schwartz, K. Sümmerer, C. Trautmann, H. Weick, M. Winkler, Experimental Investigations on Heavy-Ion Induced Radiation Damage of Graphite for the Super-FRS Target and Beam Catchers, in: K. Große (Ed.), *GSI Sci. Rep.* 2007, GSI, Darmstadt, 2008: p. 69. <http://repository.gsi.de/record/53524>.
- [144] C.H. Wu, J.P. Bonal, B. Kryger, The effect of high-dose neutron irradiation on the properties of graphite and silicon carbide, *J. Nucl. Mater.* 208 (1994) 1–7. [https://doi.org/10.1016/0022-3115\(94\)90191-0](https://doi.org/10.1016/0022-3115(94)90191-0).
- [145] R.E. Stoller, M.B. Toloczko, G.S. Was, A.G. Certain, S. Dwaraknath, F.A. Garner, On the

- 
- use of SRIM for computing radiation damage exposure, *Nucl. Instruments Methods Phys. Res. Sect. B Beam Interact. with Mater. Atoms.* 310 (2013) 75–80. <https://doi.org/10.1016/j.nimb.2013.05.008>.
- [146] H.J. Christie, D.L. Roach, I. Suarez-Martinez, N.A. Marks, M. Robinson, D.K. Ross, Simulating radiation damage cascades in graphite, *Carbon N. Y.* 81 (2014) 105–114. <https://doi.org/10.1016/j.carbon.2014.09.031>.
- [147] A.J. McKenna, T. Trevethan, C.D. Latham, P.J. Young, M.I. Heggie, Threshold displacement energy and damage function in graphite from molecular dynamics, *Carbon N. Y.* 99 (2016) 71–78. <https://doi.org/10.1016/j.carbon.2015.11.040>.
- [148] G. Fugallo, A. Cepellotti, L. Paulatto, M. Lazzeri, N. Marzari, F. Mauri, Thermal conductivity of graphene and graphite: Collective excitations and mean free paths, *Nano Lett.* 14 (2014) 6109–6114. <https://doi.org/10.1021/nl502059f>.
- [149] Z.G. Fthenakis, Z. Zhu, D. Tománek, Effect of structural defects on the thermal conductivity of graphene: From point to line defects to haeckelites, *Phys. Rev. B - Condens. Matter Mater. Phys.* 89 (2014) 1–6. <https://doi.org/10.1103/PhysRevB.89.125421>.
- [150] W.J. Weber, Models and mechanisms of irradiation-induced amorphization in ceramics, *Nucl. Instruments Methods Phys. Res. Sect. B Beam Interact. with Mater. Atoms.* 166 (2000) 98–106. [https://doi.org/10.1016/S0168-583X\(99\)00643-6](https://doi.org/10.1016/S0168-583X(99)00643-6).

---

## List of figures

Figure 1.1 Scheme of the current GSI (in blue) and future (in red) FAIR accelerator facility, adapted from [11]. The materials research facilities are highlighted with colorful rings.	11
Figure 2.1 The crystal lattice of hexagonal graphite with the unit cell (dashed lines) and characteristic sizes, created using VESTA software [35].	14
Figure 2.2 The Brillouin zone (left) and electronic band structure (right) of graphene (top) and graphite (bottom), adapted from [37].	15
Figure 2.3 Phonon dispersion of graphite adapted from [38]. Lines and points show ab initio calculations and experimental data, respectively.	16
Figure 2.4 TEM images of Sigradur K (A) and Sigradur G (B) glassy carbon produced at 1000°C and 2800°C, respectively. Models for the fullerene-related structure of low-temperature (C) and high-temperature (D) glassy carbon, proposed by Harris. The figures are reproduced from [39].	19
Figure 2.5 Nuclear (dashed lines) and electronic (solid lines) energy loss of different ions in graphite as a function of specific energy, calculated using SRIM-2013 software.	22
Figure 2.6 Spectral radiance according to Planck's law at different temperatures.	28
Figure 3.1 Photo of pristine samples. From left to right: polycrystalline graphite disc ( $\emptyset$ 10 mm, 500 $\mu\text{m}$ thick), polycrystalline graphite disk ( $\emptyset$ 20 mm, 50 $\mu\text{m}$ thick), flexible graphite disk ( $\emptyset$ 20 mm, 21 $\mu\text{m}$ thick).	29
Figure 3.2 Optical microscopy images of flexible graphite (A) and polycrystalline graphite (B).	30
Figure 3.3 Optical microscopy images of Sigradur K (A) and Sigradur G (B) glassy carbon samples.	30
Figure 4.1 Scheme of GSI linear accelerator UNILAC, adapted from [66].	31
Figure 4.2 Schematic structure of M3-beamline at UNILAC.	31
Figure 4.3 Example of a 2 cm $\times$ 2 cm beam spot checked on a luminescence screen (right) next to a sample holder (left).	32
Figure 5.1 Scheme of processes in the interaction volume of a sample exposed to the electron beam, adapted from [71].	34
Figure 5.2 Energy level representation of elastic (Rayleigh) and inelastic (Raman) scattering.	36

Figure 5.3 Raman spectra and fitted peaks of pristine (a) and ion irradiated flexible (b) and polycrystalline (c) graphite with main vibration modes. The inset graph shows a zoomed view on the D-band.....	38
Figure 5.4 Local activation model for point defects (a) and crystallite boundaries (b), adapted from [73]. The right graphs show zoomed in schemes of the 0D and 1D defects. The disordered and activated regions are marked green and yellow, respectively.....	40
Figure 5.5 The evolution of $A_D/A_G \propto E_L^4$ as a function of FWHM(G) of graphene materials with dominant presence of point defects (dashed line and solid symbols) and 1D line defects (solid line and open symbols), adapted from [91]. .....	41
Figure 5.6 Scheme of Raman spectroscopy measurements of a) flexible graphite samples, b) cross-section of polycrystalline graphite samples. Blue dots illustrate probed positions on the samples. ....	43
Figure 5.7 Temperature rise on the rear side of a sample induced by a laser flash. ....	44
Figure 5.8 a) Recorded LFA signal for PG samples of different thickness measured with a laser pulse of 0.3 ms; b) Apparent thermal diffusivity values as a function of thickness for Cu, Al, C and Ti samples. ....	45
Figure 5.9 Scheme of an in-plane laser flash measurement. ....	46
Figure 5.10 Scheme of laser flash setup LFA427 adapted from [119]. ....	47
Figure 5.11 Measured in-plane thermal diffusivity of pristine polycrystalline graphite as a function of the laser voltage for different pulse length. ....	47
Figure 5.12 Scheme of photothermal radiometry setup. ....	50
Figure 6.1 SEM images of flexible graphite before (a, c) and after (b, d) irradiation by 4.8 MeV/u Au ions at a fluence of $1 \times 10^{13}$ ions/cm <sup>2</sup> at low and high magnification. ...	51
Figure 6.2 Raman spectra of flexible graphite irradiated with 4.8 MeV/u Ca (a, b, c) and Au (d, e, f) ions at fluences from $1 \times 10^{11}$ to $1.34 \times 10^{14}$ ions/cm <sup>2</sup> . The measurements correspond to a penetration depth of 0, $21 \pm 1 \mu\text{m}$ and $42 \pm 2 \mu\text{m}$ of the ion beam.....	52
Figure 6.3 Raman D-band of ion irradiated flexible graphite consisting of D1 and D2 peaks..	53
Figure 6.4 Evolution of Raman parameters FWHM(G), $I_D/I_G$ , $A_D/A_G$ , $I_{2D}/I_G$ , $I_D/I_G$ , and $I_D/I_D'$ with increasing fluence for 4.8 MeV/u Ca, Xe and Au ion irradiated flexible graphite at different depths. Shaded areas denote average pristine values of the respective parameters.....	54



Figure 6.5 a-d) Electronic and nuclear energy loss of 4.8 MeV/u Ca, Xe, Au and U ions in flexible graphite, calculated using SRIM-2013. e-p) Raman parameters FWHM(G), $I_D/I_G$ , and $I_{2D}/I_G$ as a function of depth. The Raman spectra were recorded at the front and rear surfaces of three flexible graphite samples irradiated in stacks. ....	55
Figure 6.6 Raman parameters $I_D/I_G$ , FWHM(G) and $I_{2D}/I_G$ as a function of dose, calculated using nuclear (left) and electronic (right) energy loss of Ca, Xe, Au and U ions in flexible graphite. ....	56
Figure 6.7 Raman parameters $I_D/I_G$ and $A_D/A_G$ , normalized by the laser excitation energy $E_L$ , as a function of FWHM(G) for various ion irradiations. ....	57
Figure 6.8 SEM images of polycrystalline graphite sample irradiated with 4.8 MeV/u U ions at a fluence of $5 \times 10^{13}$ ions/cm <sup>2</sup> . a) and b) low magnification images of sample cross-section, the dashed line marks the SRIM calculated ion range (upper area: irradiated and lower area: pristine); c) high magnification image of non-irradiated section (beyond ion range); d) irradiated area of graphite sample within ion range. ....	58
Figure 6.9 (Left) Stacked Raman spectra recorded on polycrystalline graphite sample cross-sections along the ion range for 4.8 MeV/u (a) Ca, (b) Au and (c) U ion irradiation at a fluence of $5 \times 10^{13}$ ions/cm <sup>2</sup> ; (Right) Corresponding intensity maps. All spectra are normalized to the intensity of the G-band. ....	60
Figure 6.10 Raman spectra of pristine as well as 4.8 MeV/u Ca (a, b), Au (c, d) and U (e, f) ion irradiated polycrystalline graphite at different fluences, measured at the depth with dominant electronic ( $\sim 15 \mu\text{m}$ ) and nuclear ( $\sim 50 \mu\text{m}$ ) energy loss. ....	61
Figure 6.11 a, b, c – Electronic and nuclear energy loss of 4.8 MeV/u Ca, Au and U ions in polycrystalline graphite. The ratio of intensities $I_D/I_G$ (d, e, f), $I_{D3}/I_G$ (g, h, i), FWHM(G) (j, k, l) and $I_{2D}/I_G$ (p, q, r) averaged over five line profiles measured on fractured cross-section of samples irradiated with 4.8 MeV/u Ca, Au and U ions at fluences of $1 \times 10^{12}$ , $1 \times 10^{13}$ and $5 \times 10^{13}$ ions/cm <sup>2</sup> . ....	63
Figure 6.12 Evolution of the Raman parameters with increasing fluence of 4.8 MeV/u Ca, Au and U ion irradiated polycrystalline graphite. Full symbols are averaged values from 0 - $40 \mu\text{m}$ sample depth dominated by electronic stopping and open symbols are averaged values from 40 - $56 \mu\text{m}$ sample depth dominated by nuclear stopping. The average values of pristine polycrystalline graphite and two kinds of glassy carbon processed at different temperatures (discussed further in the text) are marked by shaded areas. ....	64

---

Figure 6.13 Dependence of $I_D/I_G$ , FWHM(G), $I_{D3}/I_G$ and $I_{2D}/I_G$ on the calculated nuclear (left) and electronic (right) fraction of dose, induced by Ca, Au and U ion irradiation of polycrystalline graphite.....	65
Figure 6.14 A – (a) Raman spectra of glassy carbon, processed at different temperatures from 600°C to 2500°C, adapted from [41]. Comparison of the spectra for the first order(b) and the second order (c) wavenumber regions of the different D bands. B – Raman spectra of the Sigradur K and Sigradur G glassy carbon grades. ....	67
Figure 6.15 G-band position of Ca, Au and U ion irradiated polycrystalline graphite measured along the ion range at fluence of $1 \times 10^{12}$ , $1 \times 10^{13}$ and $5 \times 10^{13}$ ions/cm <sup>2</sup> . The arrow indicates the interface between the irradiated and non-irradiated zone.....	68
Figure 6.16 $A_D/A_G$ normalized by the laser excitation energy as a function of FWHM(G) for ion irradiated flexible and polycrystalline graphite.....	69
Figure 7.1 LFA detector signals of flexible graphite from a sample stack irradiated with 4.8 MeV/u Ca (left) and Au (right) ions of various fluences: 0-21 $\mu\text{m}$ represents the front sample and 21-42 $\mu\text{m}$ represents the middle sample. For both samples the entire volume is irradiated. ....	73
Figure 7.2 Absolute (left) and relative (right) in-plane thermal diffusivity as a function of fluence of 4.8 MeV/u Ca, Xe, Au and U ion irradiated flexible graphite. ....	74
Figure 7.3 In-plane thermal diffusivity of flexible graphite as a function of dose, calculated using nuclear (left) and electronic (right) energy loss of Ca, Xe, Au and U ions.....	75
Figure 7.4 Relative transversal thermal diffusivity of flexible graphite irradiated with 4.8 MeV/u Ca, Xe and Au ions. ....	76
Figure 7.5 Example of LFA detector signal of in-plane measurements of 4.8 MeV/u Ca and Au ion irradiated polycrystalline graphite. Dashed lines are fits to the experimental data.	78
Figure 7.6 In-plane thermal diffusivity of the polycrystalline graphite irradiated with C, Ca and Au ions. (left) - absolute values; (right) - relative thermal diffusivity change with respect to the thermal diffusivity of pristine polycrystalline graphite. ....	78
Figure 7.7 Normalized amplitude and phase of the PTR signal for a pristine polycrystalline graphite sample. Open red and blue circle symbols correspond to the respective experimental data measured on the cut only and on the lapped surface of the same sample. Solid lines are fits to the experimental data by implementing an additional surface layer. The dashed lines illustrate that fits considering only a single homogeneous graphite layer cannot describe the measured data adequately above 20	

Hz. The vertical dotted line indicates the transition frequency at which the sample becomes thermally thick, i.e. $\mu = L$ . .....	80
Figure 7.8 Sensitivity of amplitude and phase to the fit parameters for pristine polycrystalline graphite sample with cut (a, b) and lapped (c, d) surfaces. ....	81
Figure 7.9 Scanning PTR measurements: phase response versus frequency for isotropic polycrystalline graphite grades with a nominal grain size of 1, 7, 10 and 20 $\mu\text{m}$ . The two curves for each grade represent the cut only and the lapped faces of the same sample. ....	82
Figure 7.10 Data for different polycrystalline graphite grades (cut and lapped surfaces) including information on density and grain size. (left) effusivity and $L \cdot a^{-1/2}$ ; (right) thermal diffusivity and thickness calculated from the PTR data. Effusivity and thermal diffusivity of bulk graphite are obtained from the LFA measurements. ....	83
Figure 7.11 Series of PTR data for isotropic polycrystalline graphite samples irradiated with C (5.9 MeV/u), Ca (4.8 MeV/u), Au (4.8 and 5.9 MeV/u) and U (4.8 MeV/u) ions of various fluences: (A) normalized amplitude and (B) phase of thermal signal as a function of frequency. Solid lines are model fits considering a 3-layer system. ....	85
Figure 7.12 Sensitivity of amplitude (A) and phase (B) to the fit parameters for polycrystalline graphite samples irradiated with 4.8 MeV/u Au ions of fluence a) $1 \times 10^{11}$ , b) $1 \times 10^{12}$ , c) $1 \times 10^{13}$ , d) $5 \times 10^{13}$ ions/cm <sup>2</sup> . ....	86
Figure 7.13 Thermal effusivity (left) and $L \cdot a^{-1/2}$ (right) values versus fluence as deduced from fits to experimental PRT data: surface layer (open symbols) and irradiated layer (full symbols) for polycrystalline graphite samples exposed to C, Ca, Au and U ion beams.	87
Figure 7.14 Thermal diffusivity (left) and thickness (right) of the irradiated surface layer calculated from fits of effusivity and $L \cdot a^{-1/2}$ . ....	88
Figure 7.15 Relative thermal effusivity with respect to the pristine value as a function of fluence for polycrystalline graphite irradiated with C, Ca, Au and U ions. ....	89
Figure 7.16 Absolute (left) and relative (right) degradation of thermal diffusivity of C, Ca, Au and U ion irradiated graphite as a function of fluence. The data were deduced from thermal effusivity measurements assuming that the pristine value of the volumetric heat capacity does not change. ....	90
Figure 8.1 $I_D/I_G$ , FWHM(G) and $I_{2D}/I_G$ (symbols) and corresponding fits (lines) as a function of fluence for flexible graphite irradiated with Ca, Xe, Au and U ions at different depth along the ion range. ....	95



Figure 8.2 Damage cross-section of Ca, Xe, Au and U ions in flexible graphite as a function of nuclear energy loss, calculated based on fits to the fluence evolution of Raman parameters FWHM(G),  $I_D/I_G$ , and  $I_{2D}/I_G$ . The black star shows a value reconstructed for HOPG irradiated with 4 MeV Kr ions from reference [14]. ..... 95

Figure 8.3 Relative thermal diffusivity as a function of ion fluence for flexible graphite irradiated with Ca and Au ions. Lines represent exponential fits (Eq. 8.1) by a single impact model. .... 96

Figure 8.4 Relative thermal diffusivity (left) and effusivity (right) as a function of applied fluence for polycrystalline graphite irradiated with Au and U ions. Lines represent exponential fits (Eq. 8.1) by a single impact model. .... 97

Figure 9.1 Thermal diffusivity as a function of the Raman parameters  $I_D/I_G E_L^4$  (left) and  $I_{2D}/I_G$  (right) for flexible graphite (FG), polycrystalline graphite (PG) and glassy carbon (GC) presented in linear (top) and logarithmic (bottom) scales. .... 99

---

## List of tables

Table 4.1 Irradiation parameters for flexible graphite (FG) and polycrystalline graphite (PG) disc samples. Ion range is calculated using SRIM-2013 code with an uncertainty of about 10% [68]. Flux and fluence uncertainties are assumed to be between 10 and 20%. .....	33
Table 5.1 List of deconvoluted peaks of graphite Raman spectra recorded with a laser of wavelength $\lambda=473$ nm. ....	37
Table 7.1 Thermal effusivity $e$ of pristine graphite (SIGRAFINE R6650) from laser flash analysis and PTR results for $e$ and $L \cdot a^{-1/2}$ of cut and lapped surface layers. ....	81
Table 7.2 Density and average grain size of different polycrystalline graphite grades as presented in the datasheets [139,140]; thermal diffusivity values were measured using laser flash analysis. ....	82
Table 8.1 Damage cross-sections $\sigma$ deduced from fits to the different Raman data $I_D/I_G$ , FWHM(G) and $I_{2D}/I_G$ of ion irradiated flexible graphite. ....	94
Table 8.2 Damage cross sections deduced from fits to LFA data of flexible graphite irradiated with Ca and Au ions. Amplitude A of Eq. 8.1 is in all cases $-0.87 \pm 0.01$ , and $Y_0$ is set to 1. ....	96
Table 8.4 Damage cross sections deduced from fits (Equation 8.1) to thermal diffusivity and effusivity data of polycrystalline graphite irradiated with Au and U ions. ....	97

---

## List of abbreviations

TUD	Technische Universität Darmstadt
GSI	Gesellschaft für Schwerionenforschung
FAIR	Facility for Antiproton and Ion Research
UNILAC	Universal Linear Accelerator
PIG	Penning Ionization Gauge
MEVVA	Metal Vapor Vacuum Arc Ion Source
RFQ	Radio Frequency Quadrupole
LFA	Laser Flash Analysis
PTR	Photothermal Radiometry
SEM	Scanning Electron Microscopy
SE	Secondary Electrons
TEM	Transmission Electron Microscopy
HRTEM	High Resolution Transmission Electron Microscopy
HOPG	Highly Oriented Pyrolytic Graphite
FG	Flexible Graphite
PG	Polycrystalline graphite
GC	Glassy carbon
SRIM	Stopping and Range of Ions in Matter
i-TS	Inelastic Thermal Spike
CDF	Complex Dielectric Function
DSF	Dynamic Structure Factor
FWHM	Full Width at Half Maximum



---

## Acknowledgments

I express my sincere gratitude to everyone who supported me through all the challenges on my way to the doctorate degree and contributed to this thesis.

First of all, I thank my PhD supervisor, Prof. Dr. Christina Trautmann, for inviting me to the Materials Research Department at GSI and giving me the opportunity to perform this thesis. I greatly appreciate her endless support and guidance in my research activity, as well as her always open door in case of any question.

I am very grateful to my supervisor and mentor, Dr. Marilena Tomut, for taking care of me, for her guidance and helpful recommendations during my PhD time. Thank you for stimulating my personal and professional growth.

I would like to thank Prof. Dr. Wolfgang Ensinger, Prof. Dr. Ralph Krupke and Prof. Dr. Gerhard Wilde for their kindness and readiness to be a member of my PhD examination board. Especially I thank Prof. Trautmann and Prof. Ensinger for being referee of this thesis.

I am thankful to my former supervisors from the Joint Institute for Nuclear Research, Vladimir Skuratov, D.Sc., and Alexander Volkov, PhD, who introduced me to the field of swift heavy ions and taught me to think about the right questions.

I would like to express my gratitude to Prof. Dr. Mihai Chirtoc, Dr. Nicolas Horny and Dr. Georges Hamaoui for accepting me in their group at the University of Reims Champagne-Ardenne, sharing their expertise in photothermal radiometry and our fruitful collaboration.

I would like to thank Dr. Florent Yang for his help with SEM measurements.

I am thankful to the HGS-HiRe graduate school for the financial support dedicated to attending conferences and a research stay abroad. I appreciate their great soft-skill courses as well as interesting lecture and power weeks.

I would like to thank all members of the Materials Research group for being great colleagues, for a very friendly working atmosphere, and open discussions on any topic, as well as for a crazy amount of shared cakes and sweets. My special gratitude goes to Dr. Anton Romanenko, Dr. Peter Katrik, Pascal Simon, Jacob Lee, Dr. Michael Wagner, Philipp Bolz, Nils Ulrich, Dr. Liana Movsesyan, Dr. Christian Hubert, Dr. Janina Krieg, Dr. Katharina Kupka, Dr. Anne Spende, Dr. Marco Cassinelli, Dr. Loïc Burr, Dr. Mercedes Carrillo Solano, Dr. Wouter Majjenburg for sharing both scientific and entertaining activities and having a great time together.

---

I am very thankful to my old friends Alexander Vidiborskiy, Timofei Slimovskii and Mihail Rijov for their priceless support and encouragement, although most of the time we were located very far from each other.

The deepest gratitude belongs to my beloved Sashi Limbu, my brother Artem, and my parents Tatiana and Vladimir, for their permanent support, inspiration, trust and understanding.

---

# Curriculum Vitae

## Alexey Prosvetov



### Personal details:

Date of birth: 5 December 1989

Place of birth: Chisinau (Republic of Moldova)

### Education:

03/2015 - 08/2020 **PhD in Materials Science**

Technical University of Darmstadt, Darmstadt (Germany)

Thesis: Ion beam induced modification of structure and heat transfer properties in graphite materials.

09/2012 - 06/2014 **M.Sc. in Applied Mathematics and Physics**, Diploma with Honors

Moscow Institute of Physics and Technology, Moscow (Russia)

Thesis: MD modelling of structural changes in heavy ion tracks in  $\text{Al}_2\text{O}_3$ .

09/2008 - 06/2012 **B.Sc. in Physics**, Diploma with Honors,

Dubna State University, Dubna (Russia)

Thesis: Spatial correlation between oxide nanoparticles and displacement cascades induced by swift heavy ions in ODS-alloys.

### Work Experience

03/2015 - 07/2020 **Doctoral researcher**

GSI Helmholtzzentrum für Schwerionenforschung, Darmstadt (Germany)

10/2010 - 02/2015 **Laboratory assistant, Engineer**

Joint Institute for Nuclear Research, Dubna (Russia).

### Grants and Awards

2018 Giersch Excellence Award

2017 Giersch Excellence Award

2017 HGS-HIRE Abroad Grant

2016 Award for best student presentation at EMRS 2016 Fall meeting

---

## Scientific contribution

### Publications

- **A. Prosvetov**, G. Hamaoui, N. Horny, M. Chirtoc, F. Yang, C. Trautmann, M. Tomut, Degradation of thermal transport properties in fine-grained isotropic graphite exposed to swift heavy ion beams, *Acta Mater.* 184 (2020) 187–198.  
<https://doi.org/10.1016/j.actamat.2019.11.037>.
- J. Habainy, Y. Lee, K.B. Surreddi, **A. Prosvetov**, P. Simon, S. Iyengar, Y. Dai, M. Tomut, Study of heavy ion beam induced damage in tungsten for high power target applications, *Nucl. Instruments Methods Phys. Res. Sect. B Beam Interact. with Mater. Atoms.* 439 (2019) 7–16. <https://doi.org/10.1016/j.nimb.2018.11.017>.
- C. Goy, M.A. C. Potenza, S. Dederà, M. Tomut, E. Guillermin, A. Kalinin, K.-O. Voss, A. Schottelius, N. Petridis, **A. Prosvetov**, G. Tejada, J.M. Fernández, C. Trautmann, F. Caupin, U. Glasmacher, R.E. Grisenti, Shrinking of Rapidly Evaporating Water Microdroplets Reveals their Extreme Supercooling, *Phys. Rev. Lett.* 120, 015501 (2018)  
<https://doi.org/10.1103/PhysRevLett.120.015501>
- **A. Prosvetov**, C. Trautmann, M. Tomut, Non-homogeneous ion beam induced modification of flexible graphite along the ion range, GSI-FAIR Scientific Report 2017, p. 203 (2018), DOI:10.15120/GR-2018-1
- **A. Prosvetov**, C. Trautmann, M. Tomut, Thermal diffusivity degradation of heavy ions irradiated isotropic graphite, GSI Scientific Report 2016, p. 254 (2017), DOI:10.15120/GR-2017-1

### Oral presentations

- Photothermal radiometry study of heavy ion beam induced modification of polycrystalline graphite thermal properties.  
A. Prosvetov, G. Hamaoui, N. Horny, M. Chirtoc, F. Yang, C. Trautmann, M. Tomut  
SHIM-ICACS, 2018, Caen (France)
- Photothermal radiometry study of heavy ion beam induced modification of polycrystalline graphite thermal properties.  
A. Prosvetov, G. Hamaoui, N. Horny, M. Chirtoc, F. Yang, C. Trautmann, M. Tomut  
MAT Science week, 2018, Darmstadt (Germany)
- In-plane and through-plane laser flash measurements of thermal diffusivity degradation induced by heavy ion irradiation in thin graphite samples.  
A. Prosvetov, C. Trautmann, M. Tomut  
AITA, 2017, Quebec City (Canada)
- Swift heavy ion induced degradation of thermal diffusivity of different graphite grades.  
A. Prosvetov, C. Trautmann, M. Tomut  
Ion beam workshop, 2017, Göttingen (Germany)

---

## Poster presentations

- Raman spectroscopy analysis of swift heavy ion beam induced damage along the ion range in flexible graphite.  
A. Prosvetov, F. Yang, P. Bolz, C. Trautmann, M. Tomut  
SHIM-ICACS, 2018, Caen (France)
- Swift heavy ion induced degradation of thermal diffusivity of different graphite grades.  
A. Prosvetov, C. Trautmann, M. Tomut  
European Materials Research Society, 2016 Fall meeting, Warsaw (Poland)
- Spatial correlation of oxide nanoparticles and displacement cascades induced by swift heavy ions in ODS-alloys.  
A. Prosvetov, V. Skuratov  
Joint ICTP-IAEA Workshop on Physics of Radiation Effect and its Simulation for Non-Metallic Condensed Matter, 2012, Trieste (Italy)